Jyri Kivimäki

Issues in Design of Maximum-Power-Point-Tracking Control – Power Electronics Perspective

Jyri Kivimäki

Issues in Design of Maximum-Power-Point-Tracking Control – Power Electronics Perspective

Thesis for the degree of Doctor of Science in Technology to be presented with due permission for public examination and criticism in Rakennustalo Building, Auditorium RG202, at Tampere University of Technology, on the 5th of October 2018, at 12 noon.

Doctoral candidate: Jyri Kivimäki
                        Laboratory of Electrical Energy Engineering
                        Faculty of Computing and Electrical Engineering
                        Tampere University of Technology
                        Finland

Supervisor: Teuvo Suntio, Professor
                        Laboratory of Electrical Energy Engineering
                        Faculty of Computing and Electrical Engineering
                        Tampere University of Technology
                        Finland

Pre-examiners: Giovanni Spagnuolo, Professor
                        Department of Information Engineering,
                        Electrical Engineering, and Applied Mathematics
                        University of Salerno
                        Italy

                        Pertti Silventoinen, Professor
                        School of Energy Systems
                        Lappeenranta University of Technology
                        Finland

Opponents: Jorma Kyyrä, Professor
                        Department of Electrical Engineering and Automation
                        Aalto University
                        Finland

                        Giovanni Spagnuolo, Professor
                        Department of Information Engineering,
                        Electrical Engineering, and Applied Mathematics
                        University of Salerno
                        Italy

ABSTRACT

This thesis provides a comprehensive study of the dynamic characteristics and operation of maximum-power-point-tracking (MPPT) dc-dc converters, especially for those parts that concern the MPPT-control design. The study concentrates on the widely-utilized heuristic perturb-based MPPT algorithms and their design constraints when equipped with photovoltaic-interfacing converter. The main objective is to provide an explicit formulation of the input-power dynamics of the photovoltaic-generator-interfacing dc-dc converter for addressing the MPP-tracking control. The dynamics introduce design constraints for the aforementioned MPPT-control algorithms and provide tools for deterministic MPPT design.

A photovoltaic (PV) generator has nonlinear current-voltage characteristics with a particular maximum power point (MPP), which depends on the environmental factors such as temperature and irradiation. Thus, to ensure the maximization of the power extracted from the PV source, the interfacing power converter must be capable of controlling its parameters, i.e., changing its input voltage and current levels based on the MPP of the PV generator. That is done by implementing an MPPT controller, which generates the reference control signal for the interfacing converter. Despite the way of implementation, the fundamental operation is to find the electrical operating point, i.e., the voltage and the current, at which the PV generator either generates the maximum power or follows a given power reference at every time instant. However, the dynamic characteristics of a photovoltaic generator are determined by the environmental conditions as well as the dynamics of the interfacing converter, which creates limitations for the MPPT-control design. It has been noticed recently that the characteristic curve of a PV generator can be separated into three different operation regions each having their distinct characteristics. Thus, to ensure reliability and efficiency of a maximum-power tracking, all of these regions should be analyzed separately and choose the condition corresponding to the slowest settling dynamics of the PV system. Up to now, that is not completely recognized, and deterministic analytical models are missing to provide design guidelines for the MPPT-control design.

This thesis presents a detailed dynamic model for PV-generator power dynamics in case of open-loop and closed-loop-operated switched-mode dc-dc converter. Two common design examples of closed-loop-operated converters were provided, where the closed-loop dynamics of the converter was slow and fast by adjusting the control bandwidth and phase margin of the feedback loop. With the developed models, a proper evaluation of the MPPT control imposed by the converter dynamics was presented. Thus, previously developed design guidelines were revised, or new guidelines were established.

PREFACE

Tampere, September 6, 2018

Jyri Kivimäki

CONTENTS

SYMBOLS AND ABBREVIATIONS

GREEK CHARACTERS

Δ	Relative magnitude of settling time band, determinant
η	Diode ideality factor
η_{mppt}	Maximum-power-point-tracking efficiency
$\mathcal{L}$	Laplace operator
ω_{d}	Damped natural angular frequency
ω_{n}	Undamped natural angular frequency of a open-loop-operated converter
$\omega_{\mathrm{n\text{-}c}}$	Undamped natural angular frequency of a closed-loop-operated converter
ω_{p}	Input voltage controller pole angular frequency
ω_{s}	Grid fundamental angular frequency
ω_{z}	Input voltage controller zero angular frequency
$\omega_{\mathrm{z\text{-}esr}}$	Capacitor-induced zero angular frequency
ζ	Damping factor
θ	Phase angle
τ	Time constant

LATIN CHARACTERS

$\mathbf{A}$	System coefficient matrix of the state-space representation
$\mathbf{B}$	Input coefficient matrix of the state-space representation
B	Maximum bits in an analog-to-digital converter
$\mathbf{C}$	Output coefficient matrix of the state-space representation
c_{d}	Capacitance of a PV cell
C_{dc}	DC-link capacitance
C_1	Capacitance of the input terminal capacitor
C_2	Capacitance of the output terminal capacitor
D, d	Duty ratio
D', d'	Complement of the duty ratio
ΔD	Increment in the duty ratio
$\mathbf{D}$	Input-output coefficient matrix of the state-space representation
f_{s}	Switching frequency
$\mathbf{G}$	Matrix containing transfer functions of a converter
G	Irradiance
G_{a}	Gain of the pulse width modulator

G_c	Transfer function of a controller
G_{ci}	Control-to-input transfer function
G_{cL}	Control-to-inductor current transfer function
G_{co}	Control-to-output transfer function
G_{io}	Input-to-output transfer function
G_{se}^i	Input-current sensing gain
G_{se}^v	Input-voltage sensing gain
$\mathbf{I}$	Identity matrix of the state-space representation
H	Auxiliary variable
I_{mpp}	Current of the maximum-power point
i_{pv}, I_{pv}	Current of a photovoltaic generator
ΔI_G	Incremental change in current due to variation in irradiance
ΔI_x	Incremental change in current due to perturbation step
ΔI_{pv}	Incremental change in the terminal current of a photovoltaic generator
i_d	Diode current
i_{in}	Input current of a converter
i_{inS}	Input current of non-ideal source
i_L	Inductor current
i_o	Output current of a converter
i_{ph}	Photocurrent
i_{pv}	Terminal current of a photovoltaic generator
k	Boltzmann constant or time instant
K_c	Input voltage controller gain
K_{ph}	Material constant
L	Inductance
L_{in}	Input-voltage-control loop
N	Scaling factor
N_s	Number of series-connected cells in photovoltaic module
N_p	Number of parallel-connected cells in photovoltaic module
P_{pv}	Average output power of a photovoltaic generator
ΔP_G	Power change in a photovoltaic generator due to irradiance variation
ΔP_{pv}	Incremental change in the terminal power of a photovoltaic generator
ΔP_x	Power change in a photovoltaic generator due to perturbation step
q	Elementary charge
R_{mpp}	Static resistance of a photovoltaic generator at maximum power point
R_{pv}	Static resistance of a photovoltaic generator
r_C	Equivalent resistance of an capacitor
r_D	Forward resistance of a diode

r_{L}	Equivalent resistance of an inductor
r_{pv}	Dynamic resistance of a photovoltaic generator
r_{s}	Parasitic series resistance of a photovoltaic cell
r_{sh}	Parasitic shunt resistance of a photovoltaic cell
s	Laplace variable
t, T	Time
T_{K}	Temperature
T_{s}	Switching period
T_{oi}	Reverse transfer function
T_{Δ}	Power settling time of a photovoltaic generator
$\mathbf{u}, \mathbf{U}$	Vector containing Laplace transformed input variables
v_{adc}	Voltage resolution
V_{d}	Diode threshold voltage
V_{dc}	DC-link voltage
V_{e}	Low-frequency gain of a transfer function
V_{mpp}	Voltage of the maximum power point
$v_{\mathrm{pv}}, V_{\mathrm{pv}}$	Voltage of a photovoltaic generator
V_{fs}	Full-scale voltage in analog-to-digital converter
ΔV_{o}	Amplitude of output voltage fluctuation
ΔV_{pv}	Incremental change in the terminal voltage of a photovoltaic generator
ΔV_{x}	Incremental change in voltage due to perturbation step
ΔT	Perturbation period of a maximum-power-point tracking algorithm
V_{pv}	Terminal voltage of a photovoltaic generator
$\Delta V_{\mathrm{in}}^{\mathrm{ref}}$	Incremental change in input-voltage reference
$\mathbf{x}, \mathbf{X}$	Vector containing Laplace transformed state variables
$\hat{x}$	AC-perturbation around a steady-state operation point
$\langle x \rangle$	Average value of variable x
Δx	Incremental change in a perturbed variable
y	Output variable, optimization function
$\mathbf{y}, \mathbf{Y}$	Vector containing Laplace transformed output variables
Y_{o}	Output admittance
Y_{S}	Output admittance of a non-ideal source
Z_{in}	Input impedance

ABBREVIATIONS

ac	Alternating current
ADC	Analog-to-digital converter
CC	Constant current
CCM	Continuous conduction mode
CCR	Constant-current region
CPR	Constant-power region
CVR	Constant-voltage region
CF	Current fed
CV	Constant voltage
dc	Direct current
DCM	Discontinuous conduction mode
DMPPT	Distributed maximum-power-point tracking
ES	Extremum seeking
ESR	Equivalent series resistance
GM	Gain margin
IC	Incremental conductance
LSB	Least significant bit
MPP	Maximum-power point
MPPT	Maximum-power-point tracking
OC	Open circuit
PID	Proportional integral derivative
PM	Phase margin
PV	Photovoltaic
PVG	Photovoltaic generator
PWM	Pulse width modulation
P&O	Perturb and observe
RCC	Ripple correlation control
SC	Short circuit
STC	Standard test conditions

SUBSCRIPTS

-c	Refers to closed-loop transfer function
in	Refers to input-side transfer function
max	Refers to defined maximum value
min	Refers to defined minimum value
mpp, MPP	Refers to operation at the maximum-power point
-o	Refers to open-loop transfer function
oc, OC	Refers to operation in open-circuit condition
-oco	Refers to output terminal open-circuit
out	Refers to output-side transfer function
pv	Refers to PV-generator affected function or variable
p-p	Refers to peak-to-peak value
sc, SC	Refers to operation in short-circuit condition
-sci	Refers to input terminal short-circuit
$-\infty$	Refers to ideal transfer function

SUPERSCRIPTS

-1	Inverse operator
CCR	Refers to operation in constant-current region
CPR	Refers to operation in constant-power region
CVR	Refers to operation in constant-voltage region
I	Refers to integral-controller-transfer function
PID	Refers to integral-controller-transfer function
pv	Refers to PV-generator affected function or variable
-RO	Refers to reduced-order transfer function
S	Refers to source-affected transfer function
T	Transpose

1 INTRODUCTION

This chapter introduces the background of the research, clarifies the motivation for the conducted research, and reviews the existing knowledge related to the topic.

1.1 Electricity production using renewable energy sources

Modern society has become increasingly dependent on energy. Since the *Industrial Revolution* in the late 18th century, humankind has developed alternative ways to utilize energy for power generation and electrification purposes, which have accelerated dependency of energy. Up to now, coal with its different forms has been the primary source of energy. However, excessive use of these fossil fuels increases the emissions of carbon dioxide, which have been shown to be the main contributor to the global warming. As shown in Table 1.1, fossil fuels are still dominating the world electricity generation. Thus, growing energy demand and the impact of the extensive use of fossil fuels has driven researchers to further develop renewable energy resources such as hydro, geothermal, biofuel, wind, and solar due to their lack of harmful emissions and being inexhaustible as primary energy sources [1]. As Table 1.1 indicates, hydro has already widely utilized and therefore, a significant increase is difficult to obtain. Thus, the highest potential of future electricity generation can be seen in other renewable energy sources.

Table 1.1: World electricity generation by source in 2015 [2].

Source	Coal	Natural gas	Hydro	Nuclear	Renewables (excl. hydro)	Oil
Share (%)	39.3	22.9	16	10.6	7.1	4.1

Among renewable energy sources, solar energy seems to be the most appealing alternative to fossil fuels, because it is free, clean and abundantly available [3]. Energy from the Sun is carried by electromagnetic radiation, which can be measured to be 1361 W/m^2 on the Earth's upper atmosphere [4]. A significant amount of incoming radiation is either reflected or absorbed in the atmosphere, and therefore, average irradiance on the Earth's surface can be measured to be around 1000 W/m^2. Thus, the total solar power on the surface of the Earth can be approximated to be 86 PW [5]. According to [2], world energy consumption was approximated to be 109.1 PWh in 2015, which means that the solar power can fulfill the energy demand less than one and half hour. That

energy flow can be exploited to heat water by using a solar thermal collector, or it can be converted directly into electricity by using a photovoltaic (PV) generator.

Since the beginning of PV productization, solar energy has two main disadvantages: high costs and its unpredictability. The high price of the PV system is related to their low conversion efficiency, which has prevented the extensive adaption of solar energy. Research era of modern silicon-based PV cells for energy production can be considered to be started in 1954 when a PV cell with 6 % efficiency was developed [6]. Up to now, widely utilized wafer-based crystalline silicon modules have commercial efficiencies between 14 and 24 % [7]. In recent years, the combination of increased efficiency with reduced manufacturing costs, photovoltaic energy is approaching and has already reached in some countries, so-called *grid parity*, i.e., costs becomes equal or less than the electricity generated by utilizing the conventional energy sources such as fossil fuels.

As a consequence of the price development and political decisions, the installed solar photovoltaic capacity has increased significantly in recent years. Based on the latest published reports by International Energy Agency (IEA), global cumulative PV installations continued its exponential growth reaching 303 GW by the end of 2016 indicating 50 % increase from the previous year [7] mainly due to the significant investments in the United States and Asia Pacific. Especially China and Japan, have a major contribution to the growth having over 30 % of the global cumulative PV capacity by the end of 2016.

Along with the PV power price development, PV is becoming cost competitive with fossil fuels and onshore wind power [8]. Thus, the future challenges of photovoltaic can be seen to be its uncontrollability. Photovoltaic energy has strong daily and seasonal patterns, which in turn, also has a significant variance between successive years. Up to now, the energy demand characteristics of the consumers and the availability of the solar energy do not match with each other. Therefore, the standalone PV energy systems are not feasible as such. As a consequence, the way to fully exploiting the renewable energy is the grid connection, generally at the distribution level. An adaptation of various fast varying renewable sources requires intelligently controlled power electronic converter to fulfill the requirements of the grid connections, including frequency, voltage, control of active and reactive power and harmonic minimization, for example [9].

1.2 Properties of a photovoltaic generator

The operation of PV cells is based on the photovoltaic effect, which was first observed by Alexandre-Edmond Becquerel in 1839 and later explained by Albert Einstein in 1905. The fundamental behavior of photovoltaic phenomenon inside the *p-n* junction can be summarized as the absorption of solar irradiation, the generation and transport of free carriers and collection of these electric charges at the terminals of the cell. Essentially, a basic building block of every photovoltaic system is a single PV cell, where the generated

dc current in the p-n junction is determined by the area of the cell and the amount of exposed solar irradiation. PV cells can be classified as either wafer-based crystalline, compound semiconductor, or organic. Currently, crystalline silicon technologies (single crystal and multicrystalline silicon) account for more than 90 % of the overall cell production [7].

The terminal voltage of a single cell is in the order of 0.5 V. Thus several cells need to be connected in series to form panels (also known as modules) to fulfill the voltage and power requirements of a downstream system. Commercial PV panels contain typically 30 to 60 cells connected in series, yielding panel open-circuit voltage of approximately 20– 40 V with maximum-power-point (MPP) voltage of 18–32 V, and reaching power rating from 40 W to 400 W. The amount of maximum current can be increased by increasing the cell area or by connecting cells in parallel. PV panels can be further connected in series or parallel to form a PV array to increase voltage or current output, respectively. In general, the combination of interconnected PV subsystems is called PV generator (PVG) having the same fundamental characteristics as a single cell [10].

In order to model the effect of PVG on the interconnected system, a static electrical model is required. Several PV cell models have been introduced in literature differing in complexity and implementation purposes, where two main PV models proposed are the double-diode and the single-diode models [11]. Despite the higher accuracy of the double-diode model, it is not widely adopted due to parametrization difficulty and a high computational burden [12]. Thus, a single-diode model represented in [13] and shown in Fig. 1.1, is commonly used to model the static electrical characteristics of PV cell due to the excellent compromise between accuracy and complexity. Such a simplified electrical equivalent circuit of a PV cell composes of a photocurrent source with a parallel-connected diode and parasitic elements, where a non-ideal diode represents the internal semiconductor junction, and parasitic resistances correspond to the power losses.
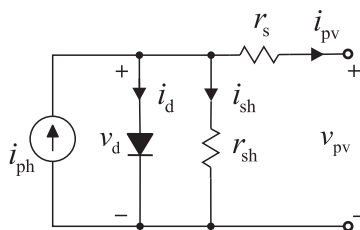

Fig. 1.1: A practical equivalent circuit of a PV cell.

An equation for PVG terminal current i_{pv} can be formed based on non-closed-form Shockley diode equation as follows

$$i_{\mathrm{pv}} = N_{\mathrm{p}}I_{\mathrm{ph}} - N_{\mathrm{p}}I_{\mathrm{s}}\left(\exp\left(\frac{v_{\mathrm{pv}} + \frac{N_{\mathrm{s}}}{N_{\mathrm{p}}}r_{\mathrm{s}}i_{\mathrm{pv}}}{N_{\mathrm{s}}\eta k T_{\mathrm{K}}/q}\right) - 1\right) - \frac{\left(v_{\mathrm{pv}} + \frac{N_{\mathrm{s}}}{N_{\mathrm{p}}}r_{\mathrm{s}}i_{\mathrm{pv}}v_{\mathrm{pv}}\right)}{\frac{N_{\mathrm{s}}}{N_{\mathrm{p}}}r_{\mathrm{sh}}}, \qquad (1.1)$$

where N_{s} denotes the number of series-connected cells and N_{p} the number of parallel-connected strings, I_{ph} is the current generated by the incident light, I_{s} is the diode reverse saturation current, q is the elementary charge, T_{K} is the absolute temperature, k is the Boltzmann constant, and η is the diode ideality factor. Clearly, due to the non-closed-formed equation, numerical computational methods need to be used to calculate PV current in respect to PV voltage. It is worth noting that the accuracy of the PV model does not solely depend on its complexity but also the identification of equivalent circuit parameters. All the parameters may be extracted by utilizing manufacturer's datasheet data [11, 14–16]. The datasheet generally gives information on the characteristics and performance in respect to the so-called *standard test condition* (STC), which corresponds to irradiation of 1000 W/m^2 at 25°C. Typically, only the values of open-circuit (OC) voltage, short-circuit (SC) current, MPP voltage and MPP current are provided, and therefore, the other parameters need to be derived.

The PV cell can be considered to be a highly non-linear current source, which has limited output voltage and power as well as distinct operation regions. The current-voltage (I-V) curve of a PV generator (cf. Fig. 1.2) contains two distinct regions separated by the MPP, which is created by the behavior of the diodes when they start conducting current along the increase in the cell terminal voltage. The operation regions are commonly categorized based on the variable, which stays practically constant within the named region. Thus, constant current region (CCR) lies at the voltage less than the MPP voltage and constant voltage region (CVR) at the voltage higher than MPP voltage. The lower boundary of CCR and the upper boundary of CVR are limited by SC and OC conditions, respectively. A PV panel operates at SC if the PV-panel voltage V_{pv} is zero and at OC if the PV-panel current I_{pv} is zero, and therefore, the PV panel does not generate any power in either of these conditions. In addition to CCR and CVR, the third region can be determined around the MPP as shown in Fig. 1.2. That is because the finite resolution of the digitally controlled measurement system will make it impossible to locate exactly the MPP, and therefore, the vicinity of MPP will form a region, which can be named as the constant-power region (CPR), as explicitly justified in Section 2.1.

Figure 1.2 also illustrates the behavior of dynamic ($r_{\mathrm{pv}} = -\Delta v_{\mathrm{pv}}/\Delta i_{\mathrm{pv}}$) and static ($R_{\mathrm{pv}} = V_{\mathrm{pv}}/I_{\mathrm{pv}}$) resistances of the PV panel. The dynamic resistance represents the low-frequency value of the PV generator output impedance, where the minus sign indicates
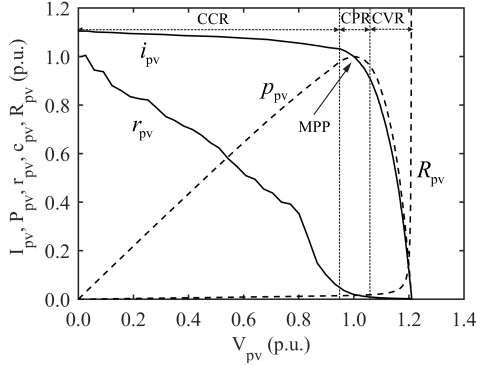
Fig. 1.2: Normalized behavior of I_{pv}, V_{pv}, P_{pv}, r_{pv} and R_{pv} when the operating point is varied.

that the current is flowing out form the PVG. As shown in the figure, the dynamic resistance is non-linear and operation-point dependent. Dynamic resistance is higher than the static resistance in CCR, whereas the relation is opposite in CVR. At the MPP, the derivative of PVG output power p_{pv} is zero, which can be represented by (1.2). Thus, static and dynamic resistances are equal at MPP as stated in [17].

$$\frac{dp_{pv}}{dv_{pv}} = \frac{d(v_{pv}i_{pv})}{dv_{pv}} = V_{pv} + I_{pv}\frac{\Delta v_{pv}}{\Delta i_{pv}} = 0 \Leftrightarrow \frac{V_{pv}}{I_{pv}} = -\frac{\Delta v_{pv}}{\Delta i_{pv}}, \tag{1.2}$$

Photovoltaic cells are highly affected by operating conditions. These are mainly the value of irradiance on a PV cell and the temperature of the p-n junction. In Fig. 1.3, two power-voltage (P-V) curves were plotted based on (1.1) with different irradiance and temperature levels scaled to per unit values for convenience. As illustrated in Fig. 1.3a, the PV-generated current is directly proportional to incoming irradiation. Thus, the maximum power can be achieved in bright sunshine conditions. The maximum power can be extracted while the PVG is operated at MPP voltage, which stays practically constant along different irradiance levels. As the figure indicates, however, the irradiance also affects slightly the OC voltage shifting the MPP voltage correspondingly. The effect is much smaller than the effect of the irradiance, and it is only noticeable at very low irradiance levels, which in turn, are not reached in practical applications due to the existing diffuse irradiance. In contrast, as can be seen in Fig. 1.3b, the temperature of a PV cell has a significant effect on the OC voltage also affecting the MPP voltage. The silicon has a negative temperature coefficient, approximately -2.3 mV/$^\circ$C, hence the maximum power is achieved at low temperature and bright sunshine conditions. In the Northern hemisphere, for instance, that means that maximum PVG power peaks can be expected in spring at the beginning of the second quarter of the year.
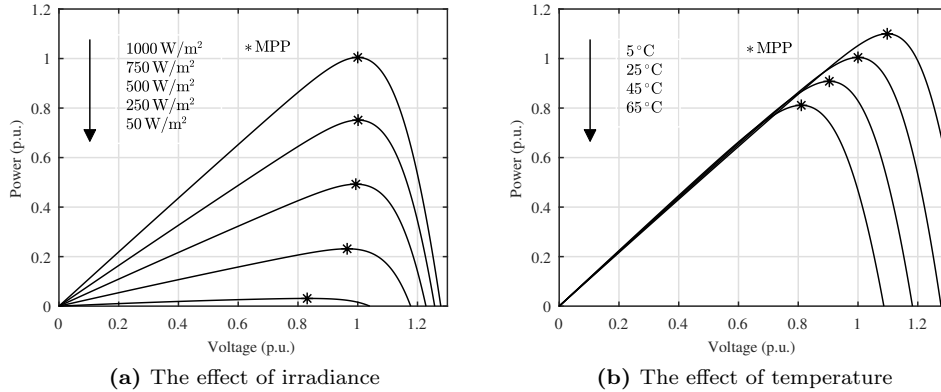
(a) The effect of irradiance

(b) The effect of temperature

Fig. 1.3: The effect of temperature and irradiance on P-V curve of a PV panel.

PV systems are prone to irradiance fluctuations caused by overpassing cloud shadows that are the main cause of fluctuating PV power production. Since the MPP voltage stays practically constant along the day, the output power of the PV system is directly proportional to the highly-varying irradiance-dependent PV current. The unpredictable behavior of the PV system is illustrated in Fig. 1.4 showing the behavior of irradiance curves during two particular days recorded on the rooftop of Tampere University of Technology. The black line represents the typical clear sky day yielding uniform parabolic irradiance distribution along the day while the irradiance is typically maximized at noon. The nominal value of the direct and diffused irradiations at the Earth's surface is considered to be $1000\,\text{W/m}^2$, but it is naturally varied depending on the atmospheric conditions and the angle of incidence of the irradiation over the location of the PV panel.

In contrast, the red line represents the half-cloudy day when the clouds are moving over the PV panels removing the direct irradiation temporarily from the spectrum of the light on the surface of the PV panels. In that case, several decreased and increased irradiance variations occur during the day indicating the problematic behavior of the varying irradiance conditions. According to [18–20], the usual and maximum irradiance slopes are considered to be 30 or $100\,\text{W/m}^2\text{s}$, while the maximum value for irradiance is considered to be STC irradiance, i.e., $1000\,\text{W/m}^2$, which are further utilized for designing MPP-tracking control, for instance. However, as shown in Fig. 1.4, these values can be exceeded due to fast-moving passing-by clouds yielding potential problems in PV systems if they are not taken into account. As the PV power production replaces more traditional non-weather-dependent power sources, power fluctuating PV systems need to be supported by other forms of electricity productions. Therefore, it is clear that PV systems increase technical requirements for the interconnected systems in order to control

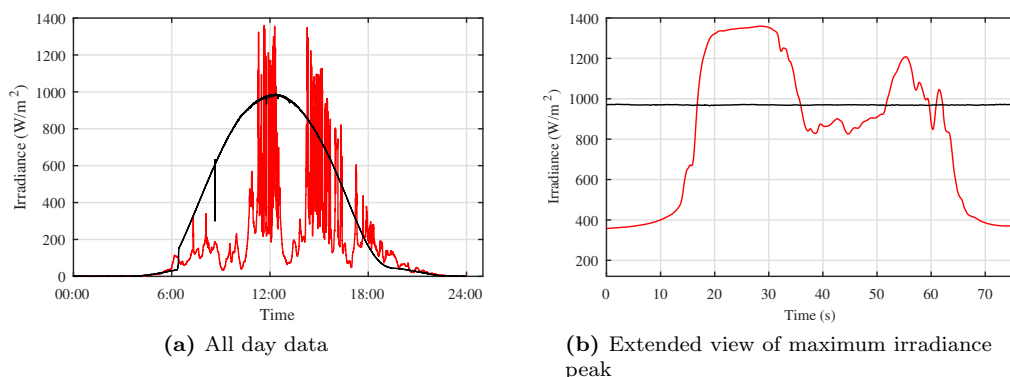the grid power according to the grid requirements [21].

(a) All day data

(b) Extended view of maximum irradiance peak

Fig. 1.4: The behavior of irradiance during particular clear-sky (black line) and half-cloudy (red line) day.

In addition to fast varying irradiance, non-uniform irradiance distribution on series-connected PV cells can cause mismatch power losses. Those mismatching conditions occur in PV system if interconnected PV cells have different electrical characteristics at the same time instant. Due to the series connection, if a single cell is shaded, the total current available from the module is limited to the value dictated by the shaded cell. Thus, the bypass diodes are needed to be connected anti-parallel with the PV cells to limit the negative voltage of a cell group to its threshold voltage enabling current to flow. Figure 1.5 represents the condition, where one-third of a PV module with three bypass diodes is shaded with different shading intensities. As can be concluded from the figure, the global MPP is found at higher voltages in low shading intensities, whereas high shading intensity causes the global MPP to be found at lower voltages making the tracking of global MPP more challenging for MPP-tracking controller [22].
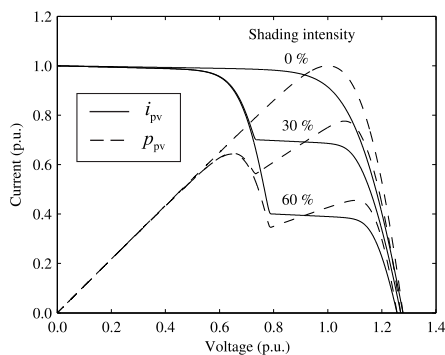

Fig. 1.5: I-V and P-V characteristics of a PVG in partial shading condition.

7

1.3 DC-DC converters in photovoltaic systems

In the field of modern electrical engineering, power electronic converters are an essential part of the integration of distributed generation unit in order to achieve high efficiency and performance in power systems. Typically, these power electronic converters are based on the switching actions, in which energy is periodically stored into the magnetic or electric field of inductors and capacitors, respectively. Periodic behavior is forced by controlling on and off time of the switch (or switches) in order to achieve desired power conversion between the source and the load with theoretically zero losses. The practical systems, however, introduce losses, which can be expected to be accountable for a couple of percents up to twenty percent of the full system power due to various loss mechanisms in the electronic components.

PV power systems can be divided into stand-alone and grid-connected systems. As the terms indicate, stand-alone PV systems are independent of electrical grids, whereas grid-connected PV systems are power plants feeding their energy into electrical grids. Nowadays, majority of the built PV systems, up to 99 %, can be considered to be grid-connected PV systems due to the technical development of grid-connected converters, reduced costs combined with incentives of local regulations [3]. Those grid-connected PV power electronic converters have two main tasks to fulfill: In addition to the requirement of the grid-connected power electronic converter to transform dc voltage from the PVG to suitable ac current for the utility grid, they need to be able to control the output voltage of the PVG in order to perform maximum-power-point tracking (MPPT) for maximizing energy yield [9]. In addition, modern PV converters have several grid-supporting features related to security and power control as well.

In grid-connected PV systems, the final stage in the power conversion chain is the grid-connected inverter, which enables power transfer from a dc source into an ac load. The conversion can be implemented either with one or two-stage conversion scheme [23]. Different configurations can be used to implement the conversion, typically divided into four different configurations: string, central, multistring and module-integrated inverter as depicted in Fig. 1.6 [9, 23].

In the single-stage scheme, as shown in Figs. 1.6a and 1.6b, the PVG is directly connected to the input of an inverter, which feeds the ac voltages and currents to the grid. In that case, the inverter is controlling its dc-link voltage to perform MPPT, and therefore, forcing the system to operate at the MPP of the PV array. A single-stage inverter requires that the PVG voltage is higher than the peak ac voltage value due to the inherent step-down characteristics of the inverter bridge. Therefore, series-connected PV modules need to be connected into parallel strings to fulfill voltage and power requirements for the grid. Figure 1.6b illustrates the central inverter topology, which is widely utilized in the past. It is mainly used in megawatt-scale PV systems since large
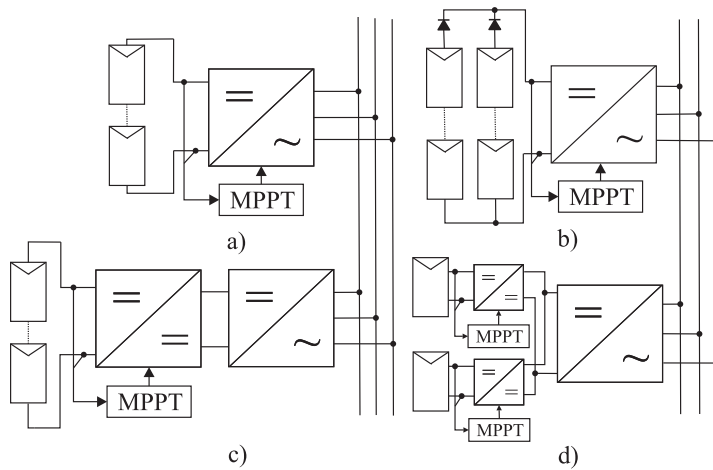
Fig. 1.6: Common PV system configurations (a) string inverter (b) central inverter (c) string inverter with two-stage conversion (d) modular system.

inverters have a low price-per-power ratio due to the lowest number of power conversion stages [24]. The PV array is formed by connecting separate strings in parallel using a blocking diode in series with each string. These string blocking diodes can be used to prevent reverse current, which could damage shaded strings in partial shading conditions as discussed in Section 1.2. This approach is efficient and effective only when MPP current levels are well matched. Thus, it has substantially reduced power output when even one segment is degraded. As a reduced version of central inverter topology, the string inverter topology shown in Fig. 1.6a utilizes one-string-per-inverter approach improving tolerance of partial shading conditions. Such a PV configuration uses a distributed approach by providing each parallel string with an individual MPP tracking converter. In this way, the strings can be forced to operate at their MPP despite the partial shading occurring in one of the parallel strings, thus, increasing the total power fed into the grid. With the increased costs of the inverters, the system modularity can be greatly increased enabling modifications into the existing system.

In contrast to the single-stage approach, the two-stage scheme is based on cascaded dc-dc and dc-ac converters as illustrated in Fig. 1.6c. The dc-dc converter stage controls the PVG voltage via the MPPT algorithm while the inverter retains dc-link voltage constant. By adding a voltage-boosting dc-dc converter between PVG and inverter, usable voltage range can be expanded, and therefore, less series-connected photovoltaic cells and modules are needed to be connected in series. That reduces the maximum voltage stress of the inverter components enabling the use of switches with a lower voltage rating. In addition, the two-stage conversion scheme offers other advantages over single-stage scheme such as increased performance of the MPPT, galvanic isolation, better

attenuation of the double-line-frequency voltage ripple and easy implementation of energy storage for attenuating power fluctuations in grid-connected PV systems favoring it to future PV systems.

In two-stage conversion scheme, double-line-frequency voltage ripple can be effectively mitigated without the need to increase input capacitor. In grid-connected single-phase systems, the output power of inverter fluctuates at twice the grid frequency causing double-line-frequency voltage ripple in the PVG output terminals. Sinusoidal voltage ripple in the PVG terminals deviates the operating point from the MPP yielding additional energy losses and incorrect operation of MPPT algorithm [23, 25, 26]. Typically, in single-stage configurations, dc-link voltage control bandwidth is designed to be at very low frequencies, up to 10 Hz, in order to achieve sufficient attenuation of voltage ripple, which may cause the corresponding grid-current harmonic components. Moreover, it may be required to increase the capacitance value of the dc-link capacitor. Thus, the speed of the MPPT is limited up to a few hertz due to the constraints of cascaded control loops making the system slow to react to sudden changes in atmospheric conditions. In contrast, in case of the two-stage configuration, the input-voltage control loop bandwidth of the dc-dc converter can be designed much higher for reducing voltage ripple effectively without large input capacitor for power decoupling and enabling faster response for MPPT with the increased energy yield. Moreover, PV system can be commanded via MPPT to perform fast power curtailment, where only a certain amount of power is transferred into the grid to prevent overvoltage or complying with the other grid requirements [27–29].

Figures 1.6a-1.6c represent the so-called centralized PV system configurations. Several solutions are introduced to overcome the drawbacks associated with mismatching phenomena in PV applications such as implementing global MPPT for traditional centralized inverters, reconfiguring interconnections between the PV panels and utilizing module-dedicated dc-dc and dc-ac converters. Despite the improved efficiency of centralized PV topology with global MPPT or reconfiguration approach, those architectures still cannot utilize all available energy of the PV generator, i.e., such power is lower than the sum of the maximum available powers that the mismatched modules can provide. Therefore, energy loss due to mismatch losses has driven significant interest in distributed power electronics, including micro-inverters and distributed dc-dc topologies.

Due to the series connection, each module has to carry equal current, which may force the operating point of the other modules away from the MPP. Thus, distributed MPPT (DMPPT) systems have been proposed, where each PV module has a dedicated interfacing converter. Basically, two different DMPPT approaches are developed: The first one is based on the adaption of module-dedicated dc-ac converters, called micro-inverters, and realizing the MPPT for each PV module. In contrast, the second approach

relies on the use of module-dedicated dc-dc converters, realizing the MPPT for each module and centralized inverters. DMPPT converters are the first part of a two-stage conversion chain, where the dc power produced by the PV modules is interfaced into the ac utility grid using an inverter. Typically, there are some individual converters transferring power into the common dc link. As a consequence, the P-V curve of a string of PV modules equipped with own dc-dc converters will have only one MPP, since all PV modules in the string are forced to behave as a PV module with average output power. That makes finding the MPP much more straightforward for the string inverter, as opposed to the case without an individual dc-dc converter, where the differences in output power between the modules lead to multiple MPPs.
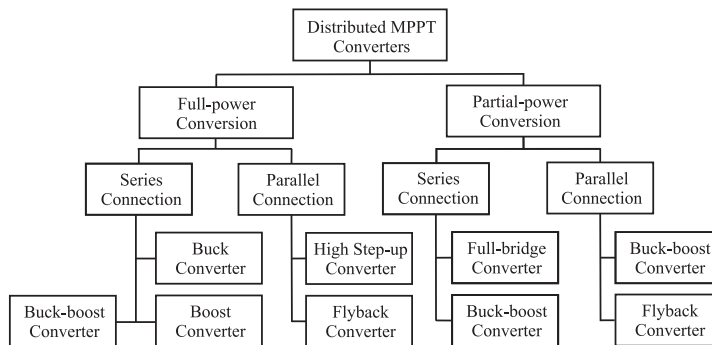
Fig. 1.7: Classification of PV module integrated dc-dc converter concepts into full-power and partial-power processing converters (redrawn from [30]).

These modular DMPPT systems can be further categorized as full-power and partial-power converters as illustrated in Fig. 1.7 with the common converter topologies [31–33]. As the name indicates, full-power converters process the entire PV power generated by its associated PV module regardless of shading conditions. In contrast, partial-power converters process only a small fraction of the generated power to balance the operating point of the modules. This feature enables several advantages, but most importantly, the effective conversion efficiency and power density can be much higher than in the series-connected power electronics due to the need for lower average power handling. The main idea of the concept is to enable module-level dc-dc converters only when differences between PV modules or their substrings occur. That limits the operation time of the converters, and therefore, has a positive impact on reliability. When active, the converters only operate on differences in power, while the bulk of the power is still delivered by the regular series-connected string of PV modules. That implies that the efficiency of the converters has less impact on the total system output power, and therefore, cheaper converters with lower efficiency can be used.

1.4   Maximum-power-point tracking in photovoltaic applications

Despite the chosen PV system configuration, they all need to have an MPPT controller implemented into their control system in order to extract the maximum amount of energy from the PVG. By connecting a PVG directly to the input port of the power processing system with a constant voltage would be a simple but very inefficient solution from the energy production point of view. If an interconnected converter is designed to maintain its input terminals at a constant voltage, this essentially forces a PVG to operate at the voltage determined by the converter. As discussed in Section 1.2, the MPP of the PVG has very non-linear characteristics causing the global MPP to vary widely as a function of irradiance, temperature and the level of mismatching during the lifetime of PV system. Therefore, it is impossible to determine a single operating point that would yield acceptable energy yield during the whole lifetime of PVG. In the worst case, the atmospheric conditions can vary so that the operating point is moved to SC or OC condition resulting in zero energy production.

Thus, in order to ensure the maximization of the power extracted from the PV source, the interfacing power converter must be capable of controlling its parameters, i.e., changing its input voltage and current levels based on the MPP of the PVG. That can be done by implementing an MPPT controller, which generates the reference control signal for an interfacing converter. Despite the way of implementation, the fundamental operation is relatively simple: To find the electrical operating point, i.e., the voltage and current, at which the PV module generates maximum power at every time instant. Basically, the majority of the introduced MPPT algorithms are focusing on maximizing the power output of the PV module yielding also the maximized output power in practical PV-interfacing converters.

MPPT controller can also be modified to limit the output power of the PV inverter to prevent overvoltage and inverter tripping in distribution grids with high PV penetration [28, 34]. As the share of the electricity produced by PV power plants increases, it becomes more important to implement grid-supporting functions in the PV inverters. Due to a non-controllable nature of the power source, PV systems can create overvoltages in distribution feeders during the periods of high power generation and low load due to reverse power flow [35]. The problem occurs especially in so-called weak grids having low short-circuit current. That is usually prevented by limiting the penetration level of PV to very conservative values or implementing voltage-frequency or active-power-reactive-power droop control methods similarly as with the traditional synchronous generators in order to balance the power flow between the source and load [36, 37]. Alternatively, some recent studies have been focused to convert an MPPT controller to perform the same tasks [28, 29, 38]. Instead of maximum power, a power output reference is given for the MPPT controller, which changes the operating point on the P-V curve correspondingly. In order

to utilize such a constant power generation in fast varying environmental conditions, two-stage conversion might be compulsory providing fast enough tracking performance and wider voltage range for PVG [28].

In addition to the electrical MPPT, the produced energy can be further maximized by utilizing so-called *solar tracking*. PV panels are normally installed at a fixed inclination angle towards the Sun at which the normal of the module surface is maintained towards the Sun as much as possible. Because solar altitude and azimuth vary over the course of any given day, a complex bi-axial solar tracking mechanism is needed to maintain this solar-radiation-maximized state, which can increase energy yield by roughly 25 to 40 % [10]. However, due to the increased demand for space combined with increased installation and maintenance costs of a solar tracking system, they seem not to be profitable enough in the era of steadily decreasing prices of PV panels.

1.4.1 Overview of existing methods

MPPT algorithms have been widely studied in recent decades [18, 39–41]. Up to now, over 7000 articles have been published solely on the popular IEEE Xplore research database indicating its importance and interest among PV systems. The developed MPPT techniques can be divided into indirect and direct techniques referring to the method how the MPP is evaluated. The indirect methods are based on the prior knowledge of the PVG, and they do not measure the extracted power directly from PVG but rather estimate the MPP based on a single measurement of voltage or current. On the contrary, direct MPPT techniques utilize both voltage and current measurements to calculate the PV power being independent of the prior knowledge of the PVG characteristics.

The indirect methods are usually based on the approximate knowledge on the location of the MPP through the *fill factor* (FF) of the PV array by measuring the short-circuit current I_{sc} and/or open-circuit voltage V_{oc}. The maximum power extracted from the PVG is always lower than the value obtained by multiplying short-circuit current by open-circuit voltage $P_{\max} = I_{\mathrm{sc}}V_{\mathrm{oc}}$, thus yielding the ratio known as FF, which can be defined as [42]

$$\mathrm{FF} = \frac{I_{\mathrm{mpp}}V_{\mathrm{mpp}}}{I_{\mathrm{sc}}V_{\mathrm{oc}}}. \tag{1.3}$$

The fill factor for commercially available solar cells varies typically within the range of 0.6–0.8 [10]. Under uniform irradiation, only one MPP exists with the corresponding values of MPP current I_{mpp} and voltage V_{mpp} with relatively linear dependency with short-circuit current and open-circuit voltage, respectively. Such a approximation is utilized in MPPT techniques called *fractional open-circuit voltage* and *fractional short-*

circuit current methods. There, a fixed coefficients ($k_1 \approx V_{\mathrm{mpp}}/V_{\mathrm{oc}}$ or $k_2 \approx I_{\mathrm{mpp}}/I_{\mathrm{sc}}$) are determined from the prior knowledge of the PV panel in order to approximate the location of the corresponding MPP values [43]. That naturally requires interrupting the energy supply during the measurement of the desired variables. It is worth noting that these methods would very seldom give the exact location of the MPP but only its rough estimation. However, these methods perform sufficiently well as long as there is only a single MPP. In case of partial shading condition, where the global MPP is found at lower voltage levels (cf. Fig. 1.5), the coefficients are not valid anymore. Moreover, they seem to be effective with the combination of direct MPPT techniques by providing an initial operating point for the system before more accurate MPPT algorithm is executed.

On the contrary to indirect computational MPPT techniques, the most widely utilized MPPT algorithms are based on heuristic search approaches, which aim to simplify the process and to make the prior knowledge of PV module characteristics unnecessary [39]. Those methods are typically based on injecting a small perturbation in the control variable of the interfacing power converter and observing the effect of voltage and current of the PVG to locate the MPP. Various perturbative algorithms have been introduced differing either from the observed variable or the type of perturbation. The basic and most popular form of perturbative algorithm is *perturb & observe* (P&O) (also known as *hill climbing*) and *incremental conductance* (IC) techniques, which are based on perturbing the PVG operating point periodically via switched-mode converter with a fixed step-wise perturbation step and observing the effect in power or in conductance $\Delta i_{\mathrm{pv}}/\Delta v_{\mathrm{pv}}$ of consecutive operating points. Furthermore, different perturb-based algorithms have been introduced such as *extremum seeking* and the *self-oscillation method* based on the sinusoidal perturbation.

Extremum seeking (ES) and the ripple correlation control (RCC) techniques are based on the detection of low and high-frequency oscillating components of a converter, respectively. In grid-connected PV applications, the dc-link voltage fluctuation can end up to PVG terminals, where ES can use the 100 Hz voltage ripple component for tracking the MPP. Using the information that the amplitude of sinusoidal disturbance minimizes at MPP, the operating point can be forced to MPP by observing the amplitude of the ripple. [44] In contrast, RCC utilizes the high-frequency ripple generated by the switching action to perform MPPT [40]. Basically, since the time derivative of the power is related to the time derivative of the current or of the voltage, the power gradient is driven to zero indicating that the operating point matches the MPP.

In addition to the perturbative algorithms, increasing computational performance have made the soft computing methods such as *fuzzy logic* and *neural network* based algorithms popular for MPPT over the last decade in different PV applications [40, 45]. The advantage of such techniques is that they handle the nonlinearity well, and

therefore, they are very suitable for nonlinear power maximization task. Unfortunately, general rules how to select optimal values do not exist. In fuzzy logic controllers, the performance is highly depended on choosing the right error computation and rule base table. Therefore, a lot of knowledge is needed in choosing right parameters to ensure optimal operation. In contrast, the neural network strategies require specific training for each type of PVG since the input variables can be any of the PV cell parameters such as open-circuit voltage, short-circuit current or atmospheric data, for instance. Moreover, due to the highly nonlinear behavior, it would be very challenging to model its dynamical effect on the rest PV system.

The MPPT algorithms designed for uniform irradiance conditions may be stuck in partial shading condition, where the MPPT is operating in the neighborhood of a relative MPP instead of that close to the absolute MPP reducing the energy yield of system [46]. That is a problem especially in the cases, where the global MPP is at the lower voltage, yielding the higher voltage difference between the unshaded and partially shaded situation as demonstrated in Fig. 1.5. Therefore, there has been a lot of research related to the development of global algorithms [47]. In order to prevent such behavior, global MPP-tracking requires more intelligent algorithms, which can distinguish a local MPP from the global one in varying atmospheric conditions. The global MPPT algorithms are typically based on scanning the whole P-V curve and then alternatively using local MPPT algorithms such as perturbative algorithms for fine adjusting [48]. The scanning can be performed by using the current sweep method to sweep the operating point from open-circuit to short-circuit condition. The main disadvantage is that energy is lost every time the search is performed. The more intelligent approaches to performing P-V curve scanning can be done when utilizing the knowledge about the system and operating conditions. For example, the proposed method in [49] uses the information that the minimum distance between two local MPPs is the MPP voltage of the shaded series-connected PV cells connected in anti-parallel with a bypass diode.

1.4.2 Reliability and efficiency of maximum-power-point tracking

The reliability of a PV system depends on several factors of which the most important ones can be listed as i) issues related to PV system configuration and interconnected converters in hardware level ii) control system design in each respective conversion stage and iii) climatic variance in the respective area [50]. The performance of MPPT is falling in the second and third category affecting both stability and efficiency of the system. Thus, it has been observed to have a significant contribution to the reliability problems in photovoltaic energy systems.

Essentially, the improvement of electrical efficiency is the primary issue in all PV systems regardless of the application. Compared to the other industrial sources of electricity,

PV panels have low conversion efficiency combined with its relatively high initial price. Thus, they should be operated at the maximum available power to reduce the time of return on investment. In that regard, the chosen MPPT algorithm has an essential role in any PV system, and it should have high MPPT efficiency η_{mppt}, i.e., the ratio between actual gathered energy and maximum energy available from the PVG. Several efficiency comparison reviews have been published between different MPPT techniques highlighting their tracking abilities under steady-state or dynamic atmospheric conditions. However, the value of the outcome of those reviews is often questionable since the comprehensive review would require the deep understanding of the MPPT algorithm and interconnected PV system to optimize design parameters. Typically, only the steady-state behavior of the converters is taken into account despite the fact that dynamic behaviors have a significant impact on the efficiency and reliability of the operation of MPPT algorithms.

Fast growing installations of grid-connected PV systems have highlighted some power quality problems caused by PV inverters [51–54]. Recent studies have revealed that large-scale adaption of grid-connected PV inverters may be one contributor to the increasing inter-harmonics appearing in the grid currents, causing voltage fluctuations and light flicker as stated in [52]. One of the sources of inter-harmonics is related to unoptimized perturbative MPPT algorithms yielding power quality problems. Origin of the harmonics is observed to be the step-wise operation of P&O algorithm generating harmonic frequencies, which are dependent on the perturbation step size [53].

Focusing on the widely adapted P&O algorithm, its MPPT efficiency can be approximated by analyzing the basic operation principle of the algorithm. The P&O method is generic by its implementation, and therefore, it can be adapted to various applications by choosing the optimization function $y(t)$ and perturbed variable $x(t)$ correspondingly. In its simplest form, it is very suitable for finding the MPP for PV or wind power application [55] on the uniform P-V curve, for instance. There, a perturbation Δx is injected into the system by the MPPT algorithm every ΔT seconds as illustrated in Fig. 1.8a. After perturbation, the polarity (and sometimes size) of corresponding optimization function (i.e., the PVG power in the P&O method and sum of static and dynamic conductances in the IC method) change $\Delta y(k) = y(k) - y(k-1)$ is detected. Thus, the next perturbation $x(k+1)$ is updated based on (1.4). In this respect, two design parameters are perturbation frequency (i.e., the inverse of time interval ΔT between two consecutive perturbation instants) and perturbation step size Δx.

$$x(k+1) = x(k) \pm \Delta x = x(k) + \Delta x \cdot sign(y(k) - y(k-1)) \qquad (1.4)$$

Despite the generic approach of the P&O algorithm, its design parameters are not generic. Thus, its parameters need to be optimized for the specific application by taking
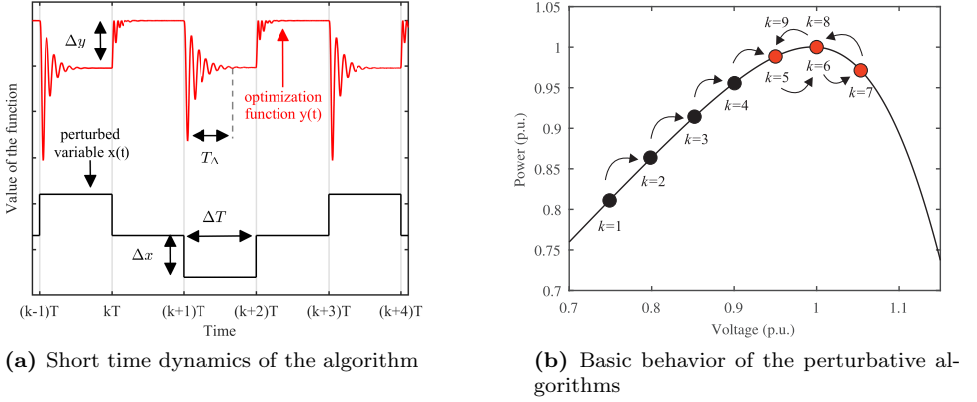
(a) Short time dynamics of the algorithm

(b) Basic behavior of the perturbative algorithms

Fig. 1.8: A demonstration of the basic operation principle of the fixed-step P&O MPPT algorithm.

into account the dynamic behavior of the interfacing converter and changes in atmospheric conditions to maximize the energy yield from the source and to ensure proper operation of the system as discussed comprehensively in [18]. The reasons for the errors can be the change of irradiance level, the ripple of the measured variables, or the transient settling process of the corresponding power electronic converters.

Figure 1.8b illustrates the basic operation behavior of the algorithm in PV system starting from CCR, which locates at the lower voltage level. According to (1.4), where $y(k) = P_{pv}(k)$, the change of consecutive power measurements is positive towards the MPP as long as the time instant $k = 7$ is reached. After the MPP, $P_{pv}(k = 6) - P_{pv}(k = 7) < 0$ and the sign of the perturbation is reversed yielding three-point operation behavior highlighted in red dots. Due to the discrete operating point changes in perturbative MPPT techniques, the system cannot exactly reach and maintain the operating point at MPP but rather oscillating around it causing so-called *limit cycle oscillation*. These steady-state oscillations are a common problem in the perturb-based MPP-tracking devices leading to reduced MPPT efficiency and even power quality issues discussed later.

If the three-point operation of the P&O algorithm is guaranteed in all atmospheric conditions (i.e., the combination of perturbation step size and frequency have been chosen carefully), the MPPT efficiency is solely determined by the perturbed PVG-power change ΔP_x caused by the perturbation step size Δx. Thus, the MPPT efficiency for the PV system operated under the fixed-step P&O algorithm can be approximated as follows [18]

$$\eta_{mppt} = \frac{\int p_{pv}(t)dt}{\int P_{mpp}(t)dt} = \frac{2P_{mpp} + 2\left|P_{mpp} - |\Delta P_x|\right|}{4P_{mpp}} = 1 - \frac{|\Delta P_x|}{2P_{mpp}}. \tag{1.5}$$

17

Therefore, while these three points lie relatively close to each other, the P-V curve in the vicinity of MPP can be modeled with parabolic approximation and the MPPT efficiency can be approximated based on the perturbed PV-power step size. Clearly, the perturbation step size should be chosen as small as possible to maximize MPPT efficiency. Up to 99.8 % MPPT efficiencies have been measured from experimental systems as reported in [56] indicating that such an algorithm can yield very high MPPT efficiency if the design parameters are properly chosen.

Perturbation step size cannot be reduced to an arbitrarily low value due to varying irradiance and noise in the measurement circuit affecting the accuracy of two consecutive PVG-power measurements. The erratic operation of the perturbative algorithm under varying irradiance condition can be explained by inspecting Fig. 1.9a, where the present operating point is at point A, and the sign of the next perturbation step is leftwards, i.e., to lower voltage level. If irradiance is increasing during the MPPT perturbation period, the new operating point moves from A to C instead of A to B. However, this is not a problem, since the power change caused by the perturbation is larger than the power change caused by the irradiance change corresponding to $P_{pv}(k+1) - P_{pv}(k) < 0$. Therefore, the sign of the next perturbation is inverted, i.e., the voltage is increased and the operating point converges towards the MPP. In contrast, the false response to the changing irradiance condition is illustrated in Fig. 1.9b. The starting point is the same as in Fig. 1.9a, the operating point is located at point A, and the sign of the next perturbation is leftwards. Due to the changing irradiance level between the perturbation periods, the operating point is moved from A to C. In this case, the sign of the next perturbation is calculated as $P_{pv}(k+1) - P_{pv}(k) > 0$ and the direction of next perturbation is leftward indicating the wrong operation of the MPPT algorithm. Such behavior will occur as long as the irradiance transition lasts, and eventually, the operating point will move towards OC or SC condition. In order to prevent such behavior, the perturbation step size should be designed to be high enough to provide power change in PVG terminals to overcome the power change caused by the irradiance variation within the same time interval as stated in [57].

In addition to fast-changing irradiance, different noise sources affect the operation of the perturbative algorithms. The most significant ones are the switching ripple noise, the measurement errors, the errors in numerical elaboration, and the output voltage noise [18]. As a consequence, the computed PVG power may not correspond to the real PVG power yielding an unpredictable operation of the MPPT algorithm. Thus, to guarantee the operation similar to represented in Fig. 1.8, all the noise sources that can affect PVG power should be analyzed and increase the perturbation step size Δx correspondingly. Each noise source needs to be studied separately and their effect is added together to achieve the minimum required perturbation step size [18].
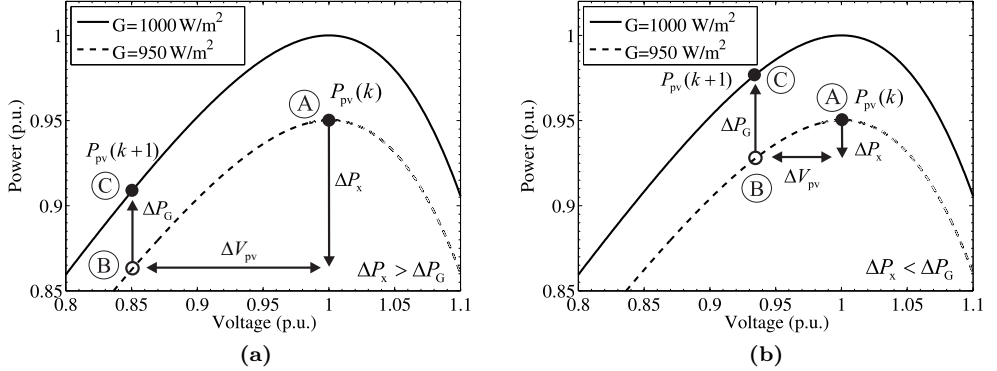
Fig. 1.9: Demonstration of (a) proper operation and (b) false operation of perturbative algorithms in fast-changing irradiance condition. [58]

Despite the fact that the effect of minimum perturbation step size is widely recognized in the literature, the upper limit also exits as recently revealed in [59]. That is because an open-loop and closed-loop interfacing converter may operate with relatively low damping factor, which causes oscillation during the transients. The undamped resonant behavior introduces overshoot also in the transient behavior of the inductor current. Therefore, if the perturbation step size Δx is too large, the inductor current can move from continuous conduction mode (CCM) to discontinuous conduction mode (DCM). That transforms the second-order system into an equivalent first-order dynamic system extending the PV-power settling time significantly, thus, reducing power tracking performance and violating the validity of the theory to compute the power settling time in the previous studies [57, 60, 61], which will be further discussed in Section 4.4.

Adaptive and variable-step algorithms are introduced to overcome the trade-off situation between the steady-state oscillation and fast dynamics in fixed-step perturbative algorithms. The conventional concept of an adaptive-step algorithm is based on varying the step size of the perturbation while the perturbation frequency is kept constant. Basically, the algorithm adjusts the step size Δx depending on how far the operating point is from the MPP. When the present operating point is far from the MPP, a large step size is used to achieve the MPP faster. In contrary, a small step size is used when operating near the MPP to minimize steady-state oscillations. In order to calculate the value of step size, the power-voltage derivative $\Delta P_{pv}/\Delta V_{pv}$ is typically chosen as a suitable parameter for tuning the step size [62] since its value reduces when the operating point moves towards the MPP yielding ideally zero at the MPP. The main problem with the algorithm is to find a suitable scaling factor for $\Delta P_{pv}/\Delta V_{pv}$ and the minimum perturbation-step-size limits in order to satisfy the constraints discussed before.
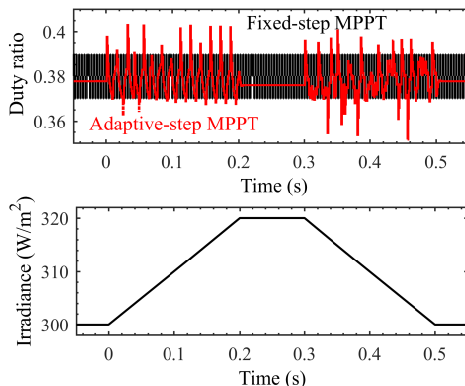
19

Fig. 1.10: Simulated operation of adaptive-step MPPT (red line) and fixed-step MPPT (black line) under trapezoidal irradiance profile shown on the bottom figure [58].

Adaptive-step P&O algorithms are very sensitive to drift due to the derivate-dependent perturbation step size. Figure 1.10 highlights the problems with variable-step algorithms originally published in [58]. In the figure, fixed-step and adaptive-step P&O algorithms are compared to varying irradiance profile shown in the lower figure. Based on the simulation in Fig. 1.10, the varying irradiance causes the algorithm to drift on both sides of the MPP with unpredictable behavior. In contrast, the perturbation step size in the fixed-step MPPT algorithm is chosen large enough to compensate irradiance variation, and therefore, the MPPT control operates with the basic three-step behavior. Therefore, as concluded in [58], the adaptive-step MPPT algorithms are very sensitive to noise, and therefore, additional mechanisms should be added to the algorithm to prevent drift phenomenon.

The second design variable of the perturbative algorithms is the perturbation frequency, i.e., the period between two consecutive perturbations. As Fig. 1.8a indicated, the undamped converter topologies exhibit resonant behavior in the transient conditions, which extends the settling process of PVG voltage and current also affecting PVG power. Therefore, the perturbation period ΔT should be longer than the longest settling time of the PVG output power transient induced by the injected perturbation, i.e., $\Delta T > T_\Delta$ must hold throughout the whole operation range, otherwise the algorithm may fail and the operating point can enter into chaotic behavior and lose its predictability [57]. As can be seen from Fig. 1.8a, the transient behavior changes according to the operating point. Thus, all operation regions should be studied to determine the conditions, where the settling time is the longest.

Even though different MPPT algorithms have been widely studied in the literature, their dynamic behavior is mostly neglected. The first detailed studies regarding the

optimization of the P&O algorithm design parameters are presented in [57], where the authors generated a dynamic model for the PVG-interconnected boost converter in order to determine the minimum settling time to prevent the drift phenomenon. However, alternative approaches are also introduced. The authors in [63] recommended to use 1/10 of the input-voltage-feedback-loop crossover frequency as the base for computing the PV-power-settling time. However, as reported in [60], the settling time of the transient cannot be determined solely by the control bandwidth since the damping factor and the phase margin have also a great impact on the outcome. Later, a few other studies have given simplified guidelines to determine an optimized value for perturbation frequency and step size. For example, the authors in [64] suggested that the speed of the MPPT algorithm should be in the range of 0.1–1.0 % of MPP voltage per second in order to reach annual MPPT efficiency of 99.9 %. The other approaches have been introduced by the authors in [65] utilizing shorter perturbation period. In that case, the PVG power never reaches the steady state yielding chaotic behavior around the MPP. Despite the interesting approach, such a high-frequency perturbation cannot be used in multi-loop converter control scheme due to the constraints of control bandwidths between outer and inner control loops.

It must be emphasized that the design guidelines represented in [18] and [57] seem to be generalized and intended for both open-loop and closed-loop MPPT structures. Nevertheless, there is no evidence in the literature (including [18] and [57]) of applying these to systems employing closed-loop MPPT structures. For example, the authors of [26] recommend determining the minimum allowed perturbation period by means of simulations rather than analytically. Consequently, the thesis aims to fulfill the gap by demonstrating that in case the input-voltage feedback loop is properly closed, PVG-power-settling time would be independent of PVG dynamic resistance, thus being longest in CPR. Revealed analytical findings are experimentally validated by utilizing a PVG-interconnected dc-dc converter [66].

Although the perturbation frequency does not directly affect the tracking efficiency, it has a significant impact on the operation of the algorithm in steady state and dynamic atmospheric conditions. That is because the perturbation frequency defines the tracking performance (i.e., power ramp rate $\Delta P_{pv} \Delta T$) under dynamic conditions together with the perturbation step size. Thus, these two design parameters of the perturbative algorithm should be selected carefully by taking into account dynamic behavior of the interfacing converter, possible noise sources affecting the PVG-power measurements and varying atmospheric conditions under the worst case scenario.

1.5 Objectives and scientific contributions

This thesis discusses the dynamic characteristics and operation of MPP-tracking dc-dc converters, especially, on those parts that are valid for MPPT-control design by continuing the previous work around the subject in [67]. By analyzing the published research results, it can be concluded that the given perturbative MPPT algorithm design guidelines were either insufficient or missing in some parts. As a consequence, revisited and new methods to analyze PVG-power transients in case of open-loop-operated and closed-loop-operated dc-dc converters were introduced. Studies were performed with a voltage-boosting dc-dc converter. However, the fundamental principles behind the developed methods will remain the same with other converter topologies. Thus, the results provide practical methods to estimate the factors affecting the PVG-power transient in order to facilitate the MPPT design process as well as the design of the interfacing converters.

The main scientific contributions of this thesis can be summarized as follows

- Providing an explicit formulation of PV-generator power dynamics when interconnected with a switched-mode dc-dc converter. It is shown that the operating point can move from CPR to CCR even during the steady-state MPPT operation, leading to a longer PVG-power-transient-settling time than the one expected at MPP. Consequently, unlike stated in the design guidelines utilized so far, the perturbation frequency design of direct MPPT control must be accomplished for the worst-case operating point expected to be in the constant current region rather than at the MPP in the case of duty-ratio-operated converters.

- Providing revisited-perturbation-frequency design guidelines to be invariant to the PVG during the perturbation frequency design process. Once the operation in the constant current region is assumed as the worst-case operating point, it was revealed that photovoltaic-generator influence on the perturbation frequency value vanishes and the perturbation frequency could be computed based solely on the dynamic behavior of the duty-ratio-operated interfacing converter.

- It has been shown that the dynamic behavior of the input-voltage-controlled converter does not depend on the properties of the photovoltaic generator, contrary to the duty-ratio-operated MPPT converter. Consequently, the settling time is longest when the operating point resides in constant power region due to the behavior of the PV-power settling process. Therefore, it is recommended to use the constant power region related equations to compute the settling time in the case of multi-loop MPPT structures employing inner input-voltage-feedback control.

- Introducing a method to estimate the transient behavior of input-voltage-feedback-controlled MPPT converters for two typical design cases by focusing only on the

fundamental components related to the settling process. It has been shown that settling time of PVG voltage and power can be estimated accurately by means of the crossover frequency and phase margin of the input-voltage feedback loop only.

- It has been shown that MPP-tracking diode-switched dc-dc converters can move from continuous-conduction mode to discontinuous-conduction mode during the normal MPP-tracking operation if the perturbation step size of the MPPT algorithm is designed to be too large. That extends the PV-power settling time process reducing the MPP-tracking performance and violates the validity of the existing theory developed for PVG-power settling-time estimation for open-loop and closed-loop operated dc-dc converter. Thus, a method is introduced to determine the maximum-step sizes for duty ratio and input-voltage reference under open-loop and closed-loop operation.

1.6 Related publications and author's contribution

The ideas presented in this thesis are published in the following scientific publications [P1]-[P6] forming the basis of the thesis. All the publications are mainly contributed by the author. Prof. Suntio was supervising the research documented in [P1]-[P6]. He also introduced valuable ideas and comments related to the conducted research. Dr.Tech. Viinamäki gave great support for building the prototype dc-dc converter used for the measurements in the all publications. Prof. Kuperman introduced valuable ideas in [P1]-[P5] gave support for the writing of [P1] and [P3]. M.Sc. Sitbon and M.Sc. Kolesnik helped with the proofreading in [P1], [P3]-[P5].

[P1] Kivimäki, J., Sitbon M., Kolesnik S., Kuperman A. and Suntio T., "Design guidelines for multiloop perturbative maximum power point tracking algorithms", IEEE Trans. Power Electron., vol. 33, no. 2, pp. 1284-1293, Feb. 2018.

[P2] Kivimäki, J., Suntio T. and Kuperman A., "Factors affecting validity of PVG-power settling time estimation in designing MPP-tracking perturbation frequency", in *IECON 2017 - 43rd Annual Conference of the IEEE Industrial Electronics Society*, 2017, pp. 2485-2491.

[P3] Kivimäki, J., Sitbon M., Kolesnik S., Kuperman A. and Suntio T., "Revisited perturbation frequency design guideline for direct fixed-step maximum power point tracking algorithms", *IEEE Trans. Ind. Electron.*, vol. 64, no. 6, pp. 4601-4609, Jun. 2017.

[P4] Kivimäki, J., Sitbon M., Kolesnik S., Kuperman A. and Suntio T., "Sampling frequency design to optimizing MPP-tracking performance for open-loop-operated con-

verters", in *IECON 2016 - 42nd Annual Conference of the IEEE Industrial Electronics Society*, 2016, pp. 3093-3098.

[P5] Kivimäki, J., Sitbon M., Kolesnik S., Kuperman A. and Suntio T., "Determining maximum MPP-tracking sampling frequency for input-voltage-controlled PV-interfacing converter", in *2016 IEEE Energy Conversion Congress and Exposition (ECCE)*, 2016, pp. 1-8.

[P6] Kivimäki, J. and Suntio, T., "Appearance of a drift problem in variable-step perturbative MPPT algorithms", in *European Photovoltaic Solar Energy Conference and Exhibition (EU PVSEC)*, 2015, pp. 1602-1608.

1.7   Structure of the thesis

In addition to the introduction in Chapter 1, the thesis contains four chapters, which are summarized as follows: In Chapter 2, the modeling tools and methods for analyzing the behavior of PVG and dc-dc converters in PV applications are discussed. There, the small-signal models for PVG, dc-dc converter and their interconnected system are presented, and reduced-order models of the converters are derived in case of open-loop and closed-loop converters. Chapter 3 discusses the design process of the fixed-step perturbative algorithms focusing on the constraints of the perturbation frequency and step size. Based on the derived analysis in Chapter 2 and [P1]-[P6], the methods are provided to estimate the dynamic behavior of PVG power. The practical verification of the claimed issues with the actual prototypes is introduced in Chapter 4, including a description of the measurement system and the essential equipment used during the measurements. Finally, the conclusions are drawn in Chapter 5, summarizing the main claims. In addition, the issues for future research are discussed.

2 MODELING

Since the PVG current equation is non-linear, it cannot be studied similarly as linearized switched-mode converters by utilizing small-signal modeling techniques. However, the linear open-loop operation between perturbations allows the use of time-domain analysis, from which the dynamic characteristics can be derived allowing optimization of the design values of the P&O algorithm separately. Generally, the time-domain-based dynamic analysis is quite common in control engineering and are also utilized in conjunction with the grid-connected power electronics applications [68, 69]. However, the time-domain responses do not reveal the origin of the observed transient behavior or how close the system is for instability. Thus, the control design and stability analysis of PVG-interfacing dc-dc converter need to be still performed in the frequency domain to guarantee stable and controlled power processing as well as to predict the circuit response to changes in operating conditions.

This chapter presents the modeling methods used in the analysis of the PVG-interconnected dc-dc converters. The concept of state-space averaging is discussed with application to modeling switched-mode converters. The reduced-order models of the converter are discussed in detail by highlighting the fundamental factors affecting the transient response. These tools are further utilized in Chapter 3, where the optimal design parameters for MPPT algorithms are discussed in more detail.

2.1 Photovoltaic generator

Due to the highly nonlinear PVG characteristics and varying environmental conditions regarding irradiance and ambient temperature, dynamics of a solar energy conversion system must be properly identified for each possible operating point. In principle, a PV generator can be modeled either as a voltage or current source, since it contains both properties because of its dual nature, i.e., it can be modeled as a current or voltage source [69]. However, if a PV generator is modeled as a voltage source, the PV current (i.e., the input current of the interfacing converter) must be controlled, which can vary very fast due to the directly proportional dependency between irradiance and photo-induced current as shown in Fig. 1.4. Therefore, such an implementation would need a very high-bandwidth current controller of the interfacing converter in order to prevent saturation. Moreover, the further studies have revealed that the origin of the observed problem in PV
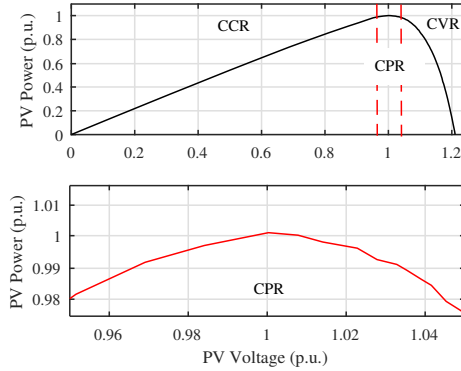
Fig. 2.1: Typical power-voltage characteristics of the PV module with extended view in the vicinity of the MPP.

current control is the violation of Kirchhoff's current law, which makes the converter to become unstable when the operating point is moved into the CCR [69, 70]. In contrast, PVG voltage is temperature dependent, which has very slow dynamics in respect of time. Thus, modeling a PVG as a current source is more preferred.

The current-voltage curve of a PV generator is typically divided into CCR and CVR separated by the MPP as can be seen in Fig. 2.1, which is plotted by utilizing existing data in the prior research by Leppäaho et al. Both regions are named based on the variable, which is staying practically constant and having the same dynamic behavior in the concerned area [71, 72]. On the contrary, following the same principle, the vicinity of the MPP can also be considered as a narrow constant-power region (CPR) rather than a single operating point due to the finite resolution of digitally controlled measurement and control system. Thus, a PVG-interfacing converter equipped with an MPPT algorithm can drift anywhere within in the narrow CPR. The existence of CPR can be further justified by examining the behavior of small-signal PV-generator power and ratio between dynamic and static resistances as discussed in this section.

(a) A detailed model.

(b) A Norton-equivalent model.

Fig. 2.2: A small-signal model of PV generator.

It is well known that the amount of current flowing through a silicon diode is reflected as diode dynamic resistance (r_{d}) and also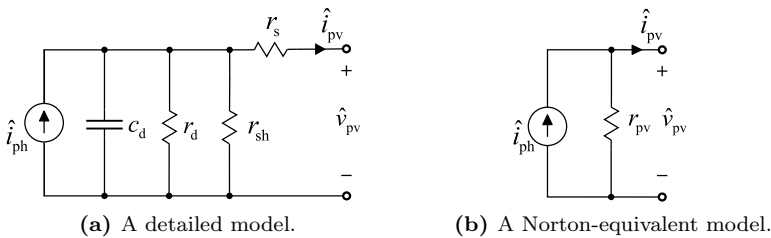 as dynamic capacitance (c_{d}), which is naturally dependent on the operating point of the cell. Thus, the diode in Fig. 1.1 can be replaced with respective components in parallel with r_{sh} as shown in Fig. 2.2a. Furthermore, the detailed equivalent circuit of PVG in Fig. 2.2a can be transformed into Norton-equivalent circuit with equivalent output resistance r_{pv} shown in Fig. 2.2b [72]. From the power electronics point of view, the behavior of dynamic (r_{pv}) and static resistance ($R_{\mathrm{pv}} = V_{\mathrm{pv}}/I_{\mathrm{pv}}$) have an essential role since the dynamic changes in the power electronic interfacing converter are affected by the ratio of dynamic and static resistances [72]. Thus, the low-frequency value of dynamic resistance r_{pv}, also known as small-signal or incremental resistance, can be given as

$$Z_{\mathrm{pv}} = r_{\mathrm{s}} + \frac{r_{\mathrm{sh}} \parallel r_{\mathrm{d}}}{1 + s(r_{\mathrm{sh}} \parallel r_{\mathrm{d}})c_{\mathrm{d}}} \overset{f \to 0}{\to} r_{\mathrm{pv}} = r_{\mathrm{s}} + \frac{r_{\mathrm{sh}} r_{\mathrm{d}}}{r_{\mathrm{sh}} + r_{\mathrm{d}}}, \tag{2.1}$$

where r_{d} represents the dynamic resistance of the diode. According to [10], the dynamic capacitance c_{d} of a single PV module can be in the order of a few microfarads and is the highest at the open circuit. Despite the fact that value of shunt capacitance can be significantly high in the CVR, it is usually much lower than an input capacitance of the interfacing converter, and therefore, it may be neglected in the most cases as also stated in [72]. However, it is worth noting that depending on a PV system the assumption might not be valid, and therefore, it should be verified case-by-case. Based on the prior impedance measurements in [73] with Raloss SR30-36 PV panel, which is also utilized in this thesis, values of PV parasitic capacitance is significantly lower compared to the input capacitor of the converter C_1 (cf. Tab. A.1) justifying the use of (2.1) in this thesis.

Based on the Fig. 2.1, it may be clear that $dp_{\mathrm{pv}}/dv_{\mathrm{pv}} = 0$ holds at the MPP. Therefore, we can conclude that

$$\left. \left(\frac{dp_{\mathrm{pv}}}{dv_{\mathrm{pv}}}\right) \right|_{\mathrm{MPP}} = \left. \left(\frac{dv_{\mathrm{pv}} i_{\mathrm{pv}}}{dv_{\mathrm{pv}}}\right) \right|_{\mathrm{MPP}} = V_{\mathrm{mpp}} \frac{di_{\mathrm{pv}}}{dv_{\mathrm{pv}}} + I_{\mathrm{mpp}} = 0 \Leftrightarrow -\frac{\Delta i_{\mathrm{pv}}}{\Delta v_{\mathrm{pv}}} = \frac{I_{\mathrm{pv}}}{V_{\mathrm{pv}}}. \tag{2.2}$$

Thus, the static resistance $R_{\mathrm{pv}} = V_{\mathrm{pv}}/I_{\mathrm{pv}}$ and $r_{\mathrm{pv}} = -\Delta v_{\mathrm{pv}}/\Delta i_{\mathrm{pv}}$ equal at MPP. The negative sign in front of the dynamic resistance in (2.2) originates from the fact that the dynamic resistance is defined by assuming positive current flowing into the terminal, although the actual current flows out of the terminal. Thus, the dynamic resistance as the output impedance of the PV cell can be determined similarly as the output impedance is defined in the state-space averaging approach discussed in the next section.

As concluded in the first chapter, the values of equivalent circuit components are both

environmental and operating point dependent, where r_{pv} represents the joint effect of these two. The same applies also to static resistance R_{pv} although it is computed based on the voltage and current of the operating point. Fig. 2.3 represents the measured dynamic and static resistances from Raloss SR30-36 PV generator recorded from the prior research in [73] also showing the extended view of them in the vicinity of MPP. A detailed description of the PV panel can be found at the beginning of Section 4.1, where the experimental setup of the research is discussed in more detail. The figure clearly indicates that, in the narrow CPR, dynamic and static resistances are very close to each other, thus indicating similar dynamic properties in the concerned region.
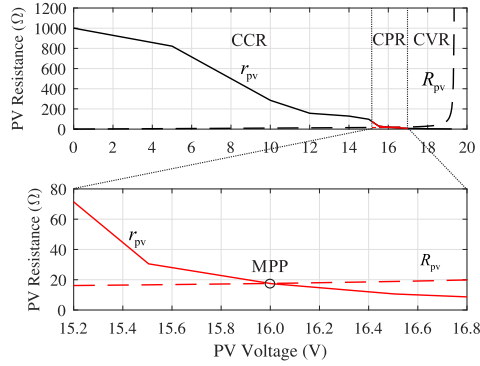
Fig. 2.3: Measured dynamic and static resistance characteristics in respect to PV voltage.

PVG power is of particular interest in MPPT-control design and therefore, its analytical model has to be correctly formed in order to predict the proper system operation and to optimize MPPT algorithm parameters. Generally, PVG power can be decomposed into DC and small-signal parts $p_{\mathrm{pv}} = P_{\mathrm{pv}} + \hat{p}_{\mathrm{pv}} = (V_{\mathrm{pv}} + \hat{v}_{\mathrm{pv}})(I_{\mathrm{pv}} + \hat{i}_{\mathrm{pv}})$ in which small-signal PVG power can be obtained as [57]

$$\hat{p}_{\mathrm{pv}} = V_{\mathrm{pv}}\hat{i}_{\mathrm{pv}} + I_{\mathrm{pv}}\hat{v}_{\mathrm{pv}} + \hat{v}_{\mathrm{pv}}\hat{i}_{\mathrm{pv}}. \tag{2.3}$$

As will be discussed in more detail in the following chapter, PVG voltage is the important control variable from the interfacing-converter point of view and therefore, small-signal power $\hat{p}_{\mathrm{pv}}$ can be represented as a function of voltage as follows

$$\hat{p}_{\mathrm{pv}} \approx V_{\mathrm{pv}}\left(\frac{1}{R_{\mathrm{pv}}} - \frac{1}{r_{\mathrm{pv}}}\right)\hat{v}_{\mathrm{pv}} - \frac{\hat{v}_{\mathrm{pv}}^2}{r_{\mathrm{pv}}}, \tag{2.4}$$

because $\hat{i}_{\mathrm{pv}} \approx -(1/r_{\mathrm{pv}})\hat{v}_{\mathrm{pv}}$ and static PV resistance equals $R_{\mathrm{pv}} = V_{\mathrm{pv}}/I_{\mathrm{pv}}$. Therefore,

the small-signal behavior of PVG power in different operation regions (CCR, CPR and CVR) can be given as follows

$$\hat{p}_{\mathrm{pv}} \approx I_{\mathrm{pv}}\hat{v}_{\mathrm{pv}}, \qquad \text{where } r_{\mathrm{pv}} \gg R_{\mathrm{pv}} \tag{2.5a}$$

$$\hat{p}_{\mathrm{pv}} \approx -(1/R_{\mathrm{pv}})\hat{v}_{\mathrm{pv}}^2, \qquad \text{where } R_{\mathrm{pv}} \approx r_{\mathrm{pv}} \tag{2.5b}$$

$$\hat{p}_{\mathrm{pv}} \approx -(V_{\mathrm{pv}}/r_{\mathrm{pv}})\hat{v}_{\mathrm{pv}} = V_{\mathrm{pv}}\hat{i}_{\mathrm{pv}}, \qquad \text{where } r_{\mathrm{pv}} \ll R_{\mathrm{pv}}, \tag{2.5c}$$

when assuming $\hat{v}_{\mathrm{pv}} \ll V_{\mathrm{pv}}$. Clearly, PV dynamic resistance changes the PVG-power characteristics significantly based on the operation region. Moreover, it is worth noting that the results in (2.5) are general, and therefore, they are not dependent on the interfacing dc-dc converter.

Figure 2.4 demonstrates the effect of sinusoidal PVG voltage perturbation on PVG power for Raloss SR30-36 PV panel. Power ripple behavior follows the formulations given above, i.e., the ripple is nearly constant and in phase with the PVG voltage ripple in CCR; the ripple increases with the increase in PVG voltage and is in opposite phase with the PVG voltage ripple in CVR; the ripple is close to zero in CPR. Fig. 2.4 also shows the similar ripple characteristics in the vicinity of the MPP, thus validating the existence of CPR. In fact, the described ripple characteristics are already utilized in ripple-based MPPT methods to identify the existence of MPP [44, 74] as mentioned in Section 1.4.1.
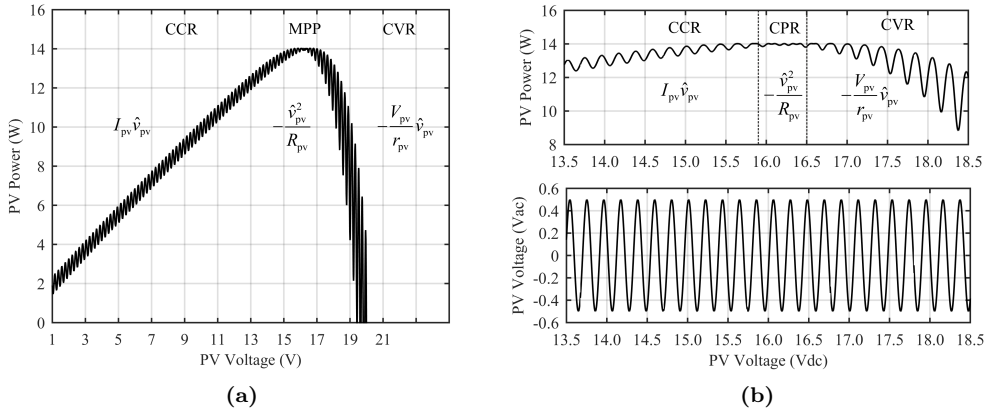

Fig. 2.4: Raloss SR30-36 PV panel voltage induced power ripple in different operation regions.

2.2 Dynamic modeling of dc-dc converters

A switched-mode dc-dc converter is an inherently nonlinear system due to the different sub-circuits introduced by the switching actions. In principle, that means that the system response cannot be calculated by combining system inputs separately, i.e., the principle of superposition does not apply. Therefore, in order to analyze the operation of a switched-mode converter in steady-state and dynamical conditions as well as to utilize linear mathematical tools such as *Laplace transform*, a linear model for the converter is required. In power electronics and control engineering in general, transfer functions are commonly used to characterize the input-output relationships of components or systems that can be described by linear, time-invariant, differential equations.

The usual way to model switched-mode converters is to use the state-space averaging approach introduced by Middlebrook in the 70's [75], which produce a linear time-invariant small-signal model describing behavior between defined inputs and outputs in frequency domain around the specific operating point. The basic idea behind the method is to average the behavior of the currents and voltages of the converter over a switching period and linearize the equations by using the first-order derivatives of the Taylor series around the steady-state operating point. Once the system behavior in the frequency domain is known, the circuit response can be predicted related to changes in operating conditions up to half the switching frequency.

2.2.1 State-space averaging

The linearized time-domain state-space model can be represented in (2.6), where $\hat{\mathbf{x}}(t)$, $\hat{\mathbf{u}}(t)$ and $\hat{\mathbf{y}}(t)$ are small-signal vectors containing the state variables, input variable and output variables, respectively. In general, switched-mode dc-dc converters have three input variables $\hat{\mathbf{u}} = [\hat{u}_1\,\hat{u}_2\,\hat{u}_c]^{\mathrm{T}}$ and two input-dependent output variables $\hat{\mathbf{y}} = [\hat{y}_1\,\hat{y}_2]^{\mathrm{T}}$. First two input variables are linked to input source and output load, whereas the third is the control variable. Output variables depict the electrical dual pairs of the input variables $\hat{u}_1$ and $\hat{u}_2$ yielding four different input-output variable combinations [76] as illustrated later in Fig. 2.5. Eventually, the state variables $\hat{\mathbf{x}}(t)$ are the smallest set of variables that determine the state of dynamic system. State variables can be chosen arbitrarily, however, the inductor currents and capacitor voltages are usually selected due to their memory characteristics.

$$
\begin{aligned}
\frac{\mathrm{d}\hat{\boldsymbol{x}}(t)}{\mathrm{d}t} &= \mathbf{A}\hat{\boldsymbol{x}}(t) + \mathbf{B}\hat{\boldsymbol{u}}(t) \\
\hat{\boldsymbol{y}}(t) &= \mathbf{C}\hat{\boldsymbol{x}}(t) + \mathbf{D}\hat{\boldsymbol{u}}(t),
\end{aligned}
\tag{2.6}
$$

where matrices $\mathbf{A}$, $\mathbf{B}$, $\mathbf{C}$ and $\mathbf{D}$ are coefficient matrices consisting of constant elements such as inductances, capacitances and resistances. The time-domain state space in (2.6) can be solved in the frequency domain by applying Laplace transform with zero initial conditions, which yields (2.7).

$$
\begin{aligned}
s\boldsymbol{X}(s) &= \mathbf{A}\boldsymbol{X}(s) + \mathbf{B}\boldsymbol{U}(s) \\
\boldsymbol{Y}(s) &= \mathbf{C}\boldsymbol{X}(s) + \mathbf{D}\boldsymbol{U}(s)
\end{aligned}
\tag{2.7}
$$

Solving the relation between input and output variables from (2.7) yields

$$
\boldsymbol{Y}(s) = (\mathbf{C}(s\mathbf{I} - \mathbf{A})^{-1}\mathbf{B} + \mathbf{D})\boldsymbol{U}(s) = \mathbf{G}(s)\boldsymbol{U}(s),
\tag{2.8}
$$

Matrix $\mathbf{G}$ in (2.8) contains six transfer functions, describing the mapping between input variables ($\boldsymbol{U} = [\hat{u}_1\ \hat{u}_2\ \hat{u}_c]^\mathrm{T}$) and output variables ($\boldsymbol{Y} = [\hat{y}_1\ \hat{y}_2]^\mathrm{T}$) Furthermore, Equation (2.8) describes how to calculate the transfer functions when linearized state-space matrices are solved. Using matrix notation, the mapping can be expressed as follows

$$
\begin{bmatrix} \hat{y}_1 \\ \hat{y}_2 \end{bmatrix} = \begin{bmatrix} G_{11} & T_{\mathrm{oi}} & G_{\mathrm{ci}} \\ G_{\mathrm{io}} & -G_{22} & G_{\mathrm{co}} \end{bmatrix} \begin{bmatrix} \hat{u}_1 \\ \hat{u}_2 \\ \hat{u}_c \end{bmatrix}
\tag{2.9}
$$

The transfer functions G_{11} and G_{22} in (2.9) describe the ohmic characteristics of input and output terminals, respectively. The minus sign in the transfer function G_{22} is required since the current flowing out of the converter is defined positive. The reverse transfer function T_{oi} describes the effect caused by the output terminal variable $\hat{u}_2$ on the input terminal variable $\hat{y}_1$. Respectively, the control-to-input transfer function G_{ci} determines the interaction between the control variable $\hat{u}_c$ and $\hat{y}_1$, whereas G_{co} is the interaction of $\hat{u}_c$ to on the output terminal variable $\hat{y}_2$. Finally, the forward transfer-function G_{io} describes the effect caused by the $\hat{u}_1$ to $\hat{y}_2$.

Traditionally, a vast majority of switched-mode converters have had a constant voltage as the input source, such as the utility grid, a battery or a dc link and have had their output voltage controlled by means of the feedback loop. In contrast, most of the power electronic converters applied in interfacing the renewable energy sources into the power grid in grid-feeding mode are to be considered as current-fed converters due to the feedback control of their input-terminal voltage. Therefore, it is important to recognize the applicable conversion scheme to correctly selecting the input and output variables.

Correct analysis of switched-mode dc-dc converter requires that the applicable con-

version scheme must be first selected, i.e., determining the input and output variables $\hat{u}_1$, $\hat{u}_2$, $\hat{y}_1$, $\hat{y}_2$ based on desired application. Input variables $\hat{u}_1$, $\hat{u}_2$ are defined and controlled externally and therefore, they cannot be selected as controllable output variables. Therefore, there are four eligible conversion schemes [76] called network parameters G, Y, H and Z, which are suitable for analyzing dynamic characteristics of interfacing power converters. These four conversion schemes with the corresponding input and output variables are represented in Fig. 2.5. Most of the existing applications belong G-parameter scheme, where the converter is fed from a constant voltage source, and the output voltage is regulated by the converter. The Y-parameter scheme is fed from constant voltage source controls while its output current is regulated, which is suitable for controlled Light emitting diode (LED) applications, for instance. H-parameters scheme, which is also utilized in this thesis, is used in PV applications, where PV-generator voltage needs to be controlled while its output voltage remains constant (e.g., dc-link of an inverter). Eventually, Z-parameters scheme shares the same input terminal properties than H-parameter scheme but regulates its output voltage instead of current. Such a scheme can be used in grid-feeding PV systems [77], for instance.
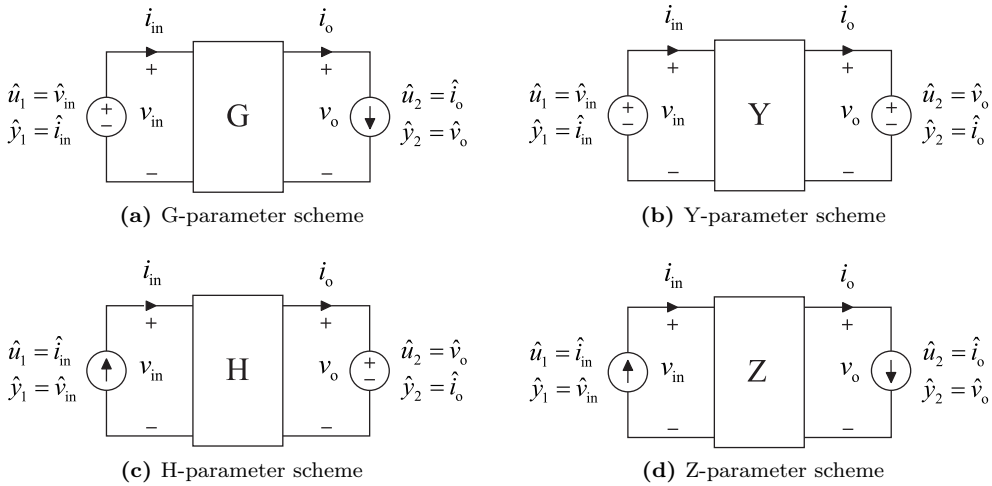
Fig. 2.5: Four conversion schemes suitable for analyzing dynamic characteristics of interfacing power converters.

This thesis focuses on modeling a single MPP-tracked voltage boosting dc-dc converter either in standalone or two-stage PV applications, thus, H-parameter scheme is utilized in the subsequent analysis. However, it is worth noting that the later discussed analyzes can also be derived for other conversion schemes as well. Thus, in H-parameter scheme, the transfer function matrix $\mathbf{G}(s)$ and the corresponding input $\mathbf{U} = [\hat{i}_{\mathrm{in}} \; \hat{v}_{\mathrm{o}} \; \hat{c}]^{\mathrm{T}}$ and output $\mathbf{Y} = [\hat{v}_{\mathrm{in}} \; \hat{i}_{\mathrm{o}}]^{\mathrm{T}}$ variables can be represented in matrix notation as shown in (2.10). It is

worth noting that the given notation is valid for both open-loop and closed-loop systems.

$$
\begin{bmatrix} \hat{v}_{\mathrm{in}} \\ \hat{i}_{\mathrm{o}} \end{bmatrix} = \begin{bmatrix} Z_{\mathrm{in}} & T_{\mathrm{oi}} & G_{\mathrm{ci}} \\ G_{\mathrm{io}} & -Y_{\mathrm{o}} & G_{\mathrm{co}} \end{bmatrix} \begin{bmatrix} \hat{i}_{\mathrm{in}} \\ \hat{v}_{\mathrm{o}} \\ \hat{c} \end{bmatrix}.
\tag{2.10}
$$

As a graphical representation, the transfer function set in (2.10) can be equally represented by a linear two-port model as shown inside the dotted line in Fig. 2.6. The input port is modeled as a series connection of two dependent voltage sources and input impedance, whereas the output port is modeled as a parallel connection of two dependent current sources and an output admittance.
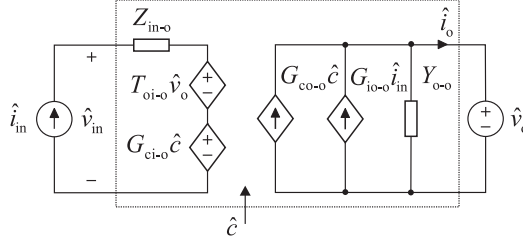

Fig. 2.6: A linear two-port model of current-fed-current-output converter with an ideal source.

When the converter is fed by a current source, the internal mode of operation is classified based on the behavior of capacitor voltage similarly as in case of the voltage-fed converters based on the behavior of inductor current. The operation mode is continuous if the corresponding state variable has two different derivatives, and the operation is discontinuous if the corresponding state variable will stay at zero level during a part of the cycle [69]. In renewable power electronic applications, continuous-conduction-mode is the preferred solution, because circuit theory can be easily applied for computing the required derivatives of the state variables and the formulations for the output variables [69].

2.2.2 Transient characteristics of first-order and second-order systems

A transfer function is usually given as a ratio of two polynomials as a function of the Laplace variable s as shown in (2.11). A transfer function can be factored by finding the roots of the numerator and denominator polynomials, called zeros ω_{z} and poles ω_{p}, yielding the final form in (2.11). The zeros and poles may be real or complex numbers, and they are given in respect of angular frequency ω (rad/s).

$$G(s) = \frac{a_n s^n + a_{n-1} s^{n-1} + \cdots + a_0}{b_m s^m + b_{m-1} s^{m-1} + \cdots + b_0}$$
$$= K \cdot \frac{(s + \omega_{z1})(s + \omega_{z2}) \cdots (s + \omega_{zn})}{(s + \omega_{p1})(s + \omega_{p2}) \cdots (s + \omega_{pm})}, \quad (m \geq n), \tag{2.11}$$

The second-order polynomials are common in power electronics [69], and they shall be recognized because of their distinct influence on the control design as well as the source and load-impedance effects on the dynamic behavior of the converter. Thus, the standard form of the second-order system, which describes the relation between output variable $\hat{y}(s)$ and control variable $\hat{c}(s)$, can be given as follows

$$G(s) = \frac{\hat{y}(s)}{\hat{c}(s)} = \frac{\omega_n^2}{s^2 + 2\zeta\omega_n s + \omega_n^2} = \frac{\omega_n^2}{(s + \zeta\omega_n + j\omega_d)(s + \zeta\omega_n - j\omega_d)}. \tag{2.12}$$

In this way, the dynamic behavior of the second-order system can then be described in terms of two distinct parameters – natural frequency ω_n and damping factor ζ, where the damped natural frequency is dependent on these two variables as $\omega_d = \omega_n\sqrt{1 - \zeta^2}$. Based on the value of damping factor, a stable system can be categorized in three different cases: *underdamped*, when $0 < \zeta < 1$, *critically damped*, when $\zeta = 1$, *overdamped*, when $\zeta > 1$.

If $0 < \zeta < 1$, the closed-loop poles are complex conjugates lying on the left half of the s plane, i.e., the roots of the second-order polynomial can be expressed as $s_{1,2} = -\zeta\omega_n \pm \omega_n\sqrt{\zeta^2 - 1}$. For a illustration, these poles are plotted on s-plane shown in Fig. 2.7a. As shown in the figure, the poles have the same radius from the origin (i.e., ω_n), and the angle from the real axis (i.e., $\theta = \tan^{-1}(\sqrt{1 - \zeta^2}/\zeta)$).

An unit-step input, where the input value is increased from zero to one in stepwise action, is commonly utilized in control engineering and power electronics. For the unit-step input ($\hat{c} = 1/s$) applied to (2.12), the corresponding time-domain function for $\hat{y}(s)$ can be solved by using inverse *Laplace transformation* (i.e., $\hat{y}(t) = \mathcal{L}^{-1}\{\hat{y}(s)\}$) as follows

$$\hat{y}(t) = \mathcal{L}^{-1}\left\{\frac{G(s)}{s}\right\} = 1 - \frac{\exp(-\zeta\omega_n t)}{\sqrt{1 - \zeta^2}} \sin\left(\omega_d t + \tan^{-1}\frac{\sqrt{1 - \zeta^2}}{\zeta}\right). \tag{2.13}$$

As can be concluded from (2.13), the output variable exhibits decaying sinusoidal oscillation at the damped natural frequency ω_d when a step change in the input variable is applied. The correlation between the damping factor and time-domain behavior is further illustrated in Fig. 2.7b, where unit-step response curves $\hat{y}(t)$ with varying damping

is shown. From (2.13) we can calculate that the maximum overshoot in respect to the unity steady-state value is $\exp(-\zeta\pi/\sqrt{1-\zeta^2})$, which will occur at $t = \pi/\omega_{\mathrm{d}}$. Thus, two second-order systems having the same ζ but different ω_{n} will exhibit the same overshoot and the same oscillatory behavior.

While the roots of the transfer functions move closer to the imaginary axis, ζ approaches zero. In a zero condition, the transfer function has pure imaginary roots located at $s_{1,2} = \pm j\omega_{\mathrm{n}}$ yielding non-decaying sinusoidal oscillation at ω_{n}. Basically, if no saturation takes place in the system, the magnitude of the oscillation can be either infinitely low or high.

(a) Second-order parameters on s plane

(b) Three-dimensional plot of unit-step response curves
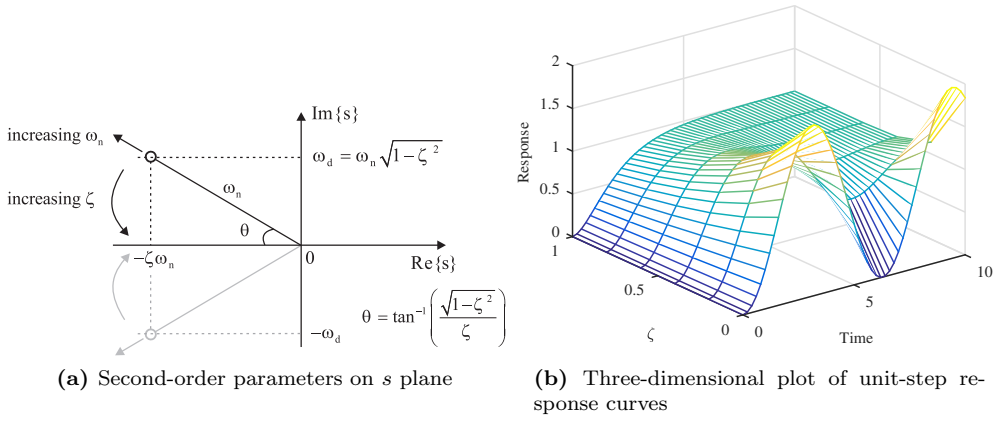
Fig. 2.7: Characteristics of second-order system parameters.

If the two poles are located on the real axis, the $\zeta \geq 1$ and depending on the value of ζ the system is called either critically ($s_{1,2} = -\zeta\omega_{\mathrm{n}}$) or overdamped ($s_{1,2} = -\zeta\omega_{\mathrm{n}} \pm \omega_{\mathrm{n}}\sqrt{\zeta^2 - 1}$). In both cases, the step response contains only exponential time-domain behavior, in which the speed is dependent on location of the pole in the real axis. For a unit-step input for critically damped system, the corresponding time-domain response can be found as

$$\hat{y}(t) = 1 - \exp(-\omega_{\mathrm{n}}t)(1 + \omega_{\mathrm{n}}t), \tag{2.14}$$

and in case of overdamped system

$$\hat{y}(t) = 1 + \frac{\omega_{\mathrm{n}}}{2\sqrt{1-\zeta^2}} \left(\frac{\exp(-s_1 t)}{s_1} - \frac{\exp(-s_2 t)}{s_2} \right). \tag{2.15}$$

35

When ζ is much larger than unity, one of the poles is located close to the origin and the other pole close to infinity, respectively. Thus, one of the two decaying components decreases much faster compared to the other and the faster-decaying exponent term can be neglected. Therefore, the system response reduces to the system with a first-order response. For example, if s_1 is located much closer to the origin than $-s_2$, the system time response can be approximated by

$$\hat{y}(t) = 1 - \exp\left((-\zeta + \sqrt{\zeta^2 - 1})\omega_n t\right). \tag{2.16}$$

The systems that inherently have high-order dynamics, containing three or more poles as in (2.11), consist of sum of responses of the first and the second-order terms [78]. If the poles of $G(s)$ consist of pairs of complex-conjugate poles, its factored form is consisting of first and second-order terms. In case of all poles are distinct, Equation (2.11) can be rewritten as

$$Y(s) = \frac{G(s)}{s} = \frac{a}{s} + \sum_{k=1}^{r} \frac{b_k(s + \zeta_k \omega_{n,k}) + c_k \omega_{n,k}\sqrt{1 - \zeta_k^2}}{s^2 + 2\zeta_k \omega_{n,k}s + \omega_{n,k}^2}, \tag{2.17}$$

which will eventually yield a sum of under-damped second-order step responses in (2.13). Typically, the dynamics of a high-order power electronic converter consists of multiple second-order transfer functions with different damping factors. Thus, the initial transient behavior of a system can be characterized by the dominant pole pairs, which locate closest to the origin as discussed more in detail in the next section.

2.2.3 Dynamic modeling under feedback control

In addition to formerly discussed open-loop systems, the negative-feedback control is commonly utilized to maintain the desired variable constant at the predefined value. This is done by forming a feedback-control loop by measuring error between the output variable and reference value, which is further fed to the controller. An advantage of the closed-loop control system is the fact that the use of feedback makes the system response relatively insensitive to external disturbances and internal variations in system parameters. Thus, manipulating the open-loop transfer function with the feedback loop, the poles or zeros of the original transfer function can be effectively revised to achieve the desired time-domain and filtering properties.

According to control engineering principles [78], only one of the output variables ($\hat{y}_1$ or $\hat{y}_2$ in (2.9)) may be controlled with a single control variable $\hat{u}_c$. In case of a PVG-interfaced dc-dc converter, the H-parameter scheme is the most preferred option indicat-

ing that the controllable output variable can be either the input voltage $\hat{v}_{\text{in}}$ or output current $\hat{i}_{\text{o}}$. Some earlier studies utilized the Y-parameter scheme for control design, thus the corresponding control variables can be either input current $\hat{i}_{\text{in}}$ or output current $\hat{i}_{\text{o}}$. However, the problem with the input-current control in photovoltaic applications is the fact that a sudden change in the output current of the PVG due to irradiance change (cf., Section 1.2) can saturate the controller causing the operating point to deviate away from the MPP with reduced energy yield. Moreover, it is further shown in [73] that PVG-terminal voltage is the only viable control variable in photovoltaic applications.

To analyze the operation of a feedback-controlled converter, the corresponding closed-loop transfer function can be solved from the block diagram shown in Fig. 2.8 one at a time by neglecting the other variables except the ones being studied. Thus, the input-output transfer functions can be solved and are given in matrix form in (2.18). It is worth noting that $G_{\text{ci-o}}$ has inherently negative dc gain as a consequence of operating the power-stage switches similarly as in the corresponding voltage-fed converter. Therefore, in order to increase the PV voltage, the conduction time of the switch needs to be reduced. To restore the positive gain, the gate drive signal can be inverted. Here, the inversion is performed by using negative gain in front of the control transfer function G_{c}.
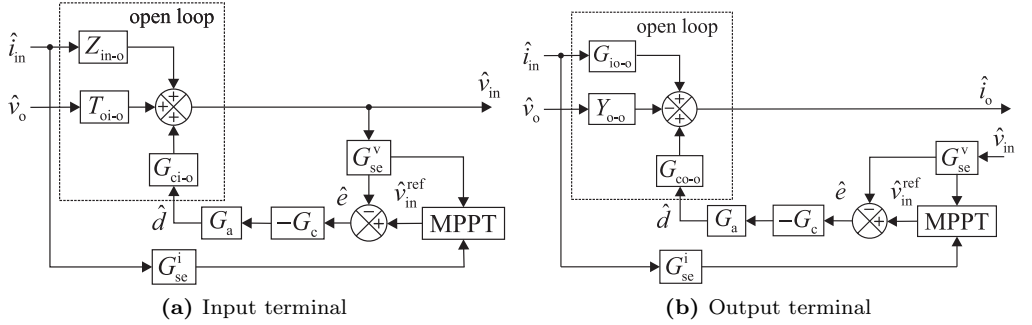

Fig. 2.8: Block diagram for voltage-boost dc-dc converter scheme under input-voltage control with MPPT.

$$
\begin{bmatrix} \hat{v}_{\text{in}} \\ \hat{i}_{\text{o}} \end{bmatrix} = \begin{bmatrix} Z_{\text{in-c}} & T_{\text{oi-c}} & G_{\text{ci-c}} \\ G_{\text{io-c}} & -Y_{\text{o-c}} & G_{\text{co-c}} \end{bmatrix} \begin{bmatrix} \hat{i}_{\text{in}} \\ \hat{v}_{\text{o}} \\ \hat{v}_{\text{in}}^{\text{ref}} \end{bmatrix}
$$

$$
= \begin{bmatrix} \dfrac{Z_{\text{in-o}}}{1 + L_{\text{in}}} & \dfrac{T_{\text{oi-o}}}{1 + L_{\text{in}}} & \dfrac{1}{G_{\text{se}}^{\text{v}}} \dfrac{L_{\text{in}}}{1 + L_{\text{in}}} \\[3mm] \dfrac{G_{\text{io-o}} + G_{\text{io-}\infty} L_{\text{in}}}{1 + L_{\text{in}}} & -\dfrac{Y_{\text{o-o}} + L_{\text{in}} Y_{\text{o-}\infty}}{1 + L_{\text{in}}} & \dfrac{1}{G_{\text{se}}^{\text{v}}} \dfrac{G_{\text{co-o}}}{G_{\text{ci-o}}} \dfrac{L_{\text{in}}}{1 + L_{\text{in}}} \end{bmatrix} \begin{bmatrix} \hat{i}_{\text{in}} \\ \hat{v}_{\text{o}} \\ \hat{v}_{\text{in}}^{\text{ref}} \end{bmatrix},
$$

(2.18)

37

where

$$\begin{aligned}
\text{L}_{\text{in}} &= -G_{\text{se}}^{\text{v}} G_{\text{c}} G_{\text{a}} G_{\text{ci-o}}, \\
G_{\text{io-}\infty} &= G_{\text{io-o}} - \frac{Z_{\text{in-o}} G_{\text{co-o}}}{G_{\text{ci-o}}}, \quad Y_{\text{o-}\infty} = Y_{\text{o-o}} + \frac{T_{\text{oi-o}} G_{\text{co-o}}}{G_{\text{ci-o}}}.
\end{aligned} \tag{2.19}$$

In Equation (2.19), L_{in} is called the input-voltage loop gain, G_{se}^{v} is the input-voltage sensing gain, G_{c} is the input-voltage controller transfer function, G_{a} is the modulator gain, $G_{\text{io-}\infty}$ is ideal forward current gain and $Y_{\text{o-}\infty}$ is the ideal output admittance, respectively. The interest of using the ideal transfer functions is that they consist only of the open-loop transfer functions, i.e., they are not affected by the control loop. The special transfer functions $G_{\text{io-}\infty}$ and $Y_{\text{o-}\infty}$ can be seen from $G_{\text{io-c}}$ and $Y_{\text{o-c}}$ in (2.18) by examining the magnitude of the loop gain L_{in}. Typically, the control loop is designed to have a high gain at low frequencies to eliminate the steady-state error. This can be achieved by using a controller with integrator resulting theoretically infinite gain at low frequencies. The high loop gain at low frequencies yields that closed-loop transfer functions $G_{\text{io-c}}$ and $Y_{\text{o-c}}$ equals ideal transfer functions $G_{\text{io-}\infty}$ and $Y_{\text{o-}\infty}$. In contrast, at high frequencies the loop gain is low and therefore, closed-loop transfer functions $Z_{\text{in-c}}, T_{\text{oi-c}}, G_{\text{io-c}}$ and $Y_{\text{o-c}}$ approach their corresponding open-loop transfer functions.

Two classical ways exist for the feedback-loop design, when the system dynamics is as given in (2.12) depending on the desired performance of a system: In the case, where the desired loop-gain crossover frequency ω_{c} is much lower than the crossover frequency of the open-loop transfer function. Thus, there is no need to cancel the capacitor ESR induced zero. Therefore, the following integral (I) controller can be utilized

$$G_{\text{c}}^{\text{I}} = \frac{K_{\text{c}}}{s}, \tag{2.20}$$

where K_{c} denotes the gain of the controller. If the converter is of resonant nature in open loop, then it is important to place the feedback-loop crossover frequency in such a manner that proper gain and phase margins are obtained for ensuring robust stability and performance.

In contrast, in case the desired loop-gain crossover frequency ω_{c} is close to or higher than the open-loop crossover frequency, the proportional-derivative-integral (PID) controller with an additional pole (cf. (2.21)) is typically used to achieve the required gain

and phase margins.

$$G_{\mathrm{c}}^{\mathrm{PID}} = \frac{K_{\mathrm{c}}(1 + s/\omega_{\mathrm{z1}})(1 + s/\omega_{\mathrm{z2}})}{s(1 + s/\omega_{\mathrm{p1}})(1 + s/\omega_{\mathrm{p2}})}. \tag{2.21}$$

The zeros of the controller $(\omega_{\mathrm{z1}}, \omega_{\mathrm{z2}})$ are typically placed at the resonant frequency to give phase boost at that frequency, while poles $(\omega_{\mathrm{p1}}, \omega_{\mathrm{p2}})$ are designed to cancel the effect of ESR zero and attenuate high-frequency noise from the switching actions.

For the stable system, the roots of the characteristic polynomial $1 + L_{\mathrm{in}}(s)$ must be located in the open left-half plane of the complex plane. The study of the location of the roots of the characteristic polynomial can be made by observing the frequency response of the loop gain. In practice, this can be done with polar and Bode plots, which are constructed by plotting the magnitude $|G(j\omega)|$ in decibels (dB) and the phase $\angle G(j\omega)$ in degrees with respect to logarithmic frequency scale. The robustness of the stability is typically related to gain (GM) and phase (PM) margins, which are related to the Bode's stability conditions. The gain margin is defined as $-(1/L_{\mathrm{in}})$ dB at the frequency, where $\angle L_{\mathrm{in}}(s) = 180°$ and the phase margin is $\angle L_{\mathrm{in}}(s) + 180°$ at the frequency where $|L_{\mathrm{in}}(s)| = 1$. For minimum requirements for stability, the gain margin of 6 dB and the phase margin of 30° are typically considered.

The control design can be performed fully in continuous time based on the frequency-domain transfer functions despite the fact that the control system is implemented in analogically or digitally. A discrete implementation of the control system, however, introduce a delay in a control loop, which needs to be taken into account in control design. Thus, the feedback loop gain will be affected by the sampling delay T_{d}, which is usually considered to be in the order of $1.5T_{\mathrm{sw}}$, where T_{sw} denotes the switching cycle. In Laplace domain, the delay equals $e^{-T_{\mathrm{d}}s}$, which can taken into account in transfer functions by using *Padé approximation* [79]. For example, the first order approximation can be given by

$$e^{-T_{\mathrm{d}}s} \approx \frac{1 - (T_{\mathrm{d}}/2)s}{1 + (T_{\mathrm{d}}/2)s}. \tag{2.22}$$

The delay produces a phase shift, which would be already close to -45 degrees at 1/10 of the switching frequency posing real problems for control design when the goal is to place the crossover frequency at the corresponding frequencies. In practice, this means that the resonant frequency should be designed to be at lower frequencies so that the crossover frequency would be selected close to 10-times of the resonant frequency to reduce more the dependence on the PV generator.

As concluded previously, the mathematical relationship between the step transient

response and the frequency response can be easily solved for standard second-order systems. For the non-standard or high-order systems, however, that correlation may not be easily predicted due to the fact that the additional poles and zeros are causing cross-couplings between the time-domain components. Some mathematical techniques can be utilized, but they appear to be too burdensome for practical use [78].

Figure 2.9 shows typical closed-loop control-to-input-voltage transfer functions in case of I and PID-controlled feedback systems, where the crossover frequency is designed to be lower and higher than the resonant frequency of the open-loop converter. According to the figures, the corresponding closed-loop transfer functions have either first-order (2.9a) or second-order (2.9b) characteristic, respectively. Although the accurate representation contains several poles in the transfer function, the initial closed-loop dynamic behavior can be characterized by the dominant pole pairs of the transfer function, i.e., the system poles located closest to the origin [78]. Therefore, the input-voltage loop gains have to be basically either first-order or second-order transfer functions, where the behavior of the transfer functions in the vicinity of the loop crossover frequency will determine the dynamic behavior of the closed-loop system. In the following, the reduced-order models are introduced in order to estimate the behavior of the converters.
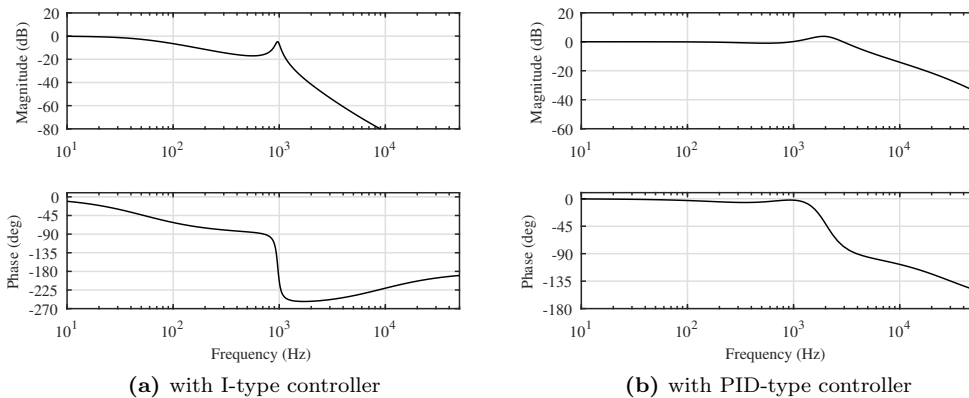

(a) with I-type controller

(b) with PID-type controller

Fig. 2.9: Typical frequency responses of closed-loop control-to-input-voltage transfer functions of CF-CO dc-dc converter.

Reduced-order models: intuitive method

In case the dc-dc converter operates under I-type control, the full-order loop gain can be given as (2.23) based on (2.12), (2.19) and (2.20).

$$L_{\text{in}}^{\text{I}} = \frac{G_{\text{se}}^{\text{v}} G_{\text{a}} K_{\text{c}} V_{\text{e}}}{s} \cdot \frac{\omega_{\text{n}}^2 (1 + s/\omega_{\text{z-esr}})}{s^2 + 2\zeta\omega_{\text{n}}s + \omega_{\text{n}}^2}. \tag{2.23}$$

where V_{e} represents the steady-state gain of the open-loop transfer function $G_{\text{ci-o}}$. If the roots of the denominator polynomial are well separated, ζ is considerably higher than unity, and the poles of the system are well separated and lie completely on the real axis in s plane. Thus, the input-voltage loop gain determining the low-frequency behavior related to the resonant frequency can be approximated in case of I-type control by [80]

$$L_{\text{in}}^{\text{I-RO}} = \frac{G_{\text{se}}^{\text{v}} G_{\text{a}} K_{\text{c}} V_{\text{e}}}{s} \qquad (0 < \omega < \omega_{\text{c}}), \tag{2.24}$$

within the control bandwidth. According to (2.18), the reduced-order closed-loop control-to-input-voltage transfer function $G_{\text{ci-c}}^{\text{I-RO}}$ can be given for I controlled system by (2.25). Thus, the system can be characterized by first-order transfer function with the single pole located at $s = -G_{\text{se}}^{\text{v}} G_{\text{a}} K_{\text{c}} V_{\text{e}}$.

$$G_{\text{ci-c}}^{\text{I-RO}} = \frac{1}{G_{\text{se}}^{\text{v}}} \frac{\dfrac{G_{\text{se}}^{\text{v}} G_{\text{a}} K_{\text{c}} V_{\text{e}}}{s}}{1 + \dfrac{G_{\text{se}}^{\text{v}} G_{\text{a}} K_{\text{c}} V_{\text{e}}}{s}} = \frac{G_{\text{a}} K_{\text{c}} V_{\text{e}}}{s + G_{\text{se}}^{\text{v}} G_{\text{a}} K_{\text{c}} V_{\text{e}}}. \tag{2.25}$$

Figure 2.10a shows the estimated frequency responses of the input-voltage loop gain (red dashed line) vs. the corresponding full-scale (solid black line) frequency responses under the I-type control. The gain K_{c} for I-controller is such that 50 Hz crossover frequency and 10 dB GM are achieved. The figure indicates that the reduced-order method equals well the original full-order response in the vicinity of the input-voltage-loop crossover frequency (i.e., $\omega_{\text{c}} = 2\pi \cdot 50$ rad/s and phase margin (PM) is 89.8 degrees). Moreover, a Bode diagram of the complementary sensitivity function is shown in Fig. 2.10 and is well predicted by (2.25) within the control bandwidth, as expected.

As can be concluded from (2.25), by estimating the fundamental behavior of loop gain with a low-frequency behavior yields very intuitive approximation. However, in that case, the internal behavior of the converter needs to be known, i.e., the values of the gains cannot be directly extracted from the Bode plot. The approximation can be also performed based on the control-engineering methods further discussed in the next
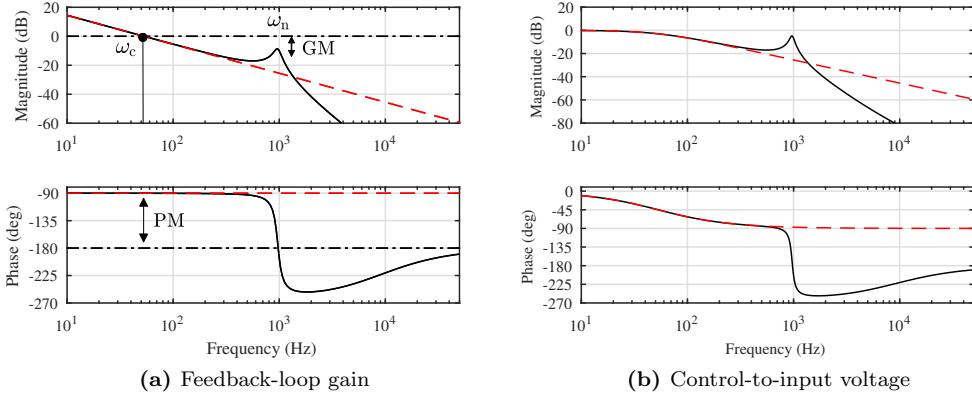
(a) Feedback-loop gain

(b) Control-to-input voltage

Fig. 2.10: The reduced-order frequency response (dotted line) vs the full-order frequency response of the input-voltage loop gains

section. In general, since the roots of the denominator polynomial are well separated, then the control-to-input voltage transfer function can be approximated by

$$G_{\text{ci-c}}^{\text{I-RO}} = \frac{\omega_{\text{n-c}}/2\zeta_c}{s + \omega_{\text{n-c}}/2\zeta_c}, \tag{2.26}$$

where $\omega_{\text{n-c}}$ and ζ_c denotes the undamped natural frequency and the damping factor for the closed-loop system. These parameters can be extracted from the measured Bode plot and can be given as a function of crossover frequency and damping factor of the system similarly as in case of the reduced second-order model discussed in the following section.

Reduced Order models: control-engineering-based method

In case of the desired loop gain crossover frequency ω_c is close to or higher than the resonant frequency, PID-type controller in (2.21) is typically used and therefore, the full-order input-voltage loop gain is then given by

$$L_{\text{in}}^{\text{PID}} = \frac{K_c G_{\text{se}}^{\text{v}} G_a (1 + s/\omega_{z1})(1 + s/\omega_{z2})}{s(1 + s/\omega_{p1})(1 + s/\omega_{p2})} \cdot \frac{\omega_{\text{n-c}}^2 (1 + s/\omega_{\text{z-esr}})}{s^2 + 2\zeta_c \omega_{\text{n-c}} s + \omega_{\text{n-c}}^2} \cdot \exp(-T_d s) \tag{2.27}$$

taking into account delay T_d caused by the sampling and the PWM modulator. The complementary sensitivity function related to the PVG voltage loop gain is then obtained as a fourth-order unity-DC-gain system with the relative degree of two, and it may be

approximated within the control bandwidth by a dominant pole pair as

$$G_{\text{ci-c}}^{\text{PID-RO}} = \frac{1}{G_{\text{se}}^{\text{v}}} \frac{L_{\text{in}}^{\text{PID-RO}}}{1 + L_{\text{in}}^{\text{PID-RO}}} = \frac{\omega_{\text{n-c}}^2}{s^2 + 2\zeta_{\text{c}}\omega_{\text{n-c}}s + \omega_{\text{n-c}}^2} \qquad 0 < \omega < \omega_{\text{c}}, \tag{2.28}$$

where $L_{\text{in}}^{\text{PID-RO}}$ corresponds the reduced-order version of the $L_{\text{in}}^{\text{PID}}$. Several methods exist for such a model reduction. Here, the classical control-engineering-related approach is used by modifying (2.28) to corresponding unity-feedback system as illustrated in Fig. 2.11.
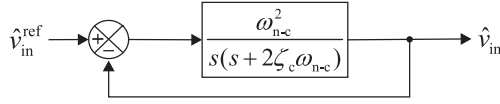

Fig. 2.11: A closed-loop block diagram for an approximated second-order system.

Thus, the corresponding loop gain of the reduced-order system can be separated from the original transfer function and is given as follows

$$L_{\text{in}}^{\text{PID-RO}} = \frac{\omega_{\text{n-c}}^2}{s(s + 2\zeta_{\text{c}}\omega_{\text{n-c}})} \qquad 0 < \omega < \omega_{\text{c}}, \tag{2.29}$$

from which the crossover frequency ω_{c} and phase margin PM can be solved by setting the magnitude to unity (i.e., $|L_{\text{in}}| = 1$), and solving the corresponding frequency and phase. The corresponding PM $= 180^\circ + \angle L_{\text{in}}(\omega_{\text{c}})$. According to theses procedures, ω_{c} and PM can be given by [78]

$$\omega_{\text{c}} = \omega_{\text{n-c}}\sqrt{\sqrt{1 + 4\zeta_{\text{c}}^4} - 2\zeta_{\text{c}}^2} \tag{2.30a}$$

$$\text{PM} = \tan^{-1}\left(\frac{2\zeta_{\text{c}}}{\sqrt{\sqrt{1 + 4\zeta_{\text{c}}^4} - 2\zeta_{\text{c}}^2}}\right). \tag{2.30b}$$

Based on (2.28), $\omega_{\text{n-c}}$ and ζ_{c} need to be solved in order to formulate the corresponding

reduced-order transfer function, which can be solved from (2.30) yielding

$$\omega_{\text{n-c}} = \frac{\omega_{\text{c}}}{\sqrt{\sqrt{1 + 4\zeta_{\text{c}}^4} - 2\zeta_{\text{c}}^2}} \tag{2.31a}$$

$$\zeta_{\text{c}} = \frac{\tan(\text{PM})}{2\big(1 + \tan^2(\text{PM})\big)^{\frac{1}{4}}}. \tag{2.31b}$$

It worth noting that while the natural frequency $\omega_{\text{n-c}}$ of the closed-loop system is dependent on both damping factor and crossover frequency, the damping factor can be solely approximated by PM. Thus, the dynamic characteristics of the closed-loop system can be tuned by selecting the crossover frequency and the phase margin correspondingly.
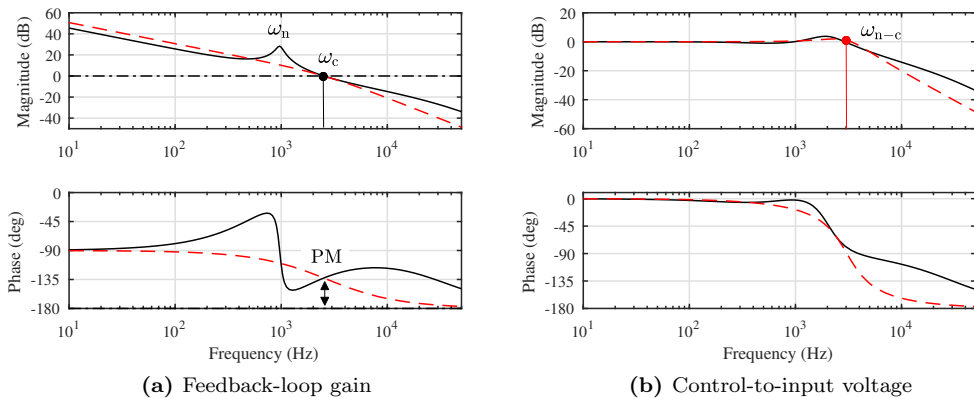

(a) Feedback-loop gain **(b)** Control-to-input voltage

Fig. 2.12: The reduced-order frequency response (red dashed line) vs the full-order frequency response (solid black line) of the dc-dc converter under PID-type control.

Figure 2.12a shows the estimated frequency responses of the input-voltage loop gain (red dashed line) vs. the corresponding full-scale (black solid line) frequency responses under the PID control. From the full-scale frequency response, it can be concluded that the PM is 47.3° and $\omega_{\text{c}} = 2515 \cdot 2\pi$ rad/s. Thus, according to (2.31), the corresponding $\omega_{\text{n-c}}$ and ζ_{c} can be calculated to be $3054 \cdot 2\pi$ rad/s and 0.446, respectively. The figure indicates that the reduced-order response equals the original full-order response in the vicinity of the input-voltage-loop crossover frequency. Moreover, a Bode diagram of the complementary sensitivity function is shown in Fig. 2.12b and is well predicted by (2.28) in the vicinity of the crossover frequency, as expected.

2.2.4 Effect of photovoltaic generator

The non-idealities of source and load play a significant role in the behavior of a switched-mode converter. Therefore, in order to correctly model and predict the system operation, these effects have to be taken into account in the modeling. The transfer functions calculated in the previous section describe only the converter internal dynamics by assuming that the source and load are ideal. However, PVG is not ideal and thus its effect on the converter dynamics shall be taken into account. The operating-point-dependent dynamic effect of a PVG can be taken into account by considering the admittance Y_s parallel to the input current source as shown in Fig. 2.13.
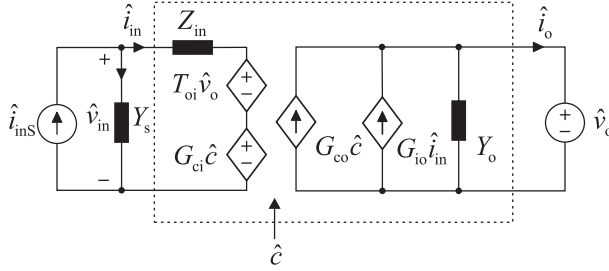

Fig. 2.13: H-parameter network with nonideal source admittance.

According to Fig. 2.13, input current can be solved as $\hat{i}_{in} = \hat{i}_{inS} - Y_s\hat{v}_{in}$, which can be substituted into (2.10) yielding

$$
\begin{bmatrix} \hat{v}_{in} \\ \hat{i}_o \end{bmatrix} = \begin{bmatrix} \dfrac{Z_{in}}{1 + Y_S Z_{in\text{-}o}} & \dfrac{T_{oi}}{1 + Y_S Z_{in\text{-}o}} & \dfrac{G_{ci\text{-}o}}{1 + Y_S Z_{in}} \\ \dfrac{G_{io}}{1 + Y_S Z_{in}} & -\dfrac{1 + Y_S Z_{in\text{-}oco}}{1 + Y_S Z_{in}} & \dfrac{1 + Y_S Z_{in\text{-}\infty}}{1 + Y_S Z_{in}} G_{co} \end{bmatrix} \begin{bmatrix} \hat{i}_{inS} \\ \hat{v}_o \\ \hat{c} \end{bmatrix} , \quad (2.32)
$$

The denominator of all transfer functions in (2.32) include the same term $Y_s Z_{in}$, which is commonly known as the *inverse minor-loop gain* [69, 81]. Thus, according to [75], the stability of the interconnected systems can be assessed on the basis of the input and output impedances at the certain interface.

As can be concluded from (2.32), the impedance-based sensitivity function $1/(1 + Y_s Z_{in})$ clearly modifies the corresponding original transfer function as long as $Y_s Z_{in}$ (Z_{in}/Z_s) has either non-zero amplitude or phase. As discussed earlier, PVG output impedance varies based on the operating point, and therefore, it affects the converter dynamics by damping the oscillatory behavior of the converter. As discussed in Section 2.1, the dynamical resistance typically dominates the PV-generator impedance over the shunt capacitor, thus it is responsible for the observed changes in the interfacing-converter

dynamics [73].

The PVG-interfacing converters include usually resonant behavior in their dynamics. The damping of the resonant behavior is affected by the impedance of the PV generator. In CCR, r_{pv} is high (i.e., Y_{pv} is low), thus parallel connected-PVG has little or practically no effect on the nominal transfer functions. On the other hand, in the CVR, r_{pv} is low and it effectively shunts the converter input capacitor yielding properties of the first-order converter. Such an operating-point-based behavior is illustrated in Fig. 2.14a, where impedance-based sensitivity functions are plotted in all operation regions in case of the underdamped voltage-boosting dc-dc converter. The behavior is quite predictable since the smallest impedance dominates in the parallel connection.
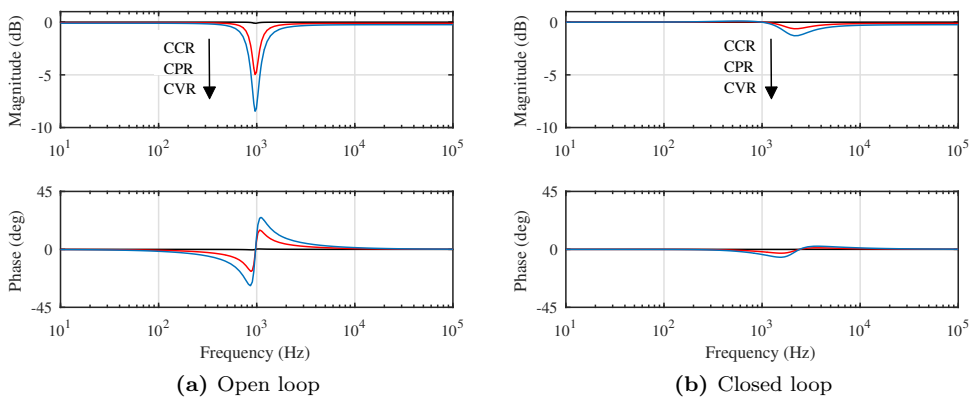

(a) Open loop   **(b)** Closed loop

Fig. 2.14: The frequency responses of the impedance-based sensitivity functions $(1/(1 + Z_{in}Y_{pv}))$ in all three operation regions.

In case of a feedback-controlled converter, the source-effect of PV generator differentiates from the corresponding open-loop behavior as shown in Fig. 2.14b. The figure represents impedance-based sensitivity function for closed-loop loop system under PID-type feedback control (cf. Fig. 2.12). If the control loop of the converter is well-designed, i.e., based on the basic principles discussed in Section 2.2.3, the input voltage follows the given voltage reference characterized by the bandwidth, phase margin and gain margin. Evidently, within control bandwidth, the input impedance of the converter is greatly reduced yielding negligible impedance-based interactions, i.e., the PVG-effect on converter transfer functions can be neglected [60, 80]. As a consequence, the high-bandwidth input-voltage-feedback loop will always maintain the input source as a current source even in CVR due to the size of the dynamic resistance.

2.2.5 Dynamic model of a PVG-interfacing voltage-boosting dc-dc converter

The current-fed boost-power-stage converter is commonly utilized as a front-end converter between a PV generator and grid-connected converter. In this way, larger variations in input voltage can be tolerated, and the maximum input voltage can be smaller compared to the single-stage conversion consisting only the inverter. Other benefits of the boost topology in photovoltaic applications are that the input current is continuous and that blocking diode is included in the topology so that no additional diode is needed. The conventional diode-switched voltage-boosting topology is studied in the thesis due to its relatively simple control scheme to highlight the important aspects of MPPT control design.
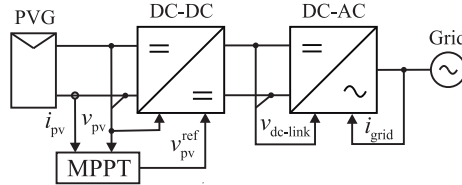

Fig. 2.15: A double-stage PV conversion scheme.

The most common way to provide an interface for photovoltaic generators is to use a general voltage-fed converter topology with an input capacitor added in its input terminal (cf. Fig. 2.16), which inherently transforms it to the corresponding current-fed converter to satisfy the terminal constraints stipulated by the source [82]. It is assumed in the later analysis that the circuit operates in the continuous-conduction-mode (CCM), which means that the inductor current or the capacitor voltage does not drop to zero during the normal operation.
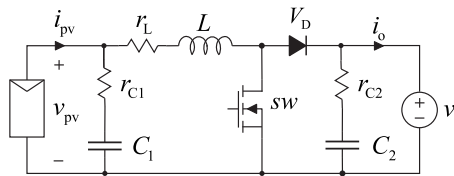
Fig. 2.16: A power stage of the CF-CO voltage-boosting dc-dc converter.

The state-space averaging process starts with defining the different sub-circuits introduced by the switching action and calculating the average model of each sub-circuit. Due to the fact that the converter operates in CCM, the switching period T_s is divided into on-time and off-time sub-circuits defined by duty ratio d. When the switch is turned on, the input voltage appears across the inductor and flowing current increases the energy

stored in the magnetic field of the inductor. In contrast, when the switch is turned off, the sum of the stored energy in the inductor and the energy from an input source is fed to the output via a diode resulting in decreasing inductor current.

The required derivatives can be found based on the well-known relations between the voltage and current in the inductor and capacitors. After applying Kirchhoff's voltage and current laws to the circuit in Fig. 2.16 with the ideal current source, the averaged state-space equations can be obtained by multiplying the on-time equations with d and off-time equations with the complement of duty ratio d' and summing them together. Finally, by utilizing first-order derivatives of the Taylor series for averaged state-space model, the linearized state-space model for current-fed-current-output voltage-boosting dc-dc converter can be obtained as follows

$$
\begin{bmatrix} \dfrac{\hat{i}_{\mathrm{L}}}{dt} \\[2ex] \dfrac{\hat{v}_{\mathrm{C1}}}{dt} \\[2ex] \dfrac{\hat{v}_{\mathrm{C2}}}{dt} \end{bmatrix} = \begin{bmatrix} -\dfrac{R_{\mathrm{e}}}{L} & \dfrac{1}{L} & 0 \\[2ex] -\dfrac{1}{C_1} & 0 & 0 \\[2ex] 0 & 0 & -\dfrac{1}{r_{\mathrm{C2}}C_2} \end{bmatrix} \begin{bmatrix} \hat{i}_{\mathrm{L}} \\[2ex] \hat{v}_{\mathrm{C1}} \\[2ex] \hat{v}_{\mathrm{C2}} \end{bmatrix} + \begin{bmatrix} \dfrac{r_{\mathrm{C1}}}{L} & -\dfrac{D'}{L} & \dfrac{V_{\mathrm{e}}}{L} \\[2ex] \dfrac{1}{C_1} & 0 & 0 \\[2ex] 0 & \dfrac{1}{r_{\mathrm{C2}}C_2} & 0 \end{bmatrix} \begin{bmatrix} \hat{i}_{\mathrm{pv}} \\[2ex] \hat{v}_{\mathrm{o}} \\[2ex] \hat{d} \end{bmatrix}
$$

$$(2.33)$$

$$
\begin{bmatrix} \hat{v}_{\mathrm{pv}} \\[2ex] \hat{i}_{\mathrm{o}} \end{bmatrix} = \begin{bmatrix} -r_{\mathrm{C1}} & 1 & 0 \\[2ex] D' & 0 & \dfrac{1}{r_{\mathrm{C2}}} \end{bmatrix} \begin{bmatrix} \hat{i}_{\mathrm{L}} \\[2ex] \hat{v}_{\mathrm{C1}} \\[2ex] \hat{v}_{\mathrm{C2}} \end{bmatrix} + \begin{bmatrix} r_{\mathrm{C1}} & 0 & 0 \\[2ex] 0 & -\dfrac{1}{r_{\mathrm{C2}}} & -I_{\mathrm{pv}} \end{bmatrix} \begin{bmatrix} \hat{i}_{\mathrm{pv}} \\[2ex] \hat{v}_{\mathrm{o}} \\[2ex] \hat{d} \end{bmatrix},
$$

$$(2.34)$$

where auxiliary variables R_{e} and V_{e}, further represented in (2.35), are introduced to simplify the notations.

$$R_{\mathrm{e}} = r_{\mathrm{C1}} + r_{\mathrm{L}} + Dr_{\mathrm{sw}} + D'r_{\mathrm{D}} \qquad (2.35\mathrm{a})$$

$$V_{\mathrm{e}} = (r_{\mathrm{D}} - r_{\mathrm{sw}})I_{\mathrm{pv}} + V_{\mathrm{o}} + V_{\mathrm{D}} \qquad (2.35\mathrm{b})$$

The symbolically expressed open-loop transfer functions of the converter are given in (2.36), which are already validated in the previous research in [66].

$$Z_{\text{in-o}} = \frac{1}{LC_1} \left(R_{\text{e}} - r_{\text{C1}} + sL \right) \left(1 + sr_{\text{C1}}C_1 \right) \frac{1}{\Delta} \tag{2.36a}$$

$$T_{\text{oi-o}} = \frac{D'}{LC_1} \left(1 + sr_{\text{C1}}C_1 \right) \frac{1}{\Delta} \tag{2.36b}$$

$$G_{\text{ci-o}} = -\frac{V_{\text{e}}}{LC_1} \left(1 + sr_{\text{C1}}C_1 \right) \frac{1}{\Delta} \tag{2.36c}$$

$$G_{\text{io-o}} = -\frac{D'}{LC_1} \left(1 + sr_{\text{C1}}C_1 \right) \frac{1}{\Delta} \tag{2.36d}$$

$$G_{\text{co-o}} = -I_{\text{pv}} \left(s^2 - s \left(\frac{D'V_{\text{e}}}{LI_{\text{pv}}} - \frac{R_{\text{e}}}{L} \right) + \frac{1}{LC_1} \right) \frac{1}{\Delta} \tag{2.36e}$$

$$Y_{\text{o-o}} = \frac{D'^2 s}{\Delta L} + \frac{sC_2}{1 + sr_{\text{C2}}C_2}, \tag{2.36f}$$

where the determinant of the transfer functions, denoted by Δ, is

$$\Delta = s^2 + s\frac{R_{\text{e}}}{L} + \frac{1}{LC_1}. \tag{2.37}$$

It is worth noting that the transfer functions calculated in (2.36) describe only the converter internal dynamics by assuming that PVG is an ideal current source. Based on the prior analysis in Section 2.2.4, the corresponding source-affected transfer functions can be calculated based on (2.32). Thus, PVG-affected control-to-duty-ratio transfer function $G_{\text{ci-o}}^{\text{pv}}$ can be given as a general second-order transfer function as follows

$$G_{\text{ci-o}}^{\text{pv}} = \frac{G_{\text{ci-o}}}{1 + Z_{\text{in-o}}Y_{\text{pv}}} = -V_{\text{e}} \frac{\omega_{\text{n}}^2(1 + s/\omega_{\text{z-esr}})}{s^2 + 2\zeta_{\text{pv}}\omega_{\text{n}}s + \omega_{\text{n}}^2}, \tag{2.38}$$

where

$$\zeta_{\text{pv}} = \frac{L + C_1 \left(R_{\text{e}}(r_{\text{pv}} + r_{\text{C1}}) - r_{\text{C1}}^2 \right)}{2\sqrt{LC_1(r_{\text{pv}} + r_{\text{C1}})(r_{\text{pv}} + R_{\text{e}} - r_{\text{C1}})}} \approx \frac{1}{2} \left(R_{\text{e}}\sqrt{\frac{C_1}{L}} + \frac{1}{r_{\text{pv}}}\sqrt{\frac{L}{C_1}} \right) \tag{2.39a}$$

$$\omega_{\text{n}} = \sqrt{\frac{r_{\text{pv}} + R_{\text{e}} - r_{\text{C1}}}{(r_{\text{pv}} + r_{\text{C1}})LC_1}} \approx \frac{1}{\sqrt{LC_1}}. \tag{2.39b}$$

$$\omega_{\text{z-esr}} = \frac{1}{sr_{\text{C1}}C_1} \tag{2.39c}$$

The final forms in (2.39a) and (2.39b) can be obtained by assuming $r_{\text{pv}} \gg r_{\text{C1}}$ and

$r_{\mathrm{pv}} \gg R_{\mathrm{e}}$, which can be justified for practical double-stage PV systems operating around MPP.

2.3 Conclusions

Photovoltaic generator characteristic curve is usually split into constant current and constant voltage regions, separated by the maximum power point. Detailed analysis of photovoltaic generator's P-V curve shape and power-transient behavior revealed that an exact maximum power point does not exist in practice due to the finite resolution of measuring facility. Instead, the steady-state operating point may reside within a region (referred to as constant power region) around the maximum power point. Thus, during the maximum-power-point tracking process, the operating point may reside in any of the three regions even under constant atmospheric conditions. The PVG power has a distinct characteristic in each region determined by the relation between dynamic and static resistances of a PVG.

This section also proposed analytical methods to analyze the fundamental transient behavior of PVG-interfacing converter by focusing on low or high-frequency behavior around the loop-gain crossover frequency. It was concluded that the closed-loop control-to-input-voltage transfer functions of I-control or PID-control equipped converter can be reduced to first-order and second-order transfer functions, respectively. That enables to approximate PV power transient analytically revealing the factors affecting the transient behavior similarly as in open-loop converter providing valuable tools for determining the settling time of a transient response.

3 MAXIMUM-POWER-POINT TRACKING IN PHOTOVOLTAIC APPLICATIONS

This chapter discusses the design process of the fixed-step perturbative algorithms focusing on the constraints of perturbation frequency and step size. Based on the derived analysis in Chapter 2 and [P1]-[P6], the methods are provided to estimate the dynamic behavior of PVG power.

3.1 Perturbative MPPT techniques

Fixed-step P&O and IC algorithms are probably the most frequently used MPPT methods, both related to the class of perturbative or direct algorithms. There, a perturbation Δx is injected into the system by the MPPT algorithm every ΔT seconds. After a transient lasting T_Δ seconds (cf. Fig. 1.8), the polarity and sometimes the size of two successive PVG power measurements is detected. Thus, the next perturbation $x(k+1)$ is updated based on (1.4). In this respect, two design parameters of the P&O and IC methods are the perturbation frequency, i.e., the inverse of time interval ΔT between two consecutive perturbation instants) and the perturbation step size Δx.

IC method is usually assumed to improve the steady-state and dynamic performance of the P&O algorithm [41]. However, it has been shown that there is no practical difference in the performance between these two methods when the design parameters of both algorithms are properly chosen as demonstrated in [56, 83]. In fact, the only difference is the numerical calculation of derivatives in the IC method. According to [56], using the IC method, the step size can be defined a slightly lower than in the P&O method to achieve similar dynamic performance in rapidly changing atmospheric conditions. Although the incremental conductance method requires a little bit more computational burden compared to the P&O method due to derivative calculations, it is not an issue even for modern microcontrollers. However, analyzing the operation of the P&O algorithm is more straightforward, and therefore, the thesis focuses on the optimization design parameters of the P&O algorithm.

Classification of two main MPPT control schemes can be seen in Fig. 3.1, where the perturbed variable x is either the duty ratio or voltage depending on the control scheme [18]. The first one involves direct perturbation of the interfacing power-converter duty

ratio generated by the MPPT. Since the MPPT is not affecting the dynamics of the PVG-interfacing converter, such an MPPT control scheme can be considered to be operating as open loop indicating its dynamical characteristics. In contrast, in the latter scheme, the MPPT algorithm perturbs the PVG reference voltage while input-voltage controller ensures correct tracking by appropriately varying the duty ratio of the interconnected-converter (cf. Fig. 3.1). While the former is simpler, the latter is often preferred due to improved speed and robustness to irradiation changes [18].
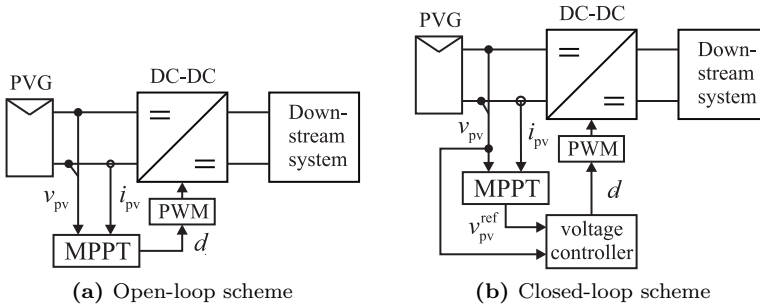

(a) Open-loop scheme   **(b)** Closed-loop scheme

Fig. 3.1: MPPT control structures.

Alternatively, the MPPT operation can be achieved by using the output terminal variables of the dc-dc converter rather than input ones [84]. Depending on the implemented topology, that may simplify the implementation of the MPPT algorithm. For example, if a downstream system of the dc-dc converter maintains the output terminal voltage constant, the power is directly proportional to the current flowing through the dc-link. Thus, the power can be maximized by tracking the maximum current of the dc-link.

The problem in the optimization process of the fixed-step perturbative algorithms is the trade-off between fast-tracking and low steady-state oscillations, which requires more detailed analysis of the PV system to tune the algorithm design parameters: perturbation step size and frequency. Most of case studies in the literature follow the generalized guidelines given in [57] and [18], where the perturbation period and step size of direct MPPT algorithms are recommended to be selected at MPP, corresponding to standard test conditions (1000 W/m^2 irradiation and 25°C temperature). However, it is well known that PVG dynamic resistance significantly affects the dynamic behavior of combined solar energy conversion system by modifying the open-loop damping factor [66, 72, 73, 85].

Several improvements have been published to overcome the drawbacks of perturbative MPPT algorithms. Since the fixed-step P&O algorithm introduces steady-state oscillations, most of the introduced improvements are focused on adjusting the perturbation step size to improve the steady-state efficiency and improve its tracking ability in fast-varying atmospheric conditions [86, 87]. Usually these algorithms need some predefined

variables based on the characteristics of the PVG to work correctly.

Basically, the adaptive MPPT algorithm adjusts the step size Δx depending on how far the operation voltage is from the MPP. When the present operating point is far from MPP, a large step-size is used to achieve the MPP faster. On the contrary, a small step size is used when operating near the MPP to minimize steady-state oscillations. In order to calculate the value of step size, the power-voltage derivative $\Delta p_{\mathrm{pv}}/\Delta v_{\mathrm{pv}}$ is introduced as a suitable parameter for tuning the step size [62]. The P-V derivative suits well for adaptive-step purposes as can be concluded from in Fig. 3.2, which represents the correlation between the P-V curve and its derivative. When the operating point is located far from the MPP, the step size has a large value while it monotonically decreases when the operating point is approaching the MPP.
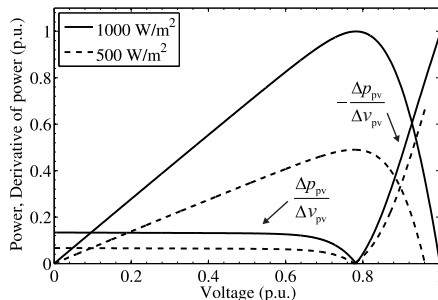

Fig. 3.2: P-V curve and the absolute value of derivative of P-V curve in two different irradiance levels.

In case of an open-loop dc-dc converter, where MPP tracker controls directly the duty ratio d, the perturbation step size is updated according to (3.1) [88]

$$x(k) = x(k-1) \pm N \left| \frac{\Delta P_{\mathrm{pv}}}{\Delta V_{\mathrm{pv}}} \right| = x(k-1) \pm N \left| \frac{P_{\mathrm{pv}}(k) - P_{\mathrm{pv}}(k-1)}{V_{\mathrm{pv}}(k) - V_{\mathrm{pv}}(k-1)} \right|, \tag{3.1}$$

where $x(k)$ and $x(k-1)$ are the converter duty ratio or voltage reference at time instants k and $k-1$, respectively. Scaling factor N is needed to adjust $|\Delta P_{\mathrm{pv}}/\Delta V_{\mathrm{pv}}|$ for a proper duty ratio level, and it has a significant effect on the performance of the adaptive-step algorithm. Moreover, adaptive-step MPPT algorithms have been show to be very sensitive to the drift phenomenon as already illustrated in Fig. 1.9. Thus, in the light of recent publication [58], it does not seem to be superior alternative for fixed-step algorithm without detailed analysis of factors affecting its operation in steady-state and dynamic conditions. This thesis focuses, however, the constraints of fixed-step perturbative algorithms which have been shown to provide a great performance if properly designed.

3.2   Perturbation frequency constraints

Perturbation frequency is one design parameters of perturbative MPPT algorithm, and its design process is fundamentally linked to the time domain behavior of PVG power, as it is the optimization function (cf. (1.8)). Although the perturbation frequency does not directly affect the tracking efficiency, it has a significant impact on the operation of the algorithm in steady-state and dynamic atmospheric conditions. That is because the perturbation frequency defines the tracking performance (i.e., power ramp rate $\Delta P_\mathrm{x} \Delta T$) under dynamic conditions in conjunction with the perturbation step size. Thus, to predict the behavior of the algorithm, the maximum perturbation frequency should be limited by the settling time of the PVG power transient induced by the injected perturbation, i.e., the PVG power transient needs to be settled to its steady-state value before applying the next perturbation.

Alternatively, the perturbation-frequency constraint can be explained by the relative bandwidth of inner and outer control loops in case of the multiloop control scheme in Fig. 3.1b. As discussed earlier, MPPT creates an additional feedback loop in the converter dynamics, whereas it generates either the reference for the duty ratio or the PV voltage depending on the chosen control topology. As commonly stated in the control engineering, if a control system contains two inner loops, the outer loop must have a lower bandwidth than the inner loop to guaranteeing a proper system operation. That is because the output of the inner control loop is used as an input for outer loop. Thus it needs to be settled to its steady-state value in order not to get confused by the transient behavior caused by the inner control loop.

The first detailed studies regarding optimizing the P&O algorithm design parameters are presented in [57], where the authors generated the dynamic model for the PVG-interconnected boost converter in order to determine the minimum settling time to prevent drift phenomenon. However, alternative approaches are also introduced. Authors in [63] recommended to use 1/10 of the input-voltage-feedback-loop crossover frequency. However, as stated earlier in (2.31), the settling time of the transient cannot be determined solely based on the control bandwidth since damping factor and phase margin also have a great impact on the outcome. Later, a few other studies have introduced simplified guidelines to determine an optimized value for the perturbation frequency and step size. For example, the authors in [64] claimed that the speed of the MPPT algorithm should be in a range of 0.1–1.0 % of MPP voltage per second to reach annual MPPT efficiency of 99.9 %. The authors have introduced another approach in [65] utilizing shorter perturbation period. In that case, the PVG power never reaches the steady-state yielding chaotic behavior around the MPP. Despite the interesting approach, such a high-frequency perturbation cannot be used in multi-loop converter-control scheme due to the constraints of control bandwidths between outer and inner control loops.

According to Fig. 2.14, damping is reduced when the operating point moves into the CCR due to the increase in dynamic resistance, i.e., the settling time of PVG power transient increases as well and would hence be longest in the short-circuit condition. Thus, in case the operating point is expected to occasionally reside in the CCR, the perturbation-frequency design guidelines must take this into account, even though selecting a higher ΔT results in slower tracking speed and reduced efficiency. When the operating point moves from CPR to CCR, the dynamic resistance rapidly increases (cf. Fig. 2.3), justifying the reconsideration of perturbation-frequency design guidelines, presented in [18, 57], stating that the perturbation frequency should be designed at STC MPP.

It is worth mentioning that the perturbation period much lower than the settling time of the system response has been recently adopted in [65, 89]. According to the authors, it is not necessary to wait for the system to reach a steady state after each MPPT perturbation. As an advantage, higher efficiency and faster response to irradiance changes may be achieved. By contrast, the steady-state oscillation for the higher perturbation frequency is larger than that for the lower perturbation frequency due to the confusion caused by noise. Even though the only experimental investigation was conducted without a solid analytical background, this is undoubtedly a very interesting and promising future research direction.

In the following sections, the settling time T_Δ is derived for CCR, CPR and CVR to reveal the highest value, based on which the perturbation period should be selected. The diode-switched boost converter, discussed in Section 2.2.5, is used as a design example in the simulations. However, it should be noted that the obtained results are also valid for PVG-interconnected synchronous-rectification voltage-boosting dc-dc converters possessing higher efficiency and enhanced thermal performance [90].

3.2.1 Open-loop-operated converters

Referring to the general representation of a solar-energy-conversion system shown in (2.32), the corresponding equations for an open-loop converter can be given as in (3.2) by setting $\hat{c} = \hat{d}$. It is known that the temperature on the PV cell affects significantly the PVG power characteristics, but its dynamics is quite slow due to the large thermal capacity of the photovoltaic modules, as discussed in [57]. Therefore, the temperature effect is disregarded in (3.2) as well. The control-to-PVG-voltage transfer function in (3.2a), i.e., the last term of the equations, is of particular interest for the perturbation frequency design. Thus, its effect on the PVG power is further discussed in the following sections.

$$\hat{v}_{\text{pv}} = \frac{Z_{\text{in}}}{1 + Z_{\text{in}}Y_{\text{pv}}}\hat{i}_{\text{ph}} + \frac{T_{\text{oi}}}{1 + Z_{\text{in}}Y_{\text{pv}}}\hat{v}_{\text{o}} + \frac{G_{\text{ci}}}{1 + Z_{\text{in}}Y_{\text{pv}}}\hat{d} \tag{3.2a}$$

$$\hat{i}_{\text{pv}} = \frac{1}{1 + Z_{\text{in}}Y_{\text{pv}}}\hat{i}_{\text{ph}} - \frac{Y_{\text{pv}}T_{\text{oi}}}{1 + Z_{\text{in}}Y_{\text{pv}}}\hat{v}_{\text{o}} - \frac{Y_{\text{pv}}G_{\text{ci}}}{1 + Z_{\text{in}}Y_{\text{pv}}}\hat{d}. \tag{3.2b}$$

Practical open-loop-operated PVG-interfaced converters can be considered as under-damped systems, where the initial transient behavior can be characterized by the second-order transfer function as concluded in Section 2.2. Therefore, the PV-voltage transient induced by a step change of duty ratio ΔD can be given in Laplace domain as follows

$$\hat{v}_{\text{pv}}(s) = G_{\text{ci-o}}^{\text{pv}} \cdot \frac{\Delta D}{s} = -V_{\text{e}}\Delta D \left(\frac{1}{s} - \frac{s + 2\zeta_{\text{pv}}\omega_{\text{n}} - \dfrac{\omega_{\text{n}}^2}{\omega_{\text{z-esr}}}}{s^2 + 2\zeta_{\text{pv}}\omega_{\text{n}}s + \omega_{\text{n}}^2} \right) \tag{3.3}$$

Hence, the corresponding time-domain response is

$$\hat{v}_{\text{pv}}(t) = V_{\text{e}}\Delta D \left(1 - \frac{\sqrt{1 + \dfrac{\omega_{\text{n}}}{\omega_{\text{z-esr}}}\left(\dfrac{\omega_{\text{n}}}{\omega_{\text{z-esr}}} - 2\zeta_{\text{pv}}\right)}}{\sqrt{1 - \zeta_{\text{pv}}^2}} \exp(-\zeta_{\text{pv}}\omega_{\text{n}}t) \cdot \sin\left(\omega_{\text{d}}t + \tan^{-1}\left(\frac{\sqrt{1 - \zeta_{\text{pv}}^2}}{\zeta_{\text{pv}} - \dfrac{\omega_{\text{n}}}{\omega_{\text{z-esr}}}}\right)\right) \right), \tag{3.4}$$

where $\omega_{\text{d}} = \omega_{\text{n}}\sqrt{1 - \zeta_{\text{pv}}^2}$ and $0 < \zeta_{\text{pv}} < 1$. Typically input capacitance is designed to be low with low ESR value resulting the frequency of the capacitor-ESR-induced zero $\omega_{\text{z-esr}} = 1/sr_{\text{C1}}C_1$ appearing much higher than the natural frequency ω_{n}. That further simplifies (3.4) into

$$\hat{v}_{\text{pv}}(t) \approx V_{\text{e}}\Delta D \left(1 - \frac{1}{\sqrt{1 - \zeta_{\text{pv}}^2}} \exp(-\zeta_{\text{pv}}\omega_{\text{n}}t) \cdot \sin\theta(t) \right) \tag{3.5}$$

with $\theta(t) = \omega_{\text{d}}t + \tan^{-1}\left(\sqrt{1 - \zeta_{\text{pv}}^2}/\zeta_{\text{pv}}\right)$. Therefore, utilizing (2.4) and (3.5), the time-

domain behavior of PVG power will be

$$\hat{p}_{\mathrm{pv}}(t) \approx -\Delta P_{\mathrm{pv}}^{\mathrm{CCR}}\left(1 \pm \frac{1}{\sqrt{1-\zeta_{\mathrm{pv}}^2}}\exp(-\zeta_{\mathrm{pv}}\omega_{\mathrm{n}}t)\cdot\sin\theta(t)\right) \tag{3.6a}$$

in CCR with $\Delta P_{\mathrm{pv}}^{\mathrm{CCR}} = I_{\mathrm{pv}}V_{\mathrm{e}}\Delta D$,

$$\hat{p}_{\mathrm{pv}}(t) \approx -\Delta P_{\mathrm{pv}}^{\mathrm{CVR}}\left(1 \pm \frac{1}{\sqrt{1-\zeta_{\mathrm{pv}}^2}}\exp(-\zeta_{\mathrm{pv}}\omega_{\mathrm{n}}t)\cdot\sin\theta(t)\right) \tag{3.6b}$$

in CVR with $\Delta P_{\mathrm{pv}}^{\mathrm{CVR}} = V_{\mathrm{pv}}V_{\mathrm{e}}\Delta D/r_{\mathrm{pv}}$ and

$$
\begin{aligned}
\hat{p}_{\mathrm{pv}}(t) &\approx -\Delta P_{\mathrm{pv}}^{\mathrm{CPR}}\left(1 \pm \frac{1}{\sqrt{1-\zeta_{\mathrm{pv}}^2}}\exp(-\zeta_{\mathrm{pv}}\omega_{\mathrm{n}}t)\cdot\sin\theta(t)\right)\\
&= -\Delta P_{\mathrm{pv}}^{\mathrm{CPR}}\left(\begin{array}{l}1 - 2\dfrac{1}{\sqrt{1-\zeta_{\mathrm{pv}}^2}}\exp(-\zeta_{\mathrm{pv}}\omega_{\mathrm{n}}t)\cdot\sin\theta(t)\\[2mm] + \dfrac{1}{2(1-\zeta_{\mathrm{pv}}^2)}\exp(-2\zeta_{\mathrm{pv}}\omega_{\mathrm{n}}t)\cdot(1-\cos 2\theta(t))\end{array}\right)
\end{aligned}
\tag{3.6c}
$$

in CPR with $\Delta P_{\mathrm{pv}}^{\mathrm{CPR}} = (V_{\mathrm{dc}}\Delta D)^2/R_{\mathrm{pv}}$. The corresponding steady-state PVG power variations and transient behaviors are well-evident in (3.6).
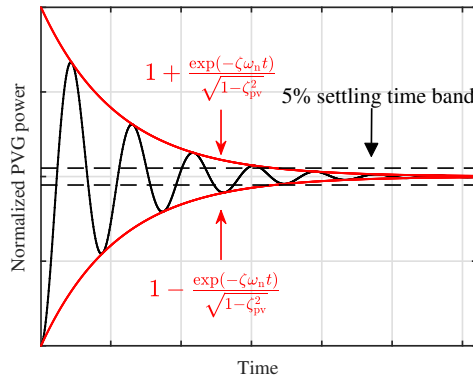

Fig. 3.3: Envelope curve of the transient response.

Figure 3.3 illustrates the under-damped transient response and their corresponding

envelope behaviors in CCR and CVR. It may be concluded that the exponent functions and their corresponding coefficients in (3.6) are the envelope curves of the transient response. Thus, the PVG-power response curve will always remain within the pair of the envelope curves. The power transient settling time is dictated by corresponding envelope behavior, given by

$$
env\left(\hat{p}_{\mathrm{pv}}(t)\right) = -\Delta P_{\mathrm{pv}}^{\mathrm{CCR}} \left(1 \pm \frac{1}{\sqrt{1-\zeta_{\mathrm{pv}}^2}} \exp(-\zeta_{\mathrm{pv}}\omega_{\mathrm{n}}t) \right) \tag{3.7a}
$$

in CCR,

$$
env\left(\hat{p}_{\mathrm{pv}}(t)\right) = -\Delta P_{\mathrm{pv}}^{\mathrm{CVR}} \left(1 \pm \frac{1}{\sqrt{1-\zeta_{\mathrm{pv}}^2}} \exp(-\zeta_{\mathrm{pv}}\omega_{\mathrm{n}}t) \right) \tag{3.7b}
$$

in CVR, and

$$
env\left(\hat{p}_{\mathrm{pv}}(t)\right) = -\Delta P_{\mathrm{pv}}^{\mathrm{CPR}} \left(\begin{array}{l} 1 - 2\dfrac{1}{\sqrt{1-\zeta_{\mathrm{pv}}^2}} \exp(-\zeta_{\mathrm{pv}}\omega_{\mathrm{n}}t) \\ + \dfrac{1}{2(1-\zeta_{\mathrm{pv}}^2)} \exp(-2\zeta_{\mathrm{pv}}\omega_{\mathrm{n}}t) \end{array} \right) \tag{3.7c}
$$

in CPR.

The speed of decay of the transient response depends on the value of the time constant $\tau = 1/(\zeta\omega_{\mathrm{n}})$, i.e., for a given ω_{n}, settling time T_Δ is a function of the damping ratio ζ. Therefore, the corresponding settling times T_Δ of (3.7) are obtained by solving

$$
env(\hat{p}_{\mathrm{pv}}(t))|_{t=T_\Delta} = -\Delta P_{\mathrm{pv}}(1 \pm \Delta) \tag{3.8}
$$

with $0 < \Delta < 1$ denoting the relative magnitude of settling band as

$$
T_\Delta = -\frac{1}{\zeta_{\mathrm{pv}}\omega_{\mathrm{n}}} \ln\left(\Delta\sqrt{1-\zeta_{\mathrm{pv}}^2} \right) \tag{3.9a}
$$

in CCR and CVR and

$$T_\Delta = -\frac{1}{\zeta_{pv}\omega_n} \ln\left(\frac{\Delta}{2}\sqrt{1-\zeta_{pv}^2}\right) \tag{3.9b}$$

in CPR. It should be emphasized that since ζ_{pv} depends on r_{pv}, the settling times must be evaluated separately for each region, taking into account the appropriate values of PVG dynamic resistance.

According to (3.5) and taking into account (2.39a), the damping factor satisfies

$$\zeta_{pv,min} < \zeta_{pv} = \frac{1}{2}\left(\frac{1}{r_{pv}}\sqrt{\frac{L}{C_1}} + R_e\sqrt{\frac{C_1}{L}}\right) < \zeta_{pv,max} \tag{3.10}$$

with

$$
\begin{aligned}
\zeta_{pv,min} &= \zeta_{pv}|_{SC} = \frac{1}{2}\left(\frac{1}{r_{sh}}\sqrt{\frac{L}{C_1}} + R_e\sqrt{\frac{C_1}{L}}\right) \approx \frac{R_e}{2}\sqrt{\frac{C_1}{L}}, \\
\zeta_{pv,max} &= \zeta_{pv}|_{OC} = \frac{1}{2}\left(\frac{1}{r_s}\sqrt{\frac{L}{C_1}} + R_e\sqrt{\frac{C_1}{L}}\right) \approx \frac{1}{2r_s}\sqrt{\frac{L}{C_1}},
\end{aligned}
\tag{3.11}
$$

Due to the same expression for PVG power equations in CCR (3.6a) and CVR (3.6b), the settling time expressions are also the same in both regions. Apparently, the settling time increases monotonically with the decrease in ζ_{pv}, hence $T_\Delta|_{OC} < T_\Delta|_{SC}$ since $\zeta_{pv}|_{SC} < \zeta_{pv}|_{OC}$, i.e., the shortest settling time would be expected in CVR.

In order to compare the settling times in CPR and CCR, it is assumed that $\zeta_{pv} \ll 1$ in both regions. This is rather practical assumption, since the parasitic elements are usually designed to be low to increasing the efficiency. Applying the approximation $\ln(1-x)|_{x\ll 1} \approx -x$ to (3.9), $T_\Delta\omega_n$ can be given by

$$T_\Delta\omega_n \approx -\frac{\ln(\Delta)}{\zeta_{pv}} \tag{3.12a}$$

in CCR, and

$$T_\Delta\omega_n \approx -\frac{\ln\left(\frac{\Delta}{2}\right)}{\zeta_{pv}} \tag{3.12b}$$

in CPR. The CCR/CPR settling time ratio is then

$$\left.\frac{T_\Delta|_{\text{CCR}}}{T_\Delta|_{\text{CPR}}}\right. = \frac{k_\Delta\,\zeta_{\text{pv}}|_{\text{CPR}}}{\zeta_{\text{pv}}|_{\text{CCR}}} \tag{3.13}$$

with $k_\Delta = \ln(\Delta)/\ln(\Delta/2)$. Hence, in case $k_\Delta\,\zeta_{\text{pv}}|_{\text{CPR}} > \zeta_{\text{pv}}|_{\text{CCR}}$, the settling time in CCR would be higher than in CPR. In classical control theory, $0.02 < \Delta < 0.1$ is typically used, corresponding to $0.77 < k_\Delta < 0.85$. On the other hand, the worst case CPR/CCR damping factor ratio is given by

$$\frac{\zeta_{\text{pv}}|_{\text{MPP}}}{\zeta_{\text{pv}}|_{\text{SC}}} \approx \frac{\dfrac{1}{2\,r_{\text{pv}}|_{\text{MPP}}}\sqrt{\dfrac{L}{C_1}} + \dfrac{R_{\text{e}}}{2}\sqrt{\dfrac{C_1}{L}}}{\dfrac{R_{\text{e}}}{2}\sqrt{\dfrac{C_1}{L_1}}} = 1 + \frac{1}{R_{\text{e}}\,r_{\text{pv}}|_{\text{MPP}}}\frac{L}{C_1}. \tag{3.14}$$

The second term in the right-hand side of (3.14) is typically much larger than unity, since $R_{\text{e}}\,r_{\text{pv}}|_{\text{MPP}} \ll 1$. Combining (3.12) and (3.14), it may be stated that in practical systems $T_\Delta|_{\text{CCR}} > T_\Delta|_{\text{CPR}}$ holds. Consequently, the time interval ΔT between two consecutive perturbation instants must be selected so that

$$\Delta T > T_\Delta|_{\text{SC}} = -\frac{1}{\zeta_{\text{pv}}|_{\text{SC}}\omega_{\text{n}}}\ln\left(\Delta\sqrt{1 - \zeta_{\text{pv}}^2|_{\text{SC}}}\right). \tag{3.15}$$

Moreover, according to $\zeta_{\text{pv}}|_{\text{SC}}$ definition in (3.11), in case the value of r_{sh} is unknown, it may be assumed to be high enough to allow using $\zeta_{\text{pv}}|_{\text{SC}} \approx \frac{R_{\text{e}}}{2}\sqrt{\frac{C_1}{L}}$, which is totally independent of the PVG and relies only on the component values of the interconnected converter.

Figure 3.4 shows the simulated PVG-power responses in different regions when a step change of 0.05 in duty ratio is applied. The developed simulation models in this thesis were implemented in MATLAB® Simulink, which easily enables to combine dc-dc converter and PVG models together. The converter used in the simulation is specified in Fig. 2.16. Figure 3.4 shows clearly that the region, where the settling process shall be studied, is CCR. As Fig. 2.4 implies, the PVG-power transient is very small in CPR compared to the PVG-power transient in the other regions. The similar transients are also later shown in Fig. 4.2 based on experimental measurements validating the comments given based on the simulations and the developed theory in (2.4).
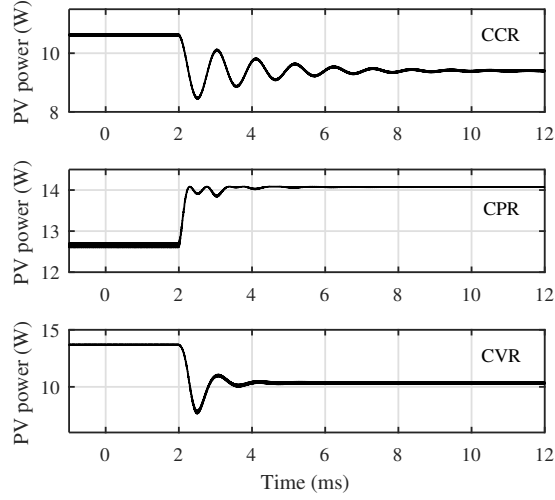
Fig. 3.4: The behavior of the PV power transient in different operational regions when a step change of 0.05 in duty ratio is applied.

3.2.2 Closed-loop-operated converters

In case of input-voltage-feedback-controlled converters, the PV-generator effect on the system damping behavior is quite different, especially, when the input-voltage-feedback-loop crossover frequencies are designed to be sufficiently lower or higher than the resonant frequency of the converter as discussed in Section 2.2.3. That is because the closed-loop input impedance ($Z_{\text{in-c}}$) is rather small especially at the frequencies, where the feedback-loop gain is high (i.e., $Z_{\text{in-c}}Y_{\text{pv}} \approx Z_{\text{in-c}}/r_{\text{pv}} \ll 1$). Thus, it affects only marginally the magnitude of the loop and the phase margin when the crossover frequency of the input-voltage loop gain is located far enough from the resonant frequency. Therefore, the set of equations in (2.32) becomes

$$\hat{v}_{\text{pv}} \approx Z_{\text{in-c}}\hat{i}_{\text{ph}} + T_{\text{oi-c}}\hat{v}_{\text{o}} + G_{\text{ci-c}}\hat{v}_{\text{pv}}^{\text{ref}} \tag{3.16a}$$

$$\hat{i}_{\text{pv}} \approx \hat{i}_{\text{ph}} - Y_{\text{pv}}T_{\text{oi-c}}\hat{v}_{\text{o}} - Y_{\text{pv}}G_{\text{ci-c}}\hat{v}_{\text{pv}}^{\text{ref}}. \tag{3.16b}$$

If the changes in atmospheric conditions and output voltage $\hat{v}_{\text{o}}$ are negligible, the only relevant elements from the MPP-tracking perturbation-frequency point of view are the last right-most elements in (3.16). Thus, the PV-voltage transient induced by a step

61

change in the input-voltage reference $\Delta V_{\mathrm{pv}}^{\mathrm{ref}}$ can be given in Laplace domain as follows

$$\hat{v}_{\mathrm{pv}}(s) = G_{\mathrm{ci\text{-}c}} \cdot \frac{\Delta V_{\mathrm{pv}}^{\mathrm{ref}}}{s} = \frac{1}{G_{\mathrm{se}}^{\mathrm{v}}} \frac{L_{\mathrm{in}}}{1 + L_{\mathrm{in}}} \cdot \frac{\Delta V_{\mathrm{pv}}^{\mathrm{ref}}}{s} \tag{3.17}$$

Due to the complexity of (3.17), the behavior of the PV voltage and current transient induced by a step change in the PV reference voltage can be naturally analyzed by using the software packages as performed, for example, in [57]. This kind of approach does not, however, give enough information on the factors affecting the transient behavior similarly as in case of an open-loop converter discussed in the previous section. If the input-voltage loop gain is substituted as such (i.e., (3.16)) in the corresponding sensitivity function to extract the time-domain functions associated with the corresponding transient behavior, the inverse transformation process will be too complicated and involves unnecessary time functions. However, the settling time of the power transient in closed-loop systems can be approximated by utilizing the methods introduced in Section 2.2.3.

It is worth noting that the following analysis only treats the case, where the input-voltage controller (cf. Fig. 3.1b) directly sets the duty ratio of the converter. In case of cascaded input-voltage-feedback implementation, which include current-mode control as in [91, 92], the dependence on the PVG properties may still exist and the outcomes presented in this paper may not be valid.

Settling-time approximation under I-type control

In case of an I-type controller, the input-voltage feedback-loop crossover frequency would be less than the resonant frequency of the converter for providing sufficient attenuation at the resonant frequency, i.e., the resonant peak value should be less than -10 dB for eliminating the effect of the resonance on the settling behavior. This means that the damping factor would be rather high, because the PM would be close to $90°$, and therefore, the roots of the second-order denominator in (3.17) would be well separated (i.e., $(s + \omega_{\mathrm{n\text{-}c}}/2\zeta_{\mathrm{c}})(s + 2\zeta_{\mathrm{c}}\omega_{\mathrm{n\text{-}c}}) = 0$). As a consequence, the PVG voltage transient behavior can be characterized by the reduced first-order model in (2.25) by

$$\hat{v}_{\mathrm{pv}}(s) = G_{\mathrm{ci\text{-}c}}^{\mathrm{I}} \cdot \frac{\Delta V_{\mathrm{pv}}^{\mathrm{ref}}}{s} \approx \frac{\omega_{\mathrm{n\text{-}c}}/2\zeta_{\mathrm{c}}}{s + \omega_{\mathrm{n\text{-}c}}/2\zeta_{\mathrm{c}}} \cdot \frac{\Delta V_{\mathrm{pv}}^{\mathrm{ref}}}{s} = \Delta V_{\mathrm{pv}}^{\mathrm{ref}} \left(\frac{1}{s} - \frac{1}{s + \dfrac{\omega_{\mathrm{n\text{-}c}}}{2\zeta_{\mathrm{c}}}} \right), \tag{3.18}$$

where the reduced-order loop gain can be extracted to be $L_{\mathrm{in}}^{\mathrm{I\text{-}RO}} = \omega_{\mathrm{n\text{-}c}}/2\zeta_{\mathrm{c}}s$. Thus, utilizing (2.4) and (3.18), the small-signal behavior of PVG power under I-type control

is dictated by

$$\hat{p}_{\text{pv}}(t) \approx I_{\text{pv}}\mathcal{L}^{-1}\left\{G_{\text{ci-c}}^{\text{I-RO}}\frac{\Delta V_{\text{pv}}^{\text{ref}}}{s}\right\} = I_{\text{pv}}\Delta V_{\text{pv}}^{\text{ref}}\left(1 - \exp(-\omega_{\text{n-c}}/2\zeta_c t)\right) \qquad (3.19a)$$

in CCR,

$$\hat{p}_{\text{pv}}(t) \approx -\frac{V_{\text{pv}}}{r_{\text{pv}}}\mathcal{L}^{-1}\left\{G_{\text{ci-c}}^{\text{I-RO}}\frac{\Delta V_{\text{pv}}^{\text{ref}}}{s}\right\} = -\frac{V_{\text{pv}}}{r_{\text{pv}}}\Delta V_{\text{pv}}^{\text{ref}}\left(1 - \exp(-\omega_{\text{n-c}}/2\zeta_c t)\right) \quad (3.19b)$$

in CVR, and

$$\hat{p}_{\text{pv}}(t) \approx -\frac{1}{R_{\text{pv}}}\mathcal{L}^{-1}\left\{G_{\text{ci-c}}^{\text{I-RO}}\frac{\Delta V_{\text{pv}}^{\text{ref}}}{s}\right\}^2 \approx -\frac{1}{R_{\text{pv}}}\Delta V_{\text{pv}}^{\text{ref}}\left(1 - 2\exp(-\omega_{\text{n-c}}/2\zeta_c t)\right)$$

$$(3.19c)$$

in CPR, when the higher order term is neglected in (3.19c). It can be concluded from (3.19) that the PVG power time constant is $\tau = 2\zeta_c\omega_{\text{n-c}}$. Thus, the settling times within $\pm\Delta$ band around the corresponding steady-state value are given by

$$T_\Delta = \frac{2\zeta_c}{\omega_{\text{n-c}}}\ln\left(\frac{1}{\Delta}\right) \qquad (3.20a)$$

in CCR and CVR, and by

$$T_\Delta = \frac{2\zeta_c}{\omega_{\text{n-c}}}\ln\left(\frac{2}{\Delta}\right) \qquad (3.20b)$$

in CPR. The closed-loop damping factor ζ_c and undamped natural frequency $\omega_{\text{n-c}}$ can be calculated from the measured crossover frequency and phase margin based on (2.31).

Figure 3.5 shows the design example of PVG-interconnected dc-dc converter under I-control. Selecting the gain margin of 10 dB, the loop gain crossover frequency is obtained as $\omega_c = 2\pi \cdot 53$ rad/s and the phase margin is PM $\approx 90°$. Since $\omega_c \ll \omega_z$, there is no need to cancel the capacitor ESR induced zero. Bode diagram of the resulting loop gains L_{in}^{I} are shown in Fig. 3.5a for all the three regions in addition to the approximated loop gain $L_{\text{in}}^{\text{I-RO}}$. Based on the measured ω_c and PM, the corresponding values of $\omega_{\text{n-c}}$ and ζ_c can be calculated to $\omega_{\text{n-c}} = 2\pi \cdot 1.27$ krad/s and $\zeta_c = 11.97$. Apparently, the

(a) Full-order and reduced order loop gains

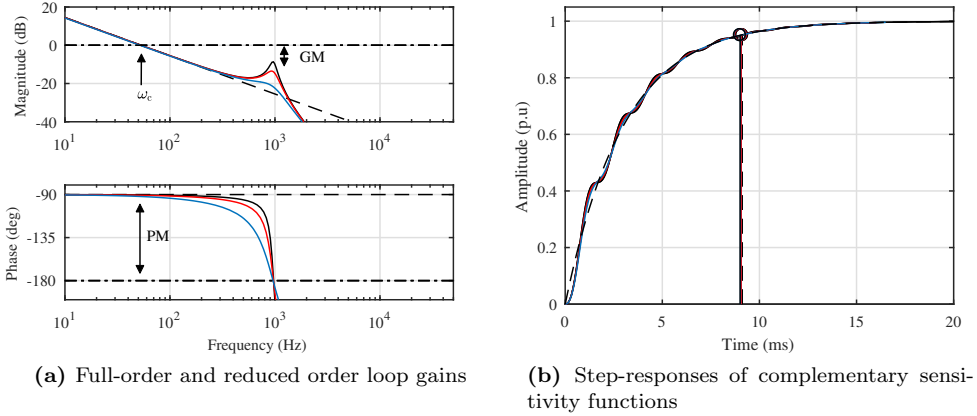(b) Step-responses of complementary sensitivity functions

Fig. 3.5: System analysis under I-control. Black line: CCR, red line: CPR, blue line: CVR and black dashed line: reduced-order model.

loop gain is well approximated by (2.26) within the control bandwidth. Figure 3.5b presents step responses of $G_{\text{ci-c}}^{\text{I}}$ and approximating function $G_{\text{ci-c}}^{\text{I-RO}}$ with $\Delta = 0.05$ (5 %) settling times indicated. It may be concluded that the differences are very small, indicating that PVG dynamic resistance has negligible influence on dynamic performance. Hence, following (3.20), PVG power settling times within 5 % band are then expected as $T_{\Delta,\text{CCR}} = T_{\Delta,\text{CVR}} \approx 9\,\text{ms}$ and $T_{\Delta,\text{CPR}} \approx 11\,\text{ms}$.

Settling-time approximation under PID-type control

For the case of the desired loop-gain crossover frequency ω_c close to or higher than the resonant frequency of the converter, a PID-type controller (2.21) is typically required. In that case, the damping factor is less than unity, and the time-domain function represents the resonant-system behavior. As discussed in (2.2.3), using inverse Laplace transformation directly to the full-order transfer function (3.17) would yield a too complex representation to calculate the corresponding envelope curves and their settling times. However, by utilizing the methods introduced in Section 2.2.3, a system can be characterized by a second-order transfer function. As a consequence, the PVG voltage transient behavior can be characterized by the reduced second-order model in (2.28) by

$$\hat{v}_{\text{pv}}(s) = G_{\text{ci-c}}^{\text{PID}} \cdot \frac{\Delta V_{\text{pv}}^{\text{ref}}}{s} \approx \frac{\omega_{\text{n-c}}^2}{s^2 + 2\zeta_c\omega_{\text{n-c}}s + \omega_{\text{n-c}}^2} \cdot \frac{\Delta V_{\text{pv}}^{\text{ref}}}{s} \qquad (3.21)$$

Thus, utilizing (2.4) and (3.18), the small-signal behavior of PVG power under PID-

type control is dictated by

$$
\begin{aligned}
\hat{p}_{\text{pv}}(t) &\approx I_{\text{pv}}\mathcal{L}^{-1}\left\{G_{\text{ci-c}}^{\text{PID-RO}}\frac{\Delta V_{\text{pv}}^{\text{ref}}}{s}\right\} \\
&= I_{\text{pv}}\Delta V_{\text{pv}}^{\text{ref}}\left(1\pm\frac{1}{\sqrt{1-\zeta_{\text{c}}^2}}\exp(-\zeta_{\text{c}}\omega_{\text{n-c}}t)\sin\theta(t)\right)
\end{aligned}
\tag{3.22a}
$$

in CCR,

$$
\begin{aligned}
\hat{p}_{\text{pv}}(t) &\approx -\frac{V_{\text{pv}}}{r_{\text{pv}}}\mathcal{L}^{-1}\left\{G_{\text{ci-c}}^{\text{PID-RO}}\frac{\Delta V_{\text{pv}}^{\text{ref}}}{s}\right\} \\
&= -\frac{V_{\text{pv}}}{r_{\text{pv}}}\Delta V_{\text{pv}}^{\text{ref}}\left(1\pm\frac{1}{\sqrt{1-\zeta_{\text{c}}^2}}\exp(-\zeta_{\text{c}}\omega_{\text{n-c}}t)\sin\theta(t)\right)
\end{aligned}
\tag{3.22b}
$$

in CVR and

$$
\begin{aligned}
\hat{p}_{\text{pv}}(t) &\approx -\frac{1}{R_{\text{pv}}}\left(L^{-1}\left\{G_{\text{ci-c}}^{\text{RO-I}}\frac{\Delta V_{\text{pv-ref}}}{s}\right\}\right)^2 \\
&\approx -\frac{\Delta V_{\text{pv}}^{\text{ref}}}{R_{\text{pv}}}\left(1\pm 2\frac{1}{\sqrt{1-\zeta_{\text{c}}^2}}\exp(-\zeta_{\text{c}}\omega_{\text{n-c}}t)\sin\theta(t)\right)
\end{aligned}
\tag{3.22c}
$$

in CPR with $\theta(t) = \omega_{\text{n-c}}\sqrt{1-\zeta_{\text{c}}^2}t + \tan^{-1}\left\{\sqrt{1-\zeta_{\text{c}}^2}/\zeta_{\text{c}}\right\}$. Moreover, the higher order term was neglected in (3.22c) similarly as in (3.7). Consequently, the settling times are determined from the corresponding power ripple envelopes. Therefore, the settling time within $\pm\Delta$ band around the corresponding steady-state value are then given by

$$
T_{\Delta}^{\text{CCR}} = T_{\Delta}^{\text{CVR}} \approx \frac{1}{\zeta_{\text{c}}\omega_{\text{n-c}}}\ln\left(\frac{1}{\Delta\sqrt{1-\zeta_{\text{c}}^2}}\right)
\tag{3.23a}
$$

CCR and CVR, and by

$$
T_{\Delta}^{\text{CPR}} \approx \frac{1}{\zeta_{\text{c}}\omega_{\text{n-c}}}\ln\left(\frac{2}{\Delta\sqrt{1-\zeta_{\text{c}}^2}}\right)
\tag{3.23b}
$$

in CPR. According to the factor of two in (3.23b), the settling time in CPR is expected to be the longest.

Figure 3.5 shows the design example of PVG-interconnected dc-dc converter under PID-control. The loop-gain crossover frequency was selected to be $2\pi \cdot 2515$ rad/s in CCR. Bode diagram of resulting loop gains L_{in}^{PID} are shown in Fig. 3.6a for all the three regions in addition to approximated loop gain L_{in}^{PID-RO}. Note that the diagrams account for $T_d = 1.5/f_s$ as total switching and sampling delay based on (2.22). As can be noticed from Fig. 3.6a, the crossover frequencies and phase margin have a slight variation due to the PVG-affected sensitivity function close to the resonant frequency. Therefore, it is recommended to calculate the corresponding average values of ω_{n-c} and ζ_c. These values are collected in Table 3.1 in different operation regions, from which the average reduced-order L_{in}^{PID-RO} is calculated in Fig. 3.6a.

Table 3.1: Calculated numerical values of the PVG-interconnected system in each region.

	CCR	CPR	CVR	average
ω_c (rad/s)	$2\pi \cdot 2515$	$2\pi \cdot 2482$	$2\pi \cdot 2356$	$2\pi \cdot 2451$
PM ($^\circ$)	33.8	36.6	45.9	38.766
ω_{n-c} (rad/s)	$2\pi \cdot 2759$	$2\pi \cdot 2785$	$2\pi \cdot 2801$	$2\pi \cdot 2782$
ζ_c	0.3051	0.3327	0.426	0.3546

Moreover, Fig. 3.6b presents the step responses of G_{ci-c}^{PID} and the approximating function G_{ci-c}^{PID-RO} with $\Delta = 0.05$ (5 %) settling times indicated. It may be concluded that the differences are insignificant, indicating that PVG dynamic resistance has minor influence on the settling time. Hence, according to (3.23), the PVG-power settling times within 5 % band are then expected as $T_\Delta^{CCR} = T_\Delta^{CVR} \approx 0.49$ ms and $T_\Delta^{CPR} \approx 0.61$ ms. The perturbation frequency shall be naturally less than the inverse of the defined settling times in (3.23) for ensuring proper operation of the MPP-tracking algorithms.

3.3   Perturbation step-size constraints

Once the perturbation frequency has been set, the perturbation step size Δx should be determined. As discussed in [18, 57, 93], to maximize the MPPT efficiency, the perturbation step size should be reduced as long as it does not violate the predictability of the algorithm. Based on (1.4), the perturbation-sign-decision process is solely determined by the derivative of two successive power measurement, any disturbance in the voltage or current measurement affect directly to the power. Thus, it was shown that the perturbative algorithms are not inherently able to distinguish the power change produced by the perturbation step change from any other external sources, which can cause power variation in PVG terminals. As a result, the perturbative algorithms can be confused and track the MPP in wrong direction as discussed in [18, 57, 93–95]. The three main factors affecting perturbation-sign-decision process are the power change ΔP_G induced by the varying irradiance, the power change ΔP_{noise} due to the uniform noise such as output

(a) Full-order and reduced-order loop gains

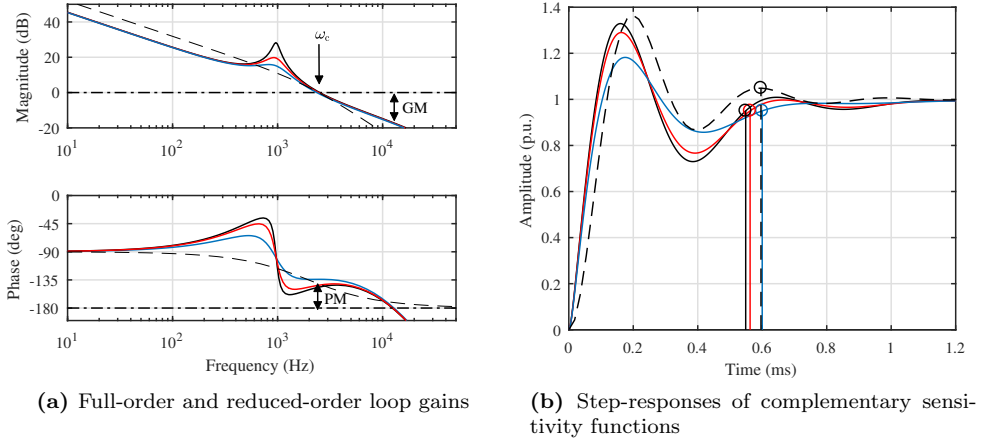(b) Step-responses of complementary sensitivity functions

Fig. 3.6: System analysis under I-control. Black line: CCR, red line: CPR, blue line: CVR and black dashed line: reduced-order model.

voltage variation or switching action, and the minimum measurable power change ΔP_{adc} due the analog-to-digital converter (ADC) quantization error. Therefore, within every perturbation period ΔT, the inequality (3.24) must be fulfilled to guarantee three-point operation (cf., Fig. 1.8).

$$|\Delta P_{\mathrm{x}}| > |\Delta P_{\mathrm{G}}| + |\Delta P_{\mathrm{noise}}| + |\Delta P_{\mathrm{adc}}|. \tag{3.24}$$

Absolute values of each factor in the right side of (3.24) should be used to take into account to the approximated maximum power variation. Each of those factors is discussed later in more detail.

Due to the nonlinear P-V curve of the PVG, the estimation of the power change induced by the voltage perturbation ΔP_{x} becomes a nontrivial task. The simplest way to approximate the PVG power variation is to use a second-order Taylor approximation (i.e., the parabolic approximation) for the P-V curve in the vicinity of the MPP as done by the authors in [56, 57, 96] given in a general form in (3.25). Thus, the knowledge of PVG internal parameters in (1.1) can be utilized to determine the factor a resulting in the power variation approximation as a function of squared voltage variation.

$$\Delta P_{\mathrm{x}} = \Delta V_{\mathrm{pv}} \Delta I_{\mathrm{pv}} \approx a(V_{\mathrm{MPP}}, I_{\mathrm{MPP}}, \eta, r_{\mathrm{s}}, r_{\mathrm{sh}} I_{\mathrm{s}}, T_{\mathrm{K}}) \cdot \Delta V_{\mathrm{pv}}^2. \tag{3.25}$$

67

For example, based on the method in [57], the characterizing factor a can be given as

$$a = H \cdot V_{\text{MPP}} + I_{\text{MPP}}/V_{\text{MPP}}, \tag{3.26}$$

where

$$H = -\frac{1}{2}\frac{\partial^2 i_{\text{pv}}}{\partial^2 v_{\text{pv}}} = -\frac{1}{2}\frac{1}{N_{\text{s}}\eta k T_{\text{K}}/q}\left(1 - \frac{r_{\text{s}}}{R_{\text{MPP}}}\right)^3 \left(\frac{I_{\text{s}}}{N_{\text{s}}\eta k T_{\text{K}}/q}\exp\left(\frac{V_{\text{MPP}} + r_{\text{s}}I_{\text{MPP}}}{N_{\text{s}}\eta k T_{\text{K}}/q}\right)\right). \tag{3.27}$$

Figure 3.7 shows ΔP_{x} as a function ΔV_{pv} extracted from the simulated Raloss SR30-36 P-V curve and parabolic estimation based on the second-order Taylor approximation (3.25). As can be concluded from the figure, the function gives a good approximation of PV power variation in vicinity of the MPP (i.e., in CPR), its average value in CCR and CVR while perturbation step size increases. Both the values of ΔP_{x} and ΔV_{pv} are scaled to their MPP values for convenience. Thus, based on this method, PVG power change induced by perturbation of the PVG voltage can be estimated in order to satisfy (3.24). Moreover, the perturbation step size must be designed in CPR, since $\Delta P_{\text{pv}}^{\text{CPR}} \ll \Delta P_{\text{pv}}^{\text{CVR}}$ and $\Delta P_{\text{pv}}^{\text{CPR}} \ll \Delta P_{\text{pv}}^{\text{CCR}}$, see (3.6).
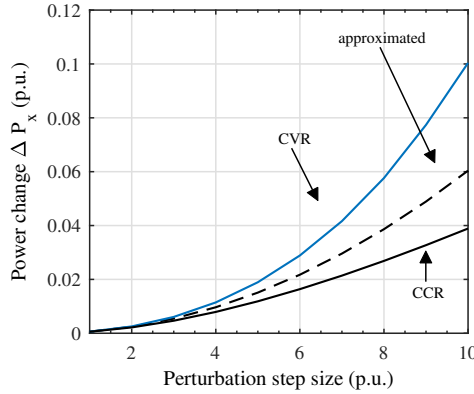

Fig. 3.7: Simulated and approximated power variations for Raloss SR30-36 PV module under low irradiance conditions, which are normalized in MPP and STC quantities.

Despite the fact that the effect of the minimum perturbation-step size is widely recognized in the literature, the upper limit also exists in a diode-switched converter as recently revealed in [59]. That is, because an open-loop and closed-loop interfacing converter may operate with relatively low damping factor, which causes oscillation during

the transients. The undamped resonant behavior introduces overshoot in converter state and output variables. In specific conditions, such an overshoot is limited by the internal behavior of the converter. That transforms the second-order system into an equivalent first-order dynamic system extending the PV-power settling time significantly, thus, reducing the power tracking performance and violating the validity of the theory to compute the power settling time in the previous studies [57, 60, 61]. The phenomenon is discussed in more detail in Section 3.3.3.

In addition to reduced MPPT efficiency, too large perturbation step size can cause power quality problems [51–54]. Recent studies have revealed that large-scale adaption of grid-connected PV inverters may be one contributor to the increasing interharmonics appearing in the grid currents, causing voltage fluctuations and light flicker as stated in [52]. One of the sources of interharmonics is related to the three-point operation of perturbative MPPT algorithms, which generates perturbation-step-size-dependent harmonic components [53]. Thus, it is not recommended to increase perturbation step size much higher than (3.25) dictates.

3.3.1 Varying irradiance conditions

The irradiance variation is considered as the main reason to confuse the operation of the perturbative MPPT algorithm. While the PVG voltage variation can be considered negligible during the irradiance transition, the photocurrent is directly proportional to the irradiance and therefore, the operating point of the PVG can vary quickly under fast-moving cloud conditions. It is worth noting that the operating-point variation is clearly dependent on the physical size of the PVG. The problem is typically more severe in the small PVGs, containing a few PV panels, where the shadow caused by moving clouds takes less time to cover a PVG than in case of large-scale PV plants. It is also observed that the characteristics of irradiance transitions due to moving clouds appears to be more linear-wise than step-wise behavior [97]. Traditionally, the validation of the perturbative MPPT-algorithms is performed with step-wise irradiance curve, which does not reveal the drift phenomenon previously demonstrated in Fig. 1.9. In 2009, a test procedure EN50530 was introduced for measuring the overall efficiency of PV systems by taking into account linear irradiance transitions [19].

It has been shown that the perturbative algorithms are sensitive to drift when the combination of step size and perturbation frequency produce too small power change ΔP_{x} compared to the power change ΔP_{G} induced by the irradiance change within the perturbation period (cf. Fig. 1.9). The phenomenon continues as long as the power change caused by perturbation is higher than the power change caused by irradiance variation within perturbation period. The power change ΔP_{G} can be assumed to be caused only by the change in the current, and therefore, the power change within time

interval ΔT can be approximated as [18]

$$\Delta P_{\mathrm{G}} \approx V_{\mathrm{pv}}\Delta I_{\mathrm{pv}} = V_{\mathrm{pv}}\frac{di_{\mathrm{pv}}}{dG}\frac{dG}{dt}\Delta T. \tag{3.28}$$

While the operating point deviates away from the MPP, the corresponding ΔP_{x} increases as can be concluded from Fig. 3.7. Therefore, the system might deviate only during a couple of additional perturbation steps until (3.24) is fulfilled restoring the normal operation of the algorithm despite the lost energy. However, in the worst case scenario, the combination of Δx and $1/\Delta T$ is designed so small that (3.24) is never fulfilled and the operation is drifted either to SC or OC condition.

As demonstrated in Section 1.2, the rate and duration of the change of irradiance transition vary a lot, which makes it problematic to choose specific values for MPPT algorithm design. The duration of the irradiance transitions can vary from a second up to several minutes, and the irradiance transitions were observed to change even 400 W/m^2 in 0.1 s. As a demonstration, the distribution of the maximum rate of change of all irradiance transitions in [98] is depicted in the Fig. 3.8 recorded from Solar Photovoltaic Power Station Research Plant of Tampere University of Technology with 10 Hz sampling rate during 50 days.
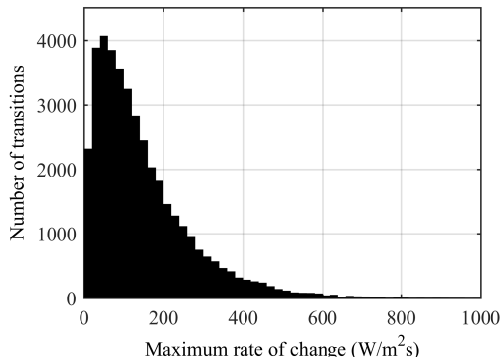

Fig. 3.8: Distribution of maximum rate of change of irradiance transitions in the specific time interval.

As can be concluded from the figure, the average of the transient speed take place around 30-50 W/m^{2}s. That matches with reported value in [20], where the usual irradiance slope is suggested as 30 W/m^{2}s and utilized in the classical stationary PV applications. However, as also stated in [18], more recent applications of PV systems, e.g., sustainable mobility, require performing the analysis with much more critical values of transition speeds. Therefore, authors in [18] suggest to using the maximum rate of

irradiance transition to be 100 W/m²s. The value is based on the maximum transition rate determined in the standard EN50530, which is the European standard for measuring the overall efficiency of PV inverters based on different irradiance profiles determining MPPT efficiency under varying irradiance conditions [19]. Perturbation period is usually designed much faster than the length of the irradiance transition and therefore, a constant value for irradiance transition speed can be used.

Despite the simplicity of power decision process with two consecutive power measurements, as a drawback, it has been shown to fail in varying irradiance conditions. Therefore, some improvements to the basic power prediction have been developed. The drift problem can be overcome by using the improved perturbative algorithm called dP-P&O developed by authors in [94]. It performs an additional measurement in the middle of the MPPT perturbation period, which is used to predict the direction of the power change. With the additional power measurement, the power change caused by the perturbation itself can be separated from the power change caused by the irradiance change. The operation of the algorithm is demonstrated in Fig. 3.9, where points A,B,C and D correspond different operating points on P-V curve.
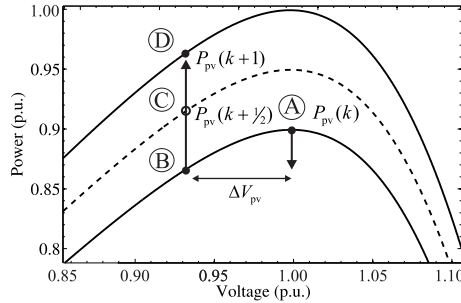

Fig. 3.9: Demonstration of dP-P&O algorithm operation in rapidly varying irradiance condition.

Let us suppose that the system is working at k-th sampling instant at point A and the operating point moves leftwards with the amount of ΔV_{pv}. If the irradiance is changing with a constant rate of speed within MPPT period, the operating point moves from A to D instead of moving from A to B. This yields $P_{\mathrm{pv}}(k) - P_{\mathrm{pv}}(k+1) < 0$ and unintentional operation of the algorithm. However, using an additional power measurement $P_{\mathrm{pv}}(k+1/2)$ in point C, the false operation of the tracker can be avoided. Assuming that the power oscillation is settled in the middle of the MPPT period in $P_{\mathrm{pv}}(k+1/2)$, the power change between C and D is solely caused by the irradiance change. Since the power change between points A and D within the whole MPPT is measured, the power change caused by the perturbation can be compared to the power change caused by the irradiance

71

change yielding the new equation for calculating the power change given in (3.29).

$$\Delta P_{\mathrm{pv}} = 2P_{\mathrm{pv}}(k+1/2) - P_{\mathrm{pv}}(k+1) - P_{\mathrm{pv}}(k). \qquad (3.29)$$

Since the additional power measurement is done in the middle of MPPT period, it requires that the power oscillation must be settled down before half of the MPPT perturbation period ΔT to guarantee correct PVG power measurements as discussed in Section 3.2. Thus, the perturbation period needs to doubled compared to the traditional case, which requires increasing Δx correspondingly.

3.3.2 The effect of different noise sources

In all MPPT algorithms based on the measurement of the electrical parameters, the noises and the measurement errors contribute to increasing the uncertainty associated to the variables involved in the MPPT, and as a consequence, the decision process can be compromised [18, 99, 100]. There are several sources of noise and uncertainty that confuse the MPPT algorithm to convergence away from MPP such as voltage and current disturbances from the downstream system, nonidealities of sensors and quantization properties of the digital systems. Modeling all the sources will be a complex task, and all the sources cannot be even estimated beforehand. Thus, by minimizing the effect of those noise sources should be carried out in hardware and signal process level. Moreover, it has been shown that enhanced signal filtering and larger perturbations are found to be effective in building the system immunity to noise [99].

In grid-connected single-phase systems, the output power of inverter fluctuates at twice the grid frequency as indicated in (3.30). This fluctuation causes double-line-frequency ripple component to the dc-link voltage in the two-stage PV inverter. When the dc-dc converter is connected to the input of the singe-phase inverter, the power fluctuation reflected to the input side of the dc-dc converter. If this voltage fluctuation passes through the dc-dc stage into the PV generator, it will decrease the energy taken from the generator or disturb the tracking of the MPP of the generator [18, 96].

$$p_{\mathrm{ac}} = v_{\mathrm{ac}}i_{\mathrm{ac}} = V\sin(\omega_{\mathrm{grid}}t)I\sin(\omega_{\mathrm{grid}}t) = VI\sin^2(\omega_{\mathrm{grid}}t) = \frac{VI}{2}(1-\cos(2\omega_{\mathrm{grid}}t)). \quad (3.30)$$

There are a lot of different solutions to prevent the output power ripple from affecting the input power, i.e., to realize the power decoupling [101, 102]. One of them is dc-link voltage feedforward, which has been used to improve the performance of dc-dc converter in two-stage conversion scheme in PV application [103]. Recent studies have indicated that such a scheme can be successfully also implemented into open-loop single-stage PV

systems [104]. However, a conventional way is to increase the dc-link capacitance between dc-dc and dc-ac conversion stages, which can also be applied to the PV generator output side. The large capacitors are usually of electrolyte type, which are known to have a limited lifetime at elevated temperatures and high ripple currents lowering the reliability of the system. Based on (3.30), the peak-to-peak value of the voltage ripple in dc-link capacitor can be approximated as given in (3.31). Thus, the amplitude of the ripple component is inversely proportional to the value of capacitance.

$$v_{\text{dc,p-p}} = \frac{P_{\text{pv}}}{2\omega_{\text{grid}}C_{\text{dc}}V_{\text{dc}}} \tag{3.31}$$

The double-line-frequency ripple component can disturb the MPP tracking process if the voltage ripple component exceeds the voltage perturbation within the perturbation period as stated in [26]. Thus, if adequate attenuation from the double-line-frequency ripple component is not carried out with passive or active methods, the perturbation step size should be increased correspondingly. The effect of output voltage ripple to PVG terminals can be estimated based on the output-voltage-to-PVG-voltage transfer function $T_{\text{oi}} = \hat{v}_{\text{pv}}/\hat{v}_{\text{o}}$. However, as can be concluded from the symbolic open-loop equation of $T_{\text{oi-o}}$ in (2.36), the magnitude of $T_{\text{oi-o}}$ at low frequencies corresponds to D', which does not provide usually sufficient attenuation at twice the grid frequency. At closed loop, however, the input-voltage feedback can improve attenuation significantly, which may satisfy the stated requirements. There are publications providing double-line frequency attenuation by input-voltage control using simple low-bandwidth I-controller [105], high bandwidth compensator [26], or high bandwidth PI controller together with quasi-resonant controller [106].

The minimum uncertainty in the voltage and current measurements can be modeled based on the resolution of the ADC [18]. In order to measure reliable PVG power change between two consecutive perturbation, the voltage perturbation needs to be large enough to produce power change in PVG terminals that ADC can measure. Thus, due to the digital implementation, the ADC has the limited number of discrete values it can produce over the range of analog values. In general, the minimum change in the voltage required to guarantee a change in the ADC output is determined by the least significant bit (LSB) voltage. If the voltage and current measurements are connected in the ADC with similar specifications (i.e., same full-scale voltage and number of bits), the both transformed signals have the voltage resolution v_{adc}, which is half of the last significant bit of the ADC [99]. Therefore, the minimum step change for ΔV_{pv} and ΔI_{pv} can be calculated by

the full-scale output voltage V_{fs} and the number of bits B in ADC as follows

$$\Delta V_{\text{pv}} > \frac{1}{G_{\text{se}}^{\text{v}}} \frac{1}{2} \frac{V_{\text{fs}}}{2^{\text{B}}} \tag{3.32a}$$

$$\Delta I_{\text{pv}} > \frac{1}{G_{\text{se}}^{\text{i}}} \frac{1}{2} \frac{V_{\text{fs}}}{2^{\text{B}}}. \tag{3.32b}$$

where G_{se}^{v} and G_{se}^{i} represent scaling factor of the current and voltage measurement (i.e., the measurement sensing gain), respectively. Since we are interested in power variation, the minimum measurable PVG power change can be calculated based on the *uncertainty propagation law* [18] yielding

$$\Delta P_{\text{ADC}} = \sqrt{v_{\text{pv}}^2 \left(\frac{v_{\text{ADC}}}{G_{\text{se}}^{\text{v}}} \right)^2 + i_{\text{pv}}^2 \left(\frac{v_{\text{ADC}}}{G_{\text{se}}^{\text{i}}} \right)^2}. \tag{3.33}$$

Equation (3.33) represents the minimum value of the power variation, which can be used as a starting point when designing perturbation step size according to (3.25).

3.3.3 The effect of discontinuous inductor current

In addition to the minimum perturbation step size, the upper limit also exists in the diode-switched converters due to their current-blocking characteristics. As discussed in Section 1.3, one of the main advantages of double-stage conversion is that larger variations in input voltage can be tolerated, and the maximum input voltage can be smaller compared to the single-stage conversion consisting only of the inverter. Other benefits of the boost topology in photovoltaic applications are that the input current is continuous and that the blocking diode is included in the power stage so that no additional diode is needed. The purpose of blocking diode is to prevent the current from flowing back to the PVG from a downstream system during the night or other times of low irradiation [70].

However, the diode introduces additional design constraints from the perturbation-step-size point of view. The open-loop and closed-loop boost-power-stage converter operating with relatively low damping factor exhibit resonant behavior in transient conditions. Such an undamped transient characteristic introduces overshoot to the control-to-output-variable transfer function, which is also visible inherently in the inductor-current transient behavior. Therefore, if the perturbation step size Δx is too large, the inductor current can move from continuous conduction mode (CCM) to discontinuous conduction mode (DCM) [59]. That transforms the second-order system into an equivalent first-order dynamic system extending the PV-power settling time significantly, thus, reducing power tracking performance and violating the validity of the theory developed for PVG-power

settling time estimation for open-loop (cf. Section 3.2.1) and closed-loop converters (cf. Section 3.2.2), which are based on the linearized model of the converter.

The phenomenon is demonstrated in Fig. 3.10, which represents simulated PV voltage, inductor current and capacitor current transient waveforms when relatively large duty-ratio step change is applied in the boost-power-stage converter. Since the diode included inherently in the power-stage (cf. Fig. 2.16), the inductor current cannot drop below zero. When the inductor current reaches zero, the capacitor current is solely determined by the constant PV current, i.e., $i_{C1} = I_{pv}$. Thus, the PV voltage starts to increase with ramp rate of I_{pv}/C_1 (cf. Fig. 3.10a) transforming the second-order system into equivalent first-order dynamic system extending the PV-voltage and finally the PV-power settling time. It is worth noting that the current saturation due to the large perturbation step size occurs especially when PV voltage is increased, which dictates from the decreased inductor current. The overshoot, i.e., the difference between the minimum (or maximum) and the steady-state value during the transient, is mainly determined by the damping factor ζ_{pv} and the perturbation step size Δx. Therefore, it is obvious that while these two values are fixed, the DCM issue is more severe in low PV current (i.e., irradiance) conditions as will be shown in the equations derived later in this section.
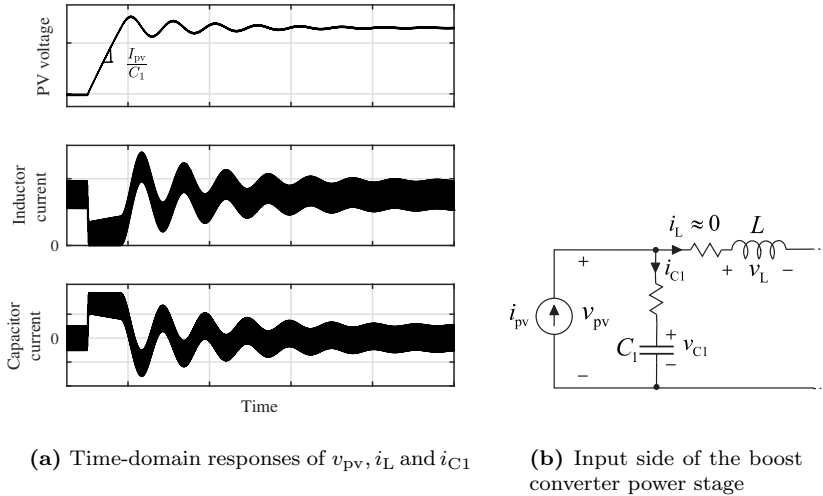

(a) Time-domain responses of v_{pv}, i_L and i_{C1}

(b) Input side of the boost converter power stage

Fig. 3.10: Illustration of the PV voltage transient response during large perturbation step size.

The following sections represent the analysis for open-loop and closed-loop operated converters to estimate the maximum perturbation step size. Based on the methods developed in the previous sections, determining the maximum overshoot of the system becomes a trivial task.

Open-loop-operated converters

The effect of the step change in duty ratio on inductor-current behavior can be studied from the open-loop control-to-inductor-current transfer function $G_{\text{cL-o}}$, which can be calculated similarly as the other output variables discussed in Section 2.2. It can be given as the function of control-to-input-voltage transfer function $G_{\text{ci-o}}$ in (3.34).

$$G_{\text{cL-o}}(s) = \frac{\hat{i}_{\text{L}}}{\hat{d}} = \frac{-C_1 s}{1 + s/\omega_{\text{z-esr}}} \cdot G_{\text{ci-o}}(s) = V_{\text{e}} C_1 \frac{\omega_{\text{n}}^2 s}{s^2 + 2\zeta_{\text{pv}}\omega_{\text{n}} s + \omega_{\cdot \text{n}}^2} \tag{3.34}$$

Thus, as (3.34) indicates, $G_{\text{cL-o}}$ with zero dc gain has the same dynamic characteristics as the $G_{\text{cL-o}}$ without the effect of capacitor induced ESR zero. The relative overshoot from the steady-state value can be studied from the second-order transfer function in (3.34) yielding descending exponential behavior as the function of damping ratio given in Fig. 3.11. Clearly, the overshoot will take place if the damping factor is less than the value of $1/\sqrt{2}$. Due to the monotonic behavior, the maximum overshoot is expected to happen at the operation region of the PVG with the lowest damping ratio, i.e., in CCR.
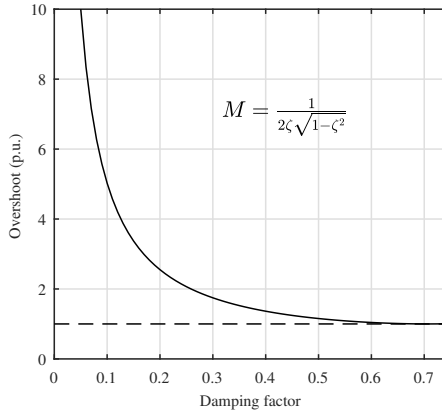
Fig. 3.11: Correlation between damping factor and overshoot.

The time-domain inductor-current step response with ΔD step change can be solved to be

$$i_{\text{L}}(t) = \mathcal{L}^{-1}\left\{G_{\text{cL-o}} \frac{\Delta D}{s}\right\} = V_{\text{e}} C_1 \left(\frac{\omega_{\text{n}}}{\sqrt{1 - \zeta_{\text{pv}}^2}} \exp\left(-\zeta_{\text{pv}}\omega_{\text{n}} t\right) \sin \theta(t)\right) \Delta D. \tag{3.35}$$

where the parameters have the same meaning as formerly defined in Section 3.2. The

critical duty-ratio step change can be solved by analyzing the time-domain equation in (3.35). The time, where $i_L(t)$ in (3.35) reaches its minimum value, can be found by solving $di_L(t)/dt = 0$. Thus, the minimum value for the unit-step response of the underdamped system occurs at

$$t_{min} = \frac{\tan^{-1}\left(\sqrt{1-\zeta_{pv}^2}/\zeta_{pv}\right)}{\omega_n\sqrt{1-\zeta_{pv}^2}}. \tag{3.36}$$

Hence, the minimum value for $i_L(t)$ due to the duty-ratio step change is

$$i_L(t_{min}) = \underbrace{V_e C_1 \omega_n \exp\left(-\frac{\zeta_{pv}}{\sqrt{1-\zeta_{pv}^2}}\tan^{-1}\left(\frac{\sqrt{1-\zeta_{pv}^2}}{\zeta_{pv}}\right)\right)}_{M_d} \Delta D. \tag{3.37}$$

To ensure continuous inductor current, the minimum inductor current after step change must be $\Delta i_L = I_{pv} - M_d \cdot \Delta d - \Delta i_{L,pp}/2 > 0$, when the inductor-current peak-to-peak ripple $\Delta i_{L,pp}$ is also taken into account. $\Delta i_{L,pp}$ is at its highest value when the input voltage is half the output voltage, i.e., $\Delta i_{L,pp} = V_o/(4Lf_s)$. Therefore, we can get the following equation for the maximum duty-ratio step size

$$\Delta D < \frac{I_{pv} - V_o/(8Lf_s)}{V_e C_1 \omega_n \exp\left(-\frac{\zeta_{pv}}{\sqrt{1-\zeta_{pv}^2}}\tan^{-1}\left(\frac{\sqrt{1-\zeta_{pv}^2}}{\zeta_{pv}}\right)\right)}. \tag{3.38}$$

It can be noticed from (3.38) that the maximum duty-ratio step size depends both on the converter parameters and the voltage and current levels at its input and output. The worst case from the duty-ratio-step-change point of view occurs at low PV current (i.e., in low irradiance condition), where I_{pv} is the smallest. Thus, the minimum irradiance with the corresponding I_{pv} need to be fixed by a designer.

Closed-loop-operated converters

In order to formulate equation for the maximum input-voltage-reference step change, the corresponding closed-loop transfer function of inductor current need to be solved (cf., (3.35)). The closed-loop reference-to-inductor-current transfer function can be calculated

based on open-loop transfer functions as follows

$$G_{\text{cL-c}} = \frac{\hat{i}_{\text{L}}}{\hat{v}_{\text{in}}^{\text{ref}}} = \frac{1}{G_{\text{se}}^{\text{v}}} \frac{L_{\text{in}}}{1 + L_{\text{in}}} \cdot \frac{G_{\text{cL-o}}}{G_{\text{ci-o}}}. \tag{3.39}$$

Within the control bandwidth, the closed-loop transfer function $(L_{\text{in}}/(1 + L_{\text{in}}))$ can be approximated by (3.40) yielding

$$\begin{aligned}
G_{\text{cL-c}}^{\text{PID-RO}} &= -\frac{1}{G_{\text{se}}^{\text{v}}} \cdot \frac{\omega_{\text{n-c}}^2}{s^2 + 2\zeta_{\text{c}}\omega_{\text{n-c}}s + \omega_{\text{n-c}}^2} \cdot \frac{-C_1 s}{1 + s/\omega_{\text{z-esr}}} \\
&\approx \frac{C_1 \omega_{\text{n-c}}^2 s}{s^2 + 2\zeta_{\text{c}}\omega_{\text{n-c}}s + \omega_{\text{n-c}}^2}, \qquad \omega_{\text{c}} \ll \omega_{\text{z-esr}}.
\end{aligned} \tag{3.40}$$

The final form in (3.40) can be obtained by the fact that the input-capacitor-related zero $\omega_{\text{z-esr}}$ is located much further from the origin than the dominant poles in (3.40) and therefore, it will not affect the transient behavior. In case of I control, the roots of the second-order denominator are well separated and (3.39) can be represented as

$$G_{\text{cL-c}}^{\text{I-RO}} = \frac{(C_1 \omega_{\text{n-c}}/2\zeta_{\text{c}})s}{s + (\omega_{\text{n-c}}/2\zeta_{\text{c}})}, \qquad 0 < \omega < \omega_{\text{c}}. \tag{3.41}$$

The time-domain transient response of i_{L} corresponds to an exponential function, where the only pole is located at $(\omega_{\text{n-c}}/2\zeta_{\text{c}})$. Thus, the overshoot does not take place in I-type controlled system. On the contrary, in case of a closed-loop underdamped system, the inductor-current-time-domain behavior can be solved from (3.40) similarly as in open loop yielding

$$i_{\text{L}}(t) = C_1 \left(\frac{\omega_{\text{n-c}}}{\sqrt{1 - \zeta_{\text{c}}^2}} \exp\left(-\zeta_{\text{c}}\omega_{\text{n-c}}t\right) \sin\left(\omega_{\text{n-c}}\sqrt{1 - \zeta_{\text{c}}^2}t\right) \right) \cdot \Delta V_{\text{pv}}^{\text{ref}}. \tag{3.42}$$

Inductor current should not reach the zero during the transient due to voltage-reference step size, i.e., $\Delta i_{\text{L}} = I_{\text{pv}} - M_{\text{v}} \cdot \Delta V_{\text{pv}}^{\text{ref}} - \Delta i_{\text{L,pp}}/2 > 0$. Therefore, the maximum voltage-reference step change, which ensures CCM operation of the converter can be given as

$$\Delta V_{\text{pv}}^{\text{ref}} < \frac{I_{\text{pv}} - V_{\text{o}}/(8Lf_{\text{s}})}{C_1 \omega_{\text{n-c}} \exp\left(-\dfrac{\zeta_{\text{c}}}{\sqrt{1 - \zeta_{\text{c}}^2}} \tan^{-1}\left(\dfrac{\sqrt{1 - \zeta_{\text{c}}^2}}{\zeta_{\text{c}}}\right)\right)}. \tag{3.43}$$

As can be seen in (3.38) and (3.43), the maximum perturbation step size is greatly depended on the damping factor of the system. In case of closed-loop system, however, the damping factor can be modified by the controller, and overshoot can be effectively reduced if necessary. Finally, the validity of (3.38) and (3.43) are verified in Section 4.4 showing a great accuracy with the developed models.

3.4 Conclusions

Despite the generic approach of the widely utilized fixed-step P&O algorithm, its design parameters are not generic. In order to maximize the energy yield from a source and to ensure proper operation of the algorithm, it needs to be designed in each application separately. Thus, its parameters – perturbation frequency and step size – need to be optimized for the specific application by taking into account the dynamic behavior of the interfacing converter and the changes in atmospheric conditions.

Perturbation-frequency design plays an important role in direct MPPT algorithms for ensuring proper operation of the MPP tracker. During the MPPT process, the operating point may reside in any of the three regions even under constant atmospheric conditions. In open-loop-operated PV systems, the longest settling time will take place in the constant current region, where the damping of the combined system is the lowest. Consequently, unlike stated in the popular design guidelines, the perturbation-frequency design of direct MPPT algorithms must be accomplished for the worst-case operating point expected to lie in the constant current region rather than at maximum power point, as proposed by the existing design guidelines. The investigations show clearly that the perturbation-frequency design can be performed based on the dynamic behavior of the interfacing converter solely when the operating point lies in the constant current region.

The perturbation-frequency design rules for the duty-ratio-operated MPP-tracking converters are well developed and published earlier, with the exception mentioned earlier, but the similar design rules for the input-voltage-feedback-controlled MPP-tracking processes are still missing. The chapter introduced a method to estimate the transient behavior of the input-voltage-feedback-controlled MPP-tracking converter based on the crossover frequency and phase margin of the feedback loop. The method is well known in control engineering but not applied earlier in power electronics for the named application. It was shown that the method produces quite accurate predictions of the transient behavior of the PV power. In case of the duty-ratio-operated MPP-tracking converter, the PV-power transient is highly dependent on the PV-generator operating point but not anymore when the input-voltage feedback control is used. Consequently, the settling time is longest when the operating point resides in constant-power region. Therefore, it is recommended to use the constant-power-region-related equations to compute the

settling time required for perturbation-frequency determination in case of multi-loop MPPT structures, employing inner input-voltage loop. In addition, the settling time can be estimated accurately by means of the crossover frequency and phase margin of the input-voltage feedback loop only.

In addition to minimum perturbation step size constraints, it has been shown that diode-switched dc-dc converter introduces the maximum value for perturbation step size due to discontinuous inductor current during transients. That is because the open-loop and closed-loop boost-power-stage converter operating with relatively low damping factor exhibit resonant behavior in transient conditions. Such an undamped transient characteristic introduces overshoot to the control-to-output-variable transfer function, which is also visible inherently in the inductor-current transient behavior. Therefore, if the perturbation step size Δx is too large, the inductor current can move from continuous conduction mode (CCM) to discontinuous conduction mode (DCM). That transforms the second-order system into an equivalent first-order dynamic system extending the PV-power settling time significantly, thus, reducing power tracking performance and violating the validity of the linear theory developed for PVG-power settling time estimation for open-loop and closed-loop converters.

4 EXPERIMENTAL VERIFICATION

4.1 Experimental setup

In order to validate the analytical findings listed in Section 1.5, the experimental setup shown in Figs. 4.1 and B.1 was based on the prior research in [105] and utilized during the experiments. The low-power MPPT boost converter was supplied by a single Raloss SR30-36 PV module, which is composed of 36 series-connected monocrystalline silicon cells. The PV module was illuminated by fluorescent lamps, which can produce maximum irradiance of about 500 W/m^2 yielding short-circuit current of 1.0 A and open-circuit voltage of 19.2 V at module temperature of 45 °C. The panel was utilized in the previous research, and further information can be found from [73]. At the time of the research, also the Agilent PV emulator was available. However, the common problem with PV emulators is the large output capacitance, which will dominate the input capacitance of the converter, thus dampening the true behavior of the PV-interconnected system. Therefore, the real PV panel was utilized in the study to reveal the true dynamics of the interconnected PV system.
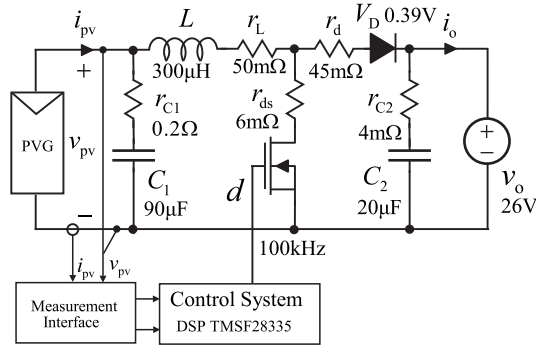
Fig. 4.1: Schematic representation of the experimental boost converter.

The PV module is connected to the boost-power-stage prototype controlled by the digital signal processor (DSP). Voltage and current measurements were low-pass-filtered with the cut-off frequency of 50 kHz in order to prevent the noise from the converter switching actions to deteriorate the measurements. Finally, the output of the converter

is connected to the 26-V battery in parallel with Chroma 63103A current sink to main-tain constant battery voltage. Frequency responses were obtained by Venable Model 3120 frequency-response analyzer without any post-processing. Time-domain responses were post-processed by normalization only, i.e., the original data were divided by the corresponding final values for improving the visibility of the information. In addition, it is worth noting that time-domain measurements in Sections 4.2 and 4.3 are represented without the switching ripple in the corresponding quantities to clarify the information of transient settling processes.

4.2   Open-loop settling time estimation

During the experiments, PVG-power-transient behavior was analyzed in the three sub-sequent operating points: $(I_{pv}, V_{pv}) = (1\ A, 10\ V)$ in CCR, $(I_{pv}, V_{pv}) = (0.91\ A, 16\ V)$ in CPR and $(I_{pv}, V_{pv}) = (0.61\ A, 18\ V)$ in CVR. Corresponding values of the PVG dynamic resistance at the above operating points were measured as follows: $r_{pv} = 285\ \Omega$ in CCR, $r_{pv} = 17.4\ \Omega$ in CPR and $r_{pv} = 3.8\ \Omega$ in CVR. Fig. 4.2 presents the measured PVG power, voltage and current responses in different operation regions to a step change in duty ratio. All the quantities are normalized to their steady-state values in order to highlight the behavior of different variables during the transients.
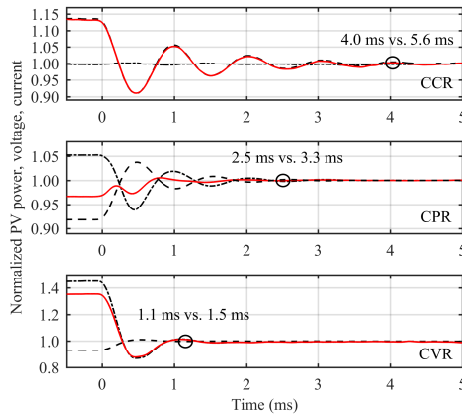

Fig. 4.2: Measured system responses of PVG voltage (dashed), current (dot-dashed line), and power (solid line) induced by a step change in the duty ratio.

Fig. 4.2 explicitly demonstrates that the measured PVG-power-transient behavior matches the analysis carried out in Section 4.2 based on the behavior of r_{pv} in different operational regions. In CCR, the settling of the PVG power transient follows that of the PVG voltage and its duration is longest among different regions. In CPR, the PVG power transient is minimized due to the opposite settling behaviors of the PV voltage

and current. In CVR, the PVG power transient settling behavior follows that of the PVG current, which is also much more damped compared to the settling behavior in CCR.

According to the component values in Fig. 4.1, the values of r_{pv} stated above and the definition given in (3.12), damping factor is 0.0883 in CCR, 0.1925 at MPP, and 0.3286 in CVR while the undamped natural frequency is $\omega_n \approx 6.08 \cdot 10^3$ rad/s. Hence, the settling times are analytically obtained as 5.6 ms in CCR, 3.3 ms in CPR and 1.5 ms in CVR for $\Delta = 0.05$. The actual settling times represented in the figure are slightly lower because of un-modeled parasitic circuit resistances (i.e., actual dampings are higher than the predicted ones); nevertheless the fact that the CCR settling time is the longest among the three regions is well evident.

Once the perturbation frequency has been set, the perturbation step size should be determined. The P&O algorithm can be confused and track the MPP in wrong direction when power variation caused by irradiation change (ΔP_G) is larger than that (ΔP_v) induced during MPPT algorithm perturbation interval. Based on the second-order Taylor approximation for the P-V curve in (3.25)-(3.27) in vicinity of the MPP, one can estimate the smallest duty cycle perturbation ΔD, satisfying (3.24). In the estimation, the following parameters are used: material constant $K_{ph} = di_{ph}/dG = 1.9$ mA, saturation current $I_s = 1.097 \cdot 10^{-10}$ A, and ideality factor $\eta = 1.0$. These parameters yield $\Delta D = 0.0178$, producing power variation capable to overcome that caused by the irradiation ramp of 100 W/m^{2}s within the interval of 5.6 ms. Nevertheless, in addition to the irradiation variations, the finite resolution of utilized analog-digital converter (ADC) should also be taken into account. Texas Instruments' TMS320F28335 DSP utilizes 12-bit ADC with 3-V full-scale voltage range (i.e., ADC resolution is 0.37 mV). Taking into account the ADC quantization error according to (3.33), the minimum duty-ratio-perturbation step size will become $\Delta D_{min} = 0.0206$.

Fig. 4.3 presents the measured waveforms of the steady-state MPP-tracking process, utilizing the above-calculated perturbation frequency and duty-ratio step size (i.e., 1/5.6 kHz and 0.0206, respectively). The behavior of the PVG power, voltage, and current demonstrates that the operating point oscillates from region to region (rather than resting) even under non-varying atmospheric conditions. The settling behavior of PVG power depends on the operating point location, as predicted. Therefore, the perturbation frequency design should be accomplished assuming the worst case CCR operating point to ensure the correct operation of direct MPPT algorithms.
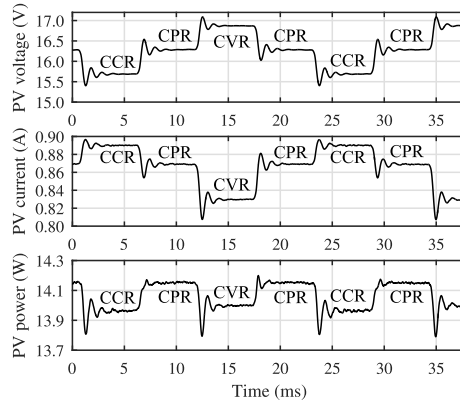
Fig. 4.3: Measured PVG voltage, current, and power during the steady-state MPPT process under non-varying atmospheric conditions.

4.3 Closed-loop settling-time estimation

The following Sections 4.3.1 and 4.3.2 focus on verification of closed-loop PVG power settling time estimation based on theoretical analysis in Section 3.2.2. The PVG-interfacing converter is controlled both I-type and PID-type controllers, and measured system responses were compared to the analytically obtained counterparts.

4.3.1 I-type control

The Bode plots of the measured loop gain L_{in} and complementary sensitivity function G_{ci-c} are shown in Fig. 4.4 corresponding to the case, where I control is used, and the crossover frequency is designed to be lower than the resonant frequency. Figure 4.4a shows the measured PV-generator-affected input-voltage-feedback loop gains in case of I controller, where the effect of the PV generator is clearly visible around the internal resonant frequency of the power stage. The crossover frequencies and PMs of converter under I control (Fig. 4.4) are as follows: CCR: 54 Hz, 89.6°, CPR: 52.3 Hz, 89.2°, and CVR: 50.5 Hz, 89.0°, respectively. The figure also shows that the PV-generator effect on the low-crossover feedback-loop gain is insignificant, and therefore, the crossover frequencies and PMs will stay practically as 50 Hz and 89.0 degrees.

The measured frequency responses, in Fig. 4.4, clearly show that the effect of the PVG resistance is insignificant on the dynamics of the converter as discussed earlier. Fig. 4.5 presents the measured PVG voltage, current, and power responses to a step change in the PVG-voltage reference in the three operating regions under I-control. The results validate the first-order transient behavior. Moreover, the power behavior satisfies (3.19) precisely: in CCR, it follows the settling behavior of PVG voltage; in CVR, it correlates
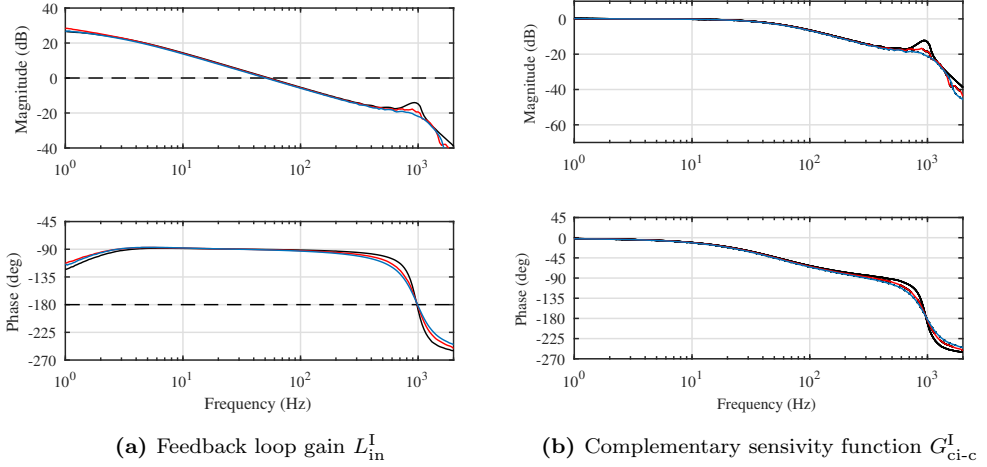
(a) Feedback loop gain L_{in}^{I}

(b) Complementary sensivity function $G_{ci\text{-}c}^{I}$

Fig. 4.4: Measured system responses under I-control in all three operation regions (black line: CCR, red line: CPR and blue line: CVR)
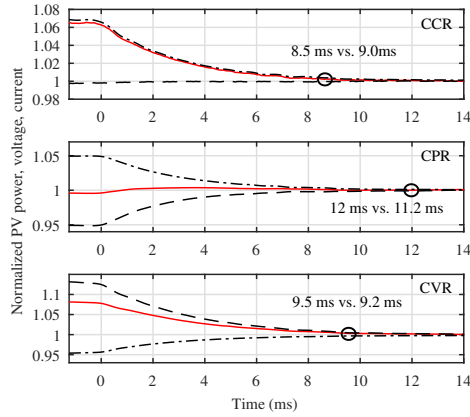

Fig. 4.5: Measured system responses of PVG voltage (dashed), current (dot-dashed line), and power (solid line) to a PVG voltage reference step change under I-type control.

with the settling behavior of the PVG current; in CPR, the PVG power transient is very small, since the PVG voltage and current transients tend to cancel each other. Moreover, the measured and predicted settling times are also given in the figure based on (3.20), where the first settling time corresponds to the measured value and the last one to the predicted value. The accuracy of the predictions and measured values are good enough to provide a tool for practical usage.

4.3.2 PID-type control

Figure 4.6 shows the measured PV-generator-affected input-voltage-feedback loop gains $L_{\text{in}}^{\text{PID}}$ and the complementarity sensitivity functions $G_{\text{ci-c}}^{\text{PID}}$ in case of PID controller, where the effect of PV generator is clearly visible around the internal resonant frequency of the power stage. The crossover frequency of the feedback loop, in Fig. 4.6a, is approximately 3 kHz. The corresponding phase behaviors indicate that the phase margin will vary slightly along the changes in the PV-generator operating point (i.e., CCR: 37 degrees, CPR: 41 degrees, and CVR: 45 degrees), which means that the system time constant will also vary accordingly.
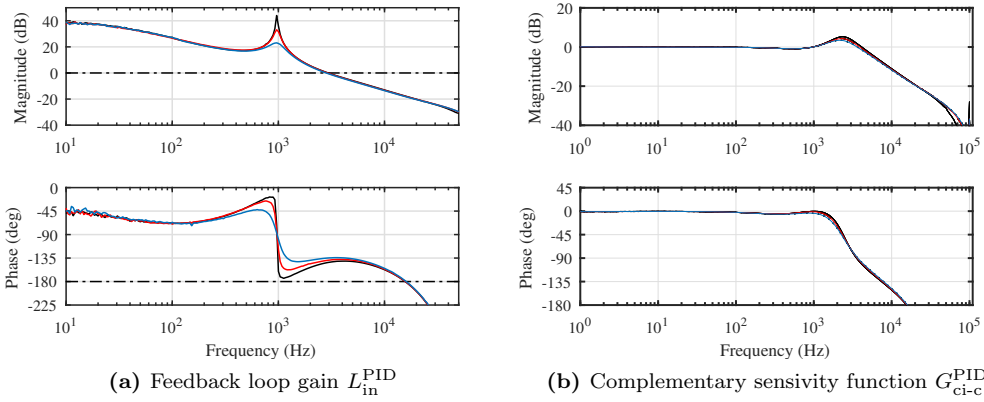

(a) Feedback loop gain $L_{\text{in}}^{\text{PID}}$ **(b)** Complementary sensivity function $G_{\text{ci-c}}^{\text{PID}}$

Fig. 4.6: Measured system responses under PID-control in all three operation regions (black line: CCR, red line: CPR and blue line: CVR)

Fig. 4.7 presents the measured PVG voltage, current, and power responses to a step change in PVG-voltage reference in the three operating regions under PID-control. The results validate the second-order transient behavior, which fits the performance predicted by (2.4). In order to validate the PVG-power-settling times, required for the perturbation frequency selection, Fig. 4.7 presents the zoomed PVG-power responses to a step change in the PVG-voltage reference in the three regions with 5 % settling time marks. As indicated, the settling times under PID-control are 0.55 ms, 0.45 ms and 0.6 ms in CCR, CVR and CPR, respectively. The predicted settling times are also given in the figure based on (3.23), where the first settling time corresponds to the measured value and the last one to the predicted value. The above experimental measurements show that the earlier given theoretical equations will quite accurately predict the PVG-power settling times. Moreover, the settling time is the longest in CPR for both of the cases under input-voltage feedback control. It is important to emphasize that this is the consequence of additional factor of 2 in the natural logarithm of (3.20b) and (3.23b) rather than the
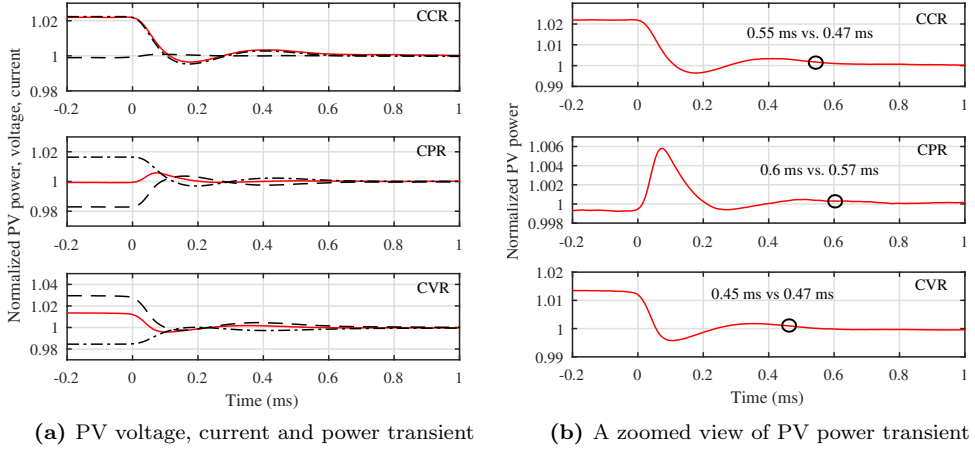
(a) PV voltage, current and power transient

(b) A zoomed view of PV power transient

Fig. 4.7: Measured system step responses of PVG voltage (dashed), current (dot-dashed line), and power (solid line) to a PVG voltage reference step change under PID-type control.

consequence of the PVG dynamic resistance.

4.4 Maximum perturbation-step size based on discontinuous inductor current

Fig. 4.8 shows the PV voltage and inductor-current transient responses under three different duty-ratio step changes. Based on the power-stage components given in Fig. 4.1, the undamped natural frequency and damping factor can be calculated to be $6.086 \cdot 10^3$ rad/s and 0.076, respectively. Thus, according to (3.38), the maximum duty-ratio step change can be calculated to be 0.075, which corresponds to 1 V PV-voltage step change. Two other measured step responses are carried out by using half and double of the critical step changes to highlight the effect of choosing too large duty-ratio step size. As can be seen from Fig. 4.8 and predicted in the earlier analysis, the transient response of the PV voltage has similar settling time as long as the duty-ratio step change is lower than the critical step change. Moreover, Equation (3.38) gives a good approximation for the inductor current peak value. In contrast, it can be seen that the inductor current is discontinuous, thus, increasing the settling time of PV voltage and PV power. For example, based on Fig. 4.8, the delay appears to be around 0.3 ms compared to the CCM case.

In the closed-loop measurements, the PID-controlled system described in the previous section was utilized. The measured loop-gain transfer functions with PID controller can be seen in [60] providing more detailed information of the system. Thus, the average
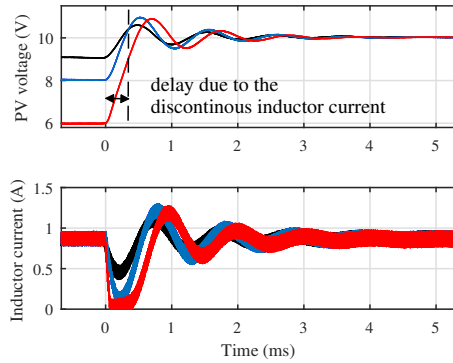
Fig. 4.8: The measured open-loop step responses of the PV voltage and inductor current when duty-ratio step changes of 0.037 (black line), 0.075 (blue line) and 0.150 (red line) are applied.

crossover frequency and phase margin are $2\pi \cdot 2950$ rad/s and $35°$, respectively. Therefore, the PID-controlled closed-loop undamped natural frequency and damping factor can be calculated to be $\omega_{\text{n-c}} = 2\pi \cdot 3263$ rad/s and $\zeta_c = 0.32$, obtained using (2.31). Thus, according to (3.43), the maximum-voltage-reference step change can be calculated to be 0.71 V. Fig. 4.9 shows the closed-loop step responses when 0.5 V, 0.71 V and 3 V PV-voltage-reference step changes are applied. The figure clearly indicates that too large perturbation step size causes delay in PV voltage transient response, thus, extending the settling time process since (3.43) is not fulfilled.
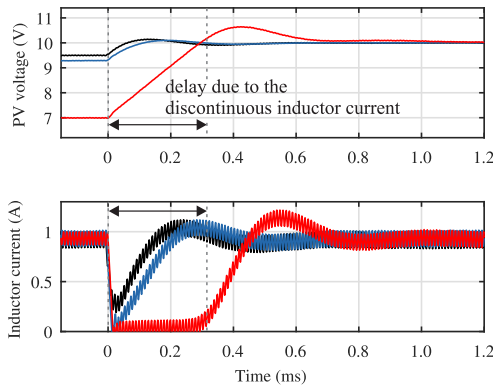

Fig. 4.9: The PV voltage and inductor-current step responses under PID control when 0.5 V (black line), 0.71 V (blue line) and 3 V (red line) reference-voltage step changes are applied).

Finally, Fig. 4.10 shows the PV voltage and inductor-current step responses with I control. Gain of the integral controller is set to 6.3 yielding crossover frequency and PM to be $2\pi \cdot 28.6$ rad/s and $89.8°$, respectively. With these values sufficient gain margin of

15 dB is achieved. Based on (2.31), the natural frequency and damping factor can be calculated to be $\omega_{\text{n-c}} = 2\pi \cdot 484$ rad/s and $\zeta_c = 8.46$. According to the earlier analyses, the transient response will be overdamped as Fig. 4.10 also shows, the inductor current does not show any overshoot or saturation. Therefore, the predicted settling time ($T_\Delta^{\text{I}} = 16.6$ ms) based on (3.20) matches well with the experiments.
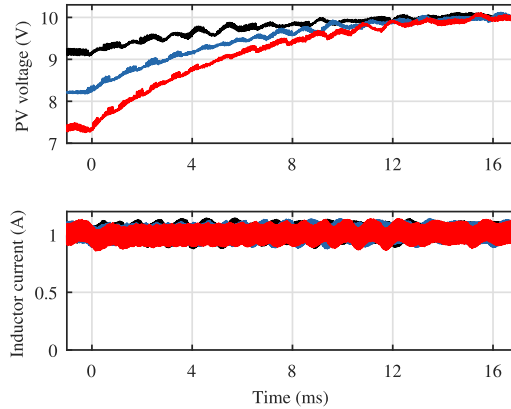

Fig. 4.10: The PV voltage and inductor-current step responses under I control when 0.9 V (black line), 1.8 V (blue line) and 2.7 V (red line) reference-voltage step changes are applied.

5 CONCLUSIONS

This chapter provides the final concluding discussions on the thesis. In addition, a brief discussion on the future topics related to the subject of the thesis is given.

5.1 Final conclusions

The I-V curve of the PV generator is usually split into constant current and constant voltage regions, separated by the maximum power point. Detailed analysis of the shape of the photovoltaic-generator's P-V curve and power-transient behavior revealed that the exact maximum power point does not exist in practice due to the finite resolution of measuring facility. Instead, the steady-state operating point may reside within a region around the MPP, which is named as constant-power region. Moreover, during the MPPT process, the operating point may reside in any of the three regions even under constant atmospheric conditions. The PVG power has a distinct characteristics in each region determined by relation between dynamic and static resistances of a PVG, which need to be considered in MPPT design process.

Thus, in order to ensure the maximization of the power extracted from the PV source, the interfacing power converter must be capable of controlling its parameters, i.e., changing its input voltage and current levels based on the MPP of the PVG. This can be done by implementing an MPPT controller, which generates the reference control signal for an interfacing converter. Regardless of the way of implementation, the fundamental operation is relatively simple: To find the electrical operating point, i.e., the voltage and current, at which the PV module generates maximum power at every time instant.

Despite the generic approach of widely utilized fixed-step P&O algorithm, its design parameters are not generic. In order to maximize the energy yield from a source and to ensure the proper operation of algorithm, the algorithm needs to be designed in each application separately. Thus, its parameters – perturbation step size and frequency – need to be optimized for the specific application by taking into account the dynamic behavior of the interfacing converter and the changes in atmospheric conditions.

MPPT efficiency is inversely proportional to the perturbation step size. Thus, to maximize the MPPT efficiency, the step size should be reduced as long as it does not violate the proper operation of the algorithm. Since the perturbation-sign-decision process is solely determined by the derivative of two successive power measurements, any

disturbance in the voltage or current measurement directly affects also the PVG power. Therefore, the perturbative MPPT algorithms are not inherently able to distinguish the power change produced by the perturbation itself from any other external source, which can cause power variation in PVG terminals. As a consequence, the perturbative algorithms can be confused and deviate from the MPP. The three main factors affecting the perturbation-sign-decision process are the power change induced by irradiance variation, the uniform noise sources and the quantization error of the ADC. Thus, the effect on each of those factors on the PVG power should be evaluated and the perturbation step size should be increased accordingly.

Perturbation-frequency design plays an essential role in direct MPPT algorithms, for ensuring the proper operation of the MPP-tracker. During MPPT process, the operating point may reside in any of the three regions with three different PVG-power-settling processes. In open-loop-operated PV systems, the longest settling time was revealed to take place in the constant current region, where the damping of the combined system is the lowest. Consequently, unlike stated in the design guidelines utilized so far, the perturbation-frequency design of the direct MPPT algorithms must be accomplished based on the worst-case operating point in the constant-current region rather than at the MPP, as proposed by the existing design guidelines. Because the PVG dynamic resistance is rather high in the constant-current region, its effect on the interfacing-converter dynamics is small. As a consequence of this, the perturbation-frequency design can be performed based on the dynamic behavior of the interfacing converter.

The perturbation-frequency design rules for the duty-ratio-operated MPP-tracking converters are well developed and published earlier, with the exception mentioned earlier, but the similar design rules for the input-voltage-feedback-controlled MPP-tracking processes are still missing. The study introduced a method to estimate the transient behavior of the input-voltage-feedback-controlled MPP-tracking converter based on the crossover frequency and phase margin of the feedback loop. The method is well known in control engineering but not applied earlier in power electronics for the named application. It was shown that the method produces quite accurate predictions of the transient behavior of the PV power. In case of the duty-ratio-operated MPP-tracking converter, the PV-power transient is highly dependent on the PV-generator operating point but not anymore when the input-voltage feedback control is used. Consequently, the settling time is longest when the operating point resides in constant-power region. Therefore, it is recommended to use the constant-power-region-related equations to compute the settling time required for the perturbation-frequency determination in case of multi-loop MPPT structures, employing inner input-voltage loop. In addition, the settling time can be estimated accurately by means of the crossover frequency and phase margin of the input-voltage feedback loop only providing a valuable tool for determining the settling

time of a transient response.

Analytical methods were also proposed to model the transient behavior of the PVG-interfacing converter based on the crossover frequency and phase margin of the feedback loop. It was concluded that closed-loop control-to-input-voltage transfer functions of I-control and PID-control equipped converter can be reduced to first-order and second-order transfer functions, respectively. That enables to approximate the PV power transient analytically, which reveals the factors affecting the transient behavior similarly as in the open-loop-operated converter, and provides valuable tools for determining the settling time of a transient response.

5.2 Future research topics

The following research topics provide an interesting continuation for the research presented in this thesis

- As it was shown, estimating the PV power transient of PVG-interconnected dc-dc converters is straightforward with the proper analytical methods. However, the similar methods do not exist for single-stage PV inverters, which are still widely used in the industry but are known to have much complex dynamics compared to the dc-dc converters. Thus, it would be valuable to develop similar transient settling time guidelines for PV inverters as well.

- Passive component sizing of converters, i.e., designing the values for inductance and capacitance in photovoltaic applications is very poorly treated in the open literature. Some suggestions have been made by authors in [107], but the rest of publications in the concerned area suggest designing the inductor and capacitor based on the maximum voltage and current-ripple value, similarly as in the conventional voltage-fed applications. Generally, the maximum current ripple is limited to 20% to 40% of the steady-state value, whereas input capacitor is designed to be large enough to attenuate the input-voltage ripple caused by the output-voltage variations. In the photovoltaic applications, which does not take into account the other important factors such as MPPT efficiency and the effect on the inductance and capacitance values on the step size of the perturbation process. Thus, it would be valuable to include the power-stage-component sizing in the MPPT-design process as well.

REFERENCES

[1] B. Bose, "Global warming: energy, environmental pollution, and the impact of power electronics," *IEEE Ind. Electron. Mag.*, vol. 4, no. 1, pp. 6–17, Mar. 2010.

[2] International Energy Agency, "Key world energy statistics," 2018. [Online]. Available: https://www.iea.org/publications/freepublications/publication/KeyWorld2017.pdf [Date accessed: 1.3.2018].

[3] S. Kouro, J. I. Leon, D. Vinnikov, and L. G. Franquelo, "Grid-connected photovoltaic systems: an overview of recent research and emerging pv converter technology," *IEEE Ind. Electron. Mag.*, vol. 9, no. 1, pp. 47–61, Mar. 2015.

[4] G. Kopp and J. L. Lean, "A new, lower value of total solar irradiance: evidence and climate significance," *Geophys. Res. Lett.*, vol. 38, no. 1, Jan. 2011.

[5] W. Hermann, "Quantifying global exergy resources," *Energy*, vol. 31, no. 12, pp. 1685–1702, Sep. 2006.

[6] D. M. Chapin, C. S. Fuller, and G. L. Pearson, "A new silicon p-n junction photocell for converting solar radiation into electrical power," *J. Appl. Phys.*, vol. 25, no. 5, pp. 676–677, May 1954.

[7] International Energy Agency, "Trends in photovoltaic applications," 2017. [Online]. Available: http://www.iea-pvps.org/fileadmin/dam/public/report/statistics/IEA-PVPS_Trends_2017_in_Photovoltaic_Applications.pdf [Date accessed: 1.3.2018].

[8] SolarPower Europe, "Global market outlook for solar power 2017-2021," Tech. Rep., 2017.

[9] F. Blaabjerg, Z. Chen, and S. Kjær, "Power electronics as efficient interface in dispersed power generation systems," *IEEE Trans. Power Electron.*, vol. 19, no. 5, pp. 1184–1194, Sep. 2004.

[10] H. Häberlin, *Photovoltaics: system design and practice.* Chichester, UK: John Wiley & Sons, Ltd, 2012.

[11] G. Petrone, C. A. Ramos-Paja, and G. Spagnuolo, *Photovoltaic sources modeling.* Chichester, UK: John Wiley & Sons, Ltd, Feb. 2017.

[12] P.-H. Huang, W. Xiao, J. C.-H. Peng, and J. L. Kirtley, "Comprehensive parameterization of solar cell: improved accuracy with simulation efficiency," *IEEE Trans. Ind. Electron.*, vol. 63, no. 3, pp. 1549–1560, Mar. 2016.

[13] M. Villalva, J. Gazoli, and E. Filho, "Comprehensive approach to modeling and simulation of photovoltaic arrays," *IEEE Trans. Power Electron.*, vol. 24, no. 5, pp. 1198–1208, May 2009.

[14] A. Chatterjee, A. Keyhani, and D. Kapoor, "Identification of photovoltaic source models," *IEEE Trans. Energy Convers.*, vol. 26, no. 3, pp. 883–889, Sep. 2011.

[15] Y. Mahmoud and E. F. El-Saadany, "A photovoltaic model with reduced computational time," *IEEE Trans. Ind. Electron.*, pp. 1–1, 2014.

[16] E. I. Batzelis and S. A. Papathanassiou, "A method for the analytical extraction of the single-diode PV model parameters," *IEEE Trans. Sustain. Energy*, vol. 7, no. 2, pp. 504–512, Apr. 2016.

[17] J. Wyatt and L. Chua, "Nonlinear resistive maximum power theorem, with solar cell application," *IEEE Trans. Circuits Syst.*, vol. 30, no. 11, pp. 824–828, Nov. 1983.

[18] N. Femia, G. Petrone, G. Spagnuolo, and M. Vitelli, *Power electronics and control techniques for maximum energy harvesting in photovoltaic systems.* CRC Press, 2012.

[19] H. Häberlin and P. Schaerf, "New procedure for measuring dynamic mpp-tracking efficiency at grid-connected pv inverters," in *24th EU PV Conf., Hamburg, Ger.*, no. September, 2009, pp. 21–25.

[20] B. Bletterie, R. Bruendlinger, and S. Spielauer, "Quantifying dynamic mppt performance under realistic conditions first test results - the way forward," in *Proc. 21st Eur. Photovolt. Sol. Energy Conf. Exhib.*, 2006, pp. 2347–2351.

[21] S. Eftekharnejad, V. Vittal, Heydt, B. Keel, and J. Loehr, "Impact of increased penetration of photovoltaic generation on power systems," *IEEE Trans. Power Syst.*, vol. 28, no. 2, pp. 893–901, May 2013.

[22] A. Mäki, S. Valkealahti, and J. Leppäaho, "Operation of series-connected silicon-based photovoltaic modules under partial shading conditions," *Prog. Photovoltaics Res. Appl.*, vol. 20, no. 3, pp. 298–309, May 2012.

[23] S. Kjær, J. Pedersen, and F. Blaabjerg, "A review of single-phase grid-connected inverters for photovoltaic modules," *IEEE Trans. Ind. Appl.*, vol. 41, no. 5, pp. 1292–1306, Sep. 2005.

[24] D. Picault, B. Raison, and S. Bacha, "Guidelines for evaluating grid connected PV system topologies," in *2009 IEEE Int. Conf. Ind. Technol.* IEEE, Feb. 2009, pp. 1–5.

[25] C. R. Sullivan, J. Awerbuch, and A. M. Latham, "Decrease in photovoltaic power output from ripple: Simple general calculation and effect of partial shading," in *2011 Twenty-Sixth Annu. IEEE Appl. Power Electron. Conf. Expo.* IEEE, Mar. 2011, pp. 1954–1960.

[26] N. Femia, G. Petrone, G. Spagnuolo, and M. Vitelli, "A technique for improving P&O MPPT performances of double-stage grid-connected photovoltaic systems," *IEEE Trans. Ind. Electron.*, vol. 56, no. 11, pp. 4473–4482, Nov. 2009.

[27] E. Romero-Cadaval, G. Spagnuolo, L. G. Franquelo, C. A. Ramos-Paja, T. Suntio, and W. M. Xiao, "Grid-connected photovoltaic generation plants: components and operation," *IEEE Ind. Electron. Mag.*, vol. 7, no. 3, pp. 6–20, Sep. 2013.

[28] A. Sangwongwanich, Y. Yang, and F. Blaabjerg, "High-performance constant power generation in grid-connected pv systems," *IEEE Trans. Power Electron.*, vol. 31, no. 3, pp. 1822–1825, Mar. 2016.

[29] Y. Yang, H. Wang, F. Blaabjerg, and T. Kerekes, "A hybrid power control concept for PV inverters with reduced thermal loading," *IEEE Trans. Power Electron.*, vol. 29, no. 12, pp. 6271–6275, Dec. 2014.

[30] M. Kasper, D. Bortis, and J. W. Kolar, "Classification and comparative evaluation of PV panel-integrated DC-DC converter concepts," *IEEE Trans. Power Electron.*, vol. 29, no. 5, pp. 2511–2526, May 2014.

[31] D. Shmilovitz and Y. Levron, "Distributed maximum power point tracking in photovoltaic systems - emerging architectures and control methods," *Autom. - J. Control. Meas. Electron. Comput. Commun.*, vol. 53, no. 2, 2012.

[32] T. Shimizu, M. Hirakata, T. Kamezawa, and H. Watanabe, "Generation control circuit for photovoltaic modules," *IEEE Trans. Power Electron.*, vol. 16, no. 3, pp. 293–300, May 2001.

[33] G. Walker and P. Sernia, "Cascaded dc-dc converter connection of photovoltaic modules," *IEEE Trans. Power Electron.*, vol. 19, no. 4, pp. 1130–1139, Jul. 2004.

[34] A. Urtasun, P. Sanchis, and L. Marroyo, "Limiting the power generated by a photovoltaic system," in *10th Int. Multi-Conferences Syst. Signals Devices 2013.* IEEE, Mar. 2013, pp. 1–6.

[35] Y. Ueda, K. Kurokawa, T. Tanabe, K. Kitamura, and H. Sugihara, "Analysis results of output power loss due to the grid voltage rise in grid-connected photovoltaic power generation systems," *IEEE Trans. Ind. Electron.*, vol. 55, no. 7, pp. 2744–2751, Jul. 2008.

[36] S. Adhikari and F. Li, "Coordinated V-f and P-Q control of solar photovoltaic generators with MPPT and battery storage in microgrids," *IEEE Trans. Smart Grid*, vol. 5, no. 3, pp. 1270–1281, May 2014.

[37] T. L. Vandoorn, B. Meersman, J. D. M. De Kooning, and L. Vandevelde, "Analogy between conventional grid control and islanded microgrid control based on a global dc-link voltage droop," *IEEE Trans. Power Deliv.*, vol. 27, no. 3, pp. 1405–1414, Jul. 2012.

[38] A. Ahmed, L. Ran, S. Moon, and J.-H. Park, "A Fast PV power tracking control algorithm with reduced power mode," *IEEE Trans. Energy Convers.*, vol. 28, no. 3, pp. 565–575, Sep. 2013.

[39] L. de Brito, Moacyr, L. P. Sampaio, and C. A. e Melo, Guilhermeand Canesin, "Evaluation of the main MPPT techniques for photovoltaic applications," *IEEE Trans. Ind. Electron.*, vol. 60, no. 3, pp. 1156–1167, Mar. 2013.

[40] T. Esram and P. Chapman, "Comparison of photovoltaic array maximum power point tracking techniques," *IEEE Trans. Energy Convers.*, vol. 22, no. 2, pp. 439–449, Jun. 2007.

[41] V. Salas, E. Olías, A. Barrado, and A. Lázaro, "Review of the maximum power point tracking algorithms for stand-alone photovoltaic systems," *Sol. Energy Mater. Sol. Cells*, vol. 90, no. 11, pp. 1555–1578, Jul. 2006.

[42] A. A. Luque and S. Hegedus, *Handbook of photovoltaic science and engineering.* Wiley, 2011.

[43] M. A. S. Masoum, H. Dehbonei, and E. F. Fuchs, "Theoretical and experimental analyses of photovoltaic systems with voltageand current-based maximum power-point tracking," *IEEE Trans. Energy Convers.*, vol. 17, no. 4, pp. 514–522, Dec. 2002.

[44] S. L. Brunton, C. W. Rowley, S. R. Kulkarni, and C. Clarkson, "Maximum power point tracking for photovoltaic optimization using ripple-based extremum seeking control," *IEEE Trans. Power Electron.*, vol. 25, no. 10, pp. 2531–2540, Oct. 2010.

[45] B. Subudhi and R. Pradhan, "A comparative study on maximum power point tracking techniques for photovoltaic power systems," *IEEE Trans. Sustain. Energy*, vol. 4, no. 1, pp. 89–98, Jan. 2013.

[46] M. García, J. M. Maruri, L. Marroyo, E. Lorenzo, and M. Pérez, "Partial shadowing, MPPT performance and inverter configurations: observations at tracking PV plants," *Prog. Photovoltaics Res. Appl.*, vol. 16, no. 6, pp. 529–536, Sep. 2008.

[47] G. Spagnuolo, E. Franco, J. D. Bastidas-Rodriguez, C. A. Ramos-Paja, and G. Petrone, "Maximum power point tracking architectures for photovoltaic systems in mismatching conditions: a review," *IET Power Electron.*, vol. 7, no. 6, pp. 1396–1413, Jun. 2014.

[48] S. Kazmi, H. Goto, O. Ichinokura, and H. Guo, "An improved and very efficient mppt controller for pv systems subjected to rapidly varying atmospheric conditions and partial shading," in *Power Eng. Conf. 2009. AUPEC 2009. Australas. Univ.*, 2009, pp. 1–6.

[49] R. Alonso, P. Ibáñez, V. Martínez, E. Román, and A. Sanz, "An innovative perturb , observe and check algorithm for partially shaded pv systems," in *13th Eur. Conf. Power Electron. Appl. 2009. EPE '09.*, 2009, pp. 1–8.

[50] G. Petrone, G. Spagnuolo, R. Teodorescu, M. Veerachary, and M. Vitelli, "Reliability issues in photovoltaic power processing systems," *IEEE Trans. Ind. Electron.*, vol. 55, no. 7, pp. 2569–2580, Jul. 2008.

[51] G. Chicco, J. Schlabbach, and F. Spertino, "Experimental assessment of the waveform distortion in grid-connected photovoltaic installations," *Sol. Energy*, vol. 83, no. 7, pp. 1026–1039, Jul. 2009.

[52] P. Pakonen, A. Hildén, T. Suntio, and P. Verho, "Grid-connected PV power plant induced power quality problems - experimental evidence," in *2016 18th Eur. Conf. Power Electron. Appl. (EPE'16 ECCE Eur.)*. IEEE, Sep. 2016, pp. 1–10.

[53] A. Sangwongwanich, Y. Yang, D. Sera, and F. Blaabjerg, "Interharmonics from grid-connected PV systems: mechanism and mitigation," in *2017 IEEE 3rd Int. Futur. Energy Electron. Conf. ECCE Asia (IFEEC 2017 - ECCE Asia)*. IEEE, Jun. 2017, pp. 722–727.

[54] R. Langella, A. Testa, J. Meyer, F. Moller, R. Stiegler, and S. Z. Djokic, "Experimental-based evaluation of PV inverter harmonic and interharmonic

distortion due to different operating conditions," *IEEE Trans. Instrum. Meas.*, vol. 65, no. 10, pp. 2221–2233, Oct. 2016.

[55] E. Koutroulis and K. Kalaitzakis, "Design of a maximum power tracking system for wind-energy-conversion applications," *IEEE Trans. Ind. Electron.*, vol. 53, no. 2, pp. 486–494, Apr. 2006.

[56] S. B. Kjær, "Evaluation of the "hill climbing" and the "incremental conductance" maximum power point trackers for photovoltaic power systems," *IEEE Trans. Energy Convers.*, vol. 27, no. 4, pp. 922–929, Dec. 2012.

[57] N. Femia, G. Petrone, G. Spagnuolo, and M. Vitelli, "Optimization of perturb and observe maximum power point tracking method," *IEEE Trans. Power Electron.*, vol. 20, no. 4, pp. 963–973, Jul. 2005.

[58] J. Kivimäki and T. Suntio, "Appearance of a drift problem in variable-step perturbative MPPT algorithms," in *Eur. Photovolt. Sol. Energy Conf. Exhib. (EU PVSEC)*, 2015, pp. 1602 – 1608.

[59] J. Kivimäki, T. Suntio, and A. Kuperman, "Factors affecting validity of PVG-power settling time estimation in designing MPP-tracking perturbation frequency," in *IECON 2017 - 43rd Annu. Conf. IEEE Ind. Electron. Soc.* IEEE, Oct. 2017, pp. 2485–2491.

[60] J. Kivimaki, S. Kolesnik, M. Sitbon, T. Suntio, and A. Kuperman, "Design guidelines for multiloop perturbative maximum power point tracking algorithms," *IEEE Trans. Power Electron.*, vol. 33, no. 2, pp. 1284–1293, Feb. 2018.

[61] J. Kivimäki, S. Kolesnik, M. Sitbon, T. Suntio, and A. Kuperman, "Revisited perturbation frequency design guideline for direct fixed-step maximum power point tracking algorithms," *IEEE Trans. Ind. Electron.*, vol. 64, no. 6, pp. 4601–4609, Jun. 2017.

[62] F. Liu, S. Duan, F. Liu, B. Liu, and Y. Kang, "A variable step size inc mppt method for pv systems," *IEEE Trans. Ind. Electron.*, vol. 55, no. 7, pp. 2622–2628, Jul. 2008.

[63] R. P. Venturini, V. Scarpa, G. Spiazzi, and S. Buso, "Analysis of limit cycle oscillations in maximum power point tracking algorithms," in *2008 IEEE Power Electron. Spec. Conf.* IEEE, Jun. 2008, pp. 378–384.

[64] H. Schmidt, B. Burger, U. Bussemas, and S. Elies, "How fast does an mpp tracker really need to be?" in *24th Eur. Photovolt. Sol. Energy Conf.*, 2009, pp. 3273–3276.

[65] M. A. Elgendy, B. Zahawi, and D. J. Atkinson, "Operating characteristics of the P&O algorithm at high perturbation frequencies for standalone PV systems," *IEEE Trans. Energy Convers.*, vol. 30, no. 1, pp. 189–198, Mar. 2015.

[66] J. Viinamäki, A. Kuperman, J. Jokipii, T. Messo, T. Suntio, and M. Sitbon, "Comprehensive dynamic analysis of photovoltaic generator interfacing DC-DC boost power stage," *IET Renew. Power Gener.*, vol. 9, no. 4, pp. 306–314, May 2015.

[67] J. Kivimäki, "Design Issues in Implementing Maximum-Power-Point Tracking Algorithms for PV Applications," Master's thesis, Tampere University of Technology, 2015.

[68] J. Basilio and S. Matos, "Design of PI and PID controllers with transient performance specification," *IEEE Trans. Educ.*, vol. 45, no. 4, pp. 364–370, Nov. 2002.

[69] T. Suntio, T. Messo, and J. Puukko, *Power electronic converters dynamics and control in conventional and renewable energy applictions.* John Wiley & Sons, Incorporated, 2017.

[70] W. Xiao, N. Ozog, and W. G. Dunford, "Topology study of photovoltaic interface for maximum power point tracking," *IEEE Trans. Ind. Electron.*, vol. 54, no. 3, pp. 1696–1704, Jun. 2007.

[71] R. Dougal, "Dynamic multiphysics model for solar array," *IEEE Trans. Energy Convers.*, vol. 17, no. 2, pp. 285–294, Jun. 2002.

[72] L. Nousiainen, J. Puukko, A. Mäki, T. Messo, J. Huusari, J. Jokipii, J. Viinamäki, D. T. Lobera, S. Valkealahti, and T. Suntio, "Photovoltaic generator as an input source for power electronic converters," *IEEE Trans. Power Electron.*, vol. 28, no. 6, pp. 3028–3038, Jun. 2013.

[73] T. Suntio, J. Leppäaho, J. Huusari, and L. Nousiainen, "Issues on solar-generator interfacing with current-fed MPP-tracking converters," *IEEE Trans. Power Electron.*, vol. 25, no. 9, pp. 2409–2419, Sep. 2010.

[74] T. Esram, J. Kimball, P. Krein, P. Chapman, and P. Midya, "Dynamic maximum power point tracking of photovoltaic arrays using ripple correlation control," *IEEE Trans. Power Electron.*, vol. 21, no. 5, pp. 1282–1291, Sep. 2006.

[75] R. Middlebrook and S. Cuk, "A general unified approach to modelling switching-converter power stages," in *1970 IEEE Power Electron. Spec. Conf.* IEEE, Jun. 1976, pp. 18–34.

[76] C. K. Tse, *Linear circuit analysis.* Addison-Wesley, 1998.

[77] J. Viinamäki, A. Kuperman, and T. Suntio, "Grid-forming-mode operation of boost-power-stage converter in PV-generator-interfacing applications," *Energies*, vol. 10, no. 7, Jul. 2017.

[78] K. Ogata, *Modern control engineering.* Paerson, 2012.

[79] F. Reukers, *Pade-approximations in number theory.* Springer, 1981.

[80] J. Kivimäki, M. Sitbon, S. Kolesnik, A. Kuperman, and T. Suntio, "Determining maximum MPP-tracking sampling frequency for input-voltage-controlled PV-interfacing converter," in *2016 IEEE Energy Convers. Congr. Expo.* IEEE, Sep. 2016, pp. 1–8.

[81] J. Sun, "Impedance-based stability criterion for grid-connected inverters," *IEEE Trans. Power Electron.*, vol. 26, no. 11, pp. 3075–3078, Nov. 2011.

[82] J. Huusari and T. Suntio, "Interfacing constraints of distributed maximum power point tracking converters in photovoltaic applications," in *2012 15th Int. Power Electron. Motion Control Conf.* IEEE, Sep. 2012, pp. DS3d.1–1–DS3d.1–7.

[83] D. P. Hohm and M. E. Ropp, "Comparative study of maximum power point tracking algorithms," *Prog. Photovoltaics Res. Appl.*, vol. 11, no. 1, pp. 47–62, Jan. 2003.

[84] D. Shmilovitz, "On the control of photovoltaic maximum power point tracker via output parameters," *IEE Proc. - Electr. Power Appl.*, vol. 152, no. 2, p. 239, 2005.

[85] M. Sitbon, J. Leppäaho, T. Suntio, and A. Kuperman, "Dynamics of photovoltaic-generator-interfacing voltage-controlled buck power stage," *IEEE J. Photovoltaics*, vol. 5, no. 2, pp. 633–640, Mar. 2015.

[86] A. K. Abdelsalam, A. M. Massoud, S. Ahmed, and P. N. Enjeti, "High-performance adaptive perturb and observe mppt technique for photovoltaic-based microgrids," *IEEE Trans. Power Electron.*, vol. 26, no. 4, pp. 1010–1021, Apr. 2011.

[87] Y. Jiang, J. A. Abu Qahouq, and T. A. Haskew, "Adaptive step size with adaptive-perturbation-frequency digital MPPT Controller for a single-sensor photovoltaic solar system," *IEEE Trans. Power Electron.*, vol. 28, no. 7, pp. 3195–3205, Jul. 2013.

[88] A. Pandey, N. Dasgupta, and A. K. Mukerjee, "Design issues in implementing mppt for improved tracking and dynamic performance," in *IECON 2006 - 32nd Annu. Conf. IEEE Ind. Electron.* IEEE, Nov. 2006, pp. 4387–4391.

[89] M. A. Elgendy, D. J. Atkinson, and B. Zahawi, "Experimental investigation of the incremental conductance maximum power point tracking algorithm at high perturbation rates," *IET Renew. Power Gener.*, vol. 10, no. 2, pp. 133–139, Feb. 2016.

[90] G. Graditi, G. Adinolfi, N. Femia, and M. Vitelli, "Comparative analysis of synchronous rectification boost and diode rectification boost converter for DMPPT applications," in *2011 IEEE Int. Symp. Ind. Electron.* IEEE, Jun. 2011, pp. 1000–1005.

[91] M. Sitbon, S. Schacham, T. Suntio, and A. Kuperman, "Improved adaptive input voltage control of a solar array interfacing current mode controlled boost power stage," *Energy Convers. Manag.*, vol. 98, pp. 369–375, Jul. 2015.

[92] A. Urtasun, P. Sanchis, and L. Marroyo, "Adaptive voltage control of the dc/dc boost stage in PV converters with small input capacitor," *IEEE Trans. Power Electron.*, vol. 28, no. 11, pp. 5038–5048, Nov. 2013.

[93] N. Femia, D. Granozio, G. Petrone, G. Spagnuolo, and M. Vitelli, "Predictive & adaptive MPPT perturb and observe method," *IEEE Trans. Aerosp. Electron. Syst.*, vol. 43, no. 3, pp. 934–950, Jul. 2007.

[94] D. Sera, R. Teodorescu, J. Hantschel, and M. Knoll, "Optimized maximum power point tracker for fast-changing environmental conditions," *IEEE Trans. Ind. Electron.*, vol. 55, no. 7, pp. 2629–2637, Jul. 2008.

[95] D. G. Montoya, C. A. R. Paja, and G. Petrone, "Design method of the perturb and observe controller parameters for photovoltaic applications," in *2012 IEEE 4th Colomb. Work. Circuits Syst.* IEEE, Nov. 2012, pp. 1–6.

[96] C. R. Sullivan, J. J. Awerbuch, and A. M. Latham, "Decrease in photovoltaic power output from ripple: simple general calculation and the effect of partial shading," *IEEE Trans. Power Electron.*, vol. 28, no. 2, pp. 740–747, Feb. 2013.

[97] K. Lappalainen and S. Valkealahti, "Effects of irradiance transition characteristics on the mismatch losses of different electrical PV array configurations," *IET Renew. Power Gener.*, vol. 11, no. 2, pp. 248–254, Feb. 2017.

[98] S. Valkealahti and K. Lappalainen, "Recognition of irradiance transitions caused by moving clouds harmful to the operation of pv systems," *29th Eur. Photovolt. Sol. Energy Conf. Exhib.*, pp. 2650–2653, Nov. 2014.

[99] H. Al-Atrash, I. Batarseh, and K. Rustom, "Effect of measurement noise and bias on hill-climbing mppt algorithms," *IEEE Trans. Aerosp. Electron. Syst.*, vol. 46, no. 2, pp. 745–760, Apr. 2010.

[100] N. Rebei, R. Gammoudi, A. Hmidet, and O. Hasnaoui, "Experimental implementation techniques of P&O MPPT algorithm for PV pumping system," in *2014 IEEE 11th Int. Multi-Conference Syst. Signals Devices.* IEEE, Feb. 2014, pp. 1–6.

[101] Y. Sun, Y. Liu, M. Su, W. Xiong, and J. Yang, "Review of active power decoupling topologies in single-phase systems," *IEEE Trans. Power Electron.*, vol. 31, no. 7, pp. 4778–4794, 2015.

[102] H. Hu, S. Harb, N. Kutkut, I. Batarseh, and Z. J. Shen, "A review of power decoupling techniques for microinverters with three different decoupling capacitor locations in PV systems," *IEEE Trans. Power Electron.*, vol. 28, no. 6, pp. 2711–2726, Jun. 2013.

[103] J. Kwon, B. Kwon, and K. Nam, "Grid-connected photovoltaic multistring PCS with PV current variation reduction control," *IEEE Trans. Ind. Electron.*, vol. 56, no. 11, pp. 4381–4388, Nov. 2009.

[104] J. Viinamäki, J. Jokipii, and T. Suntio, "Improving double-line-frequency voltage ripple rejection capability of dc/dc converter in grid connected two-stage PV inverter using dc-link voltage feedforward," in *2016 18th Eur. Conf. Power Electron. Appl. (EPE'16 ECCE Eur.).* IEEE, Sep. 2016, pp. 1–10.

[105] J. Viinamäki, J. Kivimäki, T. Suntio, and L. Hietalahti, "Design of boost-power-stage converter for PV generator interfacing," in *2014 16th Eur. Conf. Power Electron. Appl.* IEEE, Aug. 2014, pp. 1–10.

[106] B. Gu, J. Dominic, J. Zhang, L. Zhang, B. Chen, and J. Lai, "Control of electrolyte-free microinverter with improved MPPT performance and grid current quality," in *2014 IEEE Appl. Power Electron. Conf. Expo. - APEC 2014.* IEEE, Mar. 2014, pp. 1788–1792.

[107] M. Purhonen, J. Hannonen, J.-P. Ström, and P. Silventoinen, "Step-up dc-dc converter passive component dimensioning in photovoltaic applications," in *2012 IEEE 27th Conv. Electr. Electron. Eng. Isr.* IEEE, Nov. 2012, pp. 1–5.

A TABLES

Table A.1: Parameters of the voltage-boosting dc-dc converter utilized in the thesis.

Parameter	Value
L	300 μH
C_1	90 μF
C_2	20 μF
r_{C1}	200 mΩ
r_{C2}	4 mΩ
r_D	45 mΩ
V_D	0.39 V
r_{sw}	6.2 mΩ

Table A.2: Parameters of the Raloss SR30-36 module utilized in the thesis.

Parameter	Value
V_{oc}	19.2 V
I_{sc}	1.0 A
P_{mpp}	15 W
V_{mpp}	16 V
I_{mpp}	0.91 A
N_s	36
G	500 W/m^2
T_K	45°

B   LABORATORY SETUP
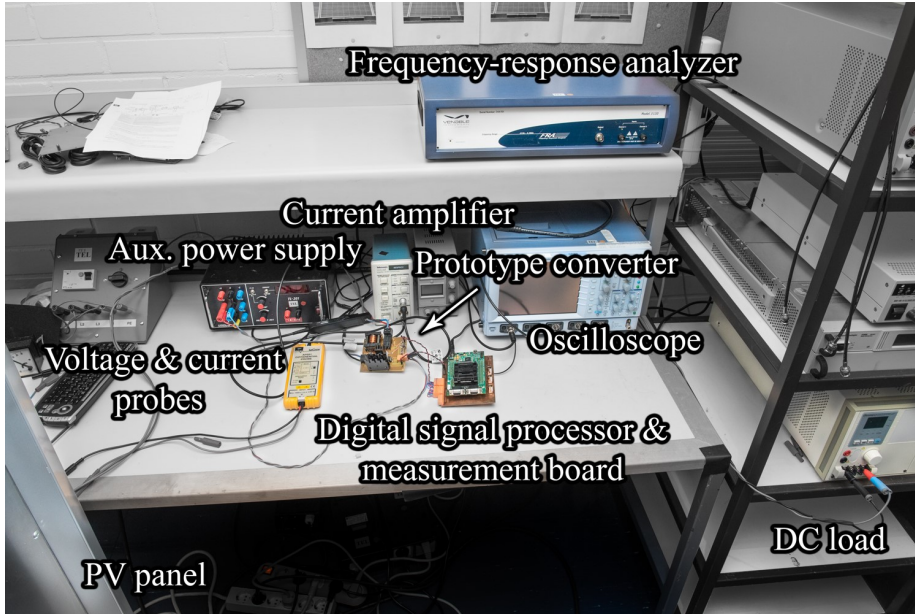
Fig. B.1: Laboratory setup for measuring the PV-interfacing dc-dc converter.